UNIVERSIDAD DE CHILE
FACULTAD DE CIENCIAS FÍSICAS Y MATEMÁTICAS
DEPARTAMENTO DE INGENIERÍA CIVIL

EFFICIENT SHEAR-FLEXURE INTERACTION MODEL FOR NONLINEAR ANALYSIS OF REINFORCED CONCRETE STRUCTURAL WALLS

TESIS PARA OPTAR AL GRADO DE MAGÍSTER EN CIENCIAS DE LA INGENIERÍA, MENCIÓN INGENIERÍA ESTRUCTURAL, SÍSMICA Y GEOTÉCNICA

MEMORIA PARA OPTAR AL TÍTULO DE INGENIERO CIVIL

CARLOS NICOLÁS LÓPEZ OLEA

PROFESOR GUÍA:
LEONARDO MAXIMILIANO MASSONE SANCHEZ

MIEMBROS DE LA COMISIÓN:
KRISTIJAN KOLOZVARI
FABIÁN ROJAS BARRALES

SANTIAGO DE CHILE
2021

RESUMEN DE LA TESIS PARA OPTAR AL
GRADO DE MAGÍSTER EN CIENCIAS DE
LA INGENIERÍA, MENCIÓN INGENIERÍA
ESTRUCTURAL, SÍSMICA Y GEOTÉCNICA;
Y AL TÍTULO DE INGENIERO CIVIL
POR: CARLOS NICOLÁS LÓPEZ OLEA
FECHA: ENERO 2021
PROF. GUÍA: LEONARDO MASSONE S.

EFFICIENT SHEAR-FLEXURE INTERACTION MODEL FOR NONLINEAR ANALYSIS OF REINFORCED CONCRETE STRUCTURAL WALLS

A research was conducted to develop a macroscopic modeling approach that integrates axial, flexure, and shear interaction under cyclic loading conditions to obtain reliable predictions of the nonlinear response of reinforced concrete (RC) structural walls. The model, named as Efficient-Shear-Flexure-Interaction (E-SFI), is intended to provide accurate results for squat, medium-rise, and slender walls, with a computationally efficient formulation that can be used under generalized conditions. The E-SFI model, based on the Shear-Flexure Interaction Multiple-Vertical-Line-Element-Model (SFI-MVLEM), incorporates a two-dimensional RC panel behavior described with a fixed-crack-angle approach. The novel formulation removes the internal degree of freedom per RC panel element of the SFI-MVLEM model by incorporating a calibrated expression to compute the horizontal normal strain (ε_x), obtaining only six degrees of freedom per element, similar to common fiber-based models. To validate the model, an extensive shear strength database of 252 RC wall specimen tests reported in the literature was used, obtaining an average ratio of the predicted over the experimentally measured shear strength (V_{model}/V_{test}) of 1.04 with a coefficient of variation of 0.24, indicating an accurate estimation of the shear strength, as well as revealing a relatively small dependence to wall parameters. Also, the predicted and experimentally measured hysteretic response was compared for ten densely-instrumented RC wall specimens reported in the literature, for a shear span-to-depth ratio ranging from 0.44 to 3.0, under single or double curvature conditions, obtaining an accurate prediction of the global, flexural, and shear displacement responses. Finally, a benchmarking was developed to study the efficiency of the E-SFI model, revealing that the novel model formulation allows an important improvement in terms of runtime and convergence rate compared with the SFI-MVLEM.

RESUMEN DE LA TESIS PARA OPTAR AL
GRADO DE MAGÍSTER EN CIENCIAS DE
LA INGENIERÍA, MENCIÓN INGENIERÍA
ESTRUCTURAL, SÍSMICA Y GEOTÉCNICA;
Y AL TÍTULO DE INGENIERO CIVIL
POR: CARLOS NICOLÁS LÓPEZ OLEA
FECHA: ENERO 2021
PROF. GUÍA: LEONARDO MASSONE S.

MODELO DE INTERACCIÓN FLEXIÓN-CORTE EFICIENTE PARA EL ANÁLISIS NO LINEAL DE MUROS ESTRUCTURALES DE HORMIGÓN ARMADO

Se llevó a cabo una investigación para desarrollar un modelo macroscópico que integra la interacción axial, flexión y corte bajo condiciones de carga cíclica para obtener predicciones precisas de la respuesta no lineal de muros estructurales de hormigón armado (HA). El modelo, denominado Efficient-Shear-Flexure-Interaction (E-SFI), busca proveer de resultados precisos para muros de baja, mediana, y alta esbeltez, con una formulación computacionalmente eficiente que pueda ser usada en condiciones generalizadas. El modelo E-SFI, basado en el Shear-Flexure Interaction Multiple-Vertical-Line-Element-Model (SFI-MVLEM), incorpora un panel de HA bi-dimensional descrito por un enfoque de modelo de ángulo fijo. La nueva formulación remueve el grado de libertad interno por cada elemento panel de HA del modelo SFI-MVLEM mediante la incorporación de una expresión calibrada para calcular la deformación normal horizontal (ε_x), obteniendo solo seis grados de libertad por elemento, similar a los modelos comunes basados en fibras. Para validar el modelo, una extensa base de datos de 252 probetas de muro de HA reportadas en la literatura fue utilizada, obteniendo un promedio de la razón entre la capacidad al corte predicha y medida experimentalmente (V_{model}/V_{test}) de 1.04 con un coeficiente de variación de 0.24, indicando una predicción precisa de la capacidad al corte, como también revelando una relativamente baja dependencia del modelo a los parámetros del muro. Además, se comparó la respuesta histerética predicha y medida experimentalmente para diez probetas de muro de HA instrumentadas reportadas en la literatura, para un rango de relación de esbeltez entre 0.44 a 3.0, bajo condiciones de curvatura simple o doble, obteniendo una predicción precisa de la respuestas de desplazamiento global, flexural y de corte. Finalmente, se realizó una evaluación comparativa de la eficiencia del modelo E-SFI, revelando que la nueva formulación permite una mejora importante en términos de tiempo de ejecución y tasa de convergencia comparado con el modelo SFI-MVLEM.

To my family.

Acknowledgments

I would like to express my deepest appreciation and sincere gratitude to my research advisor, Professor Leonardo Massone. His expertise, guidance, support, patient, and discussions, have been a great support to develop my master thesis at University of Chile. I am very thankful to him for being always available, for spending a lot of time in conversations and discussions that will remain as great memories. I would also like to thank Professor Kristijan Kolozvari. His initial guidance through the model code was fundamental to develop my research. I am very grateful to him for spending time to reply to my e-mails and for his collaboration during the research.

I would like to acknowledge all my friends and professors that I have been the opportunity to meet at University of Chile. I take the best memory of each one of you. I wish you the best for the future. Last but not least, I would like to thank my parents Juan Carlos and Fabiola, and my brothers Paulina and Octavio. Thanks for your unconditional support, for being in the good and bad times. Nothing would be the same without you. I love you.

This work was funded by the National Agency for Research and Development (ANID) for the project Fondecyt Regular 2020 N°1200023.

Table of Contents

List of Tables

List of Figures

Chapter 1

Introduction

1.1. General

Properly detailed reinforced concrete (RC) walls are commonly used as part of the structural system to limit lateral deformations and resist the lateral loads imposed by earthquake ground motions and wind. Current design requirements of the ACI 318 code (ACI Committee 318, 2019) promote flexural yielding of vertical reinforcement of walls; therefore, ductile flexural behavior is desirable over brittle shear failure. The global response of RC walls is made up of flexural and shear deformation responses, and is usually classified according to the wall aspect ratio (h_w/l_w) or shear-span-to-depth ratio (M/Vl_w), as shear-controlled walls ($M/Vl_w < 1.5$), flexural-controlled walls ($M/Vl_w > 2.5$), and medium-rise walls ($1.5 \leq M/Vl_w \leq 2.5$). Although it is a common practice to uncouple the axial-flexural and shear behaviors, experimental test results of RC walls have shown that inelastic axial-flexural and shear behaviors occur near-simultaneously (Oesterle et al., 1976), even for slender walls dominated by flexural yielding (Massone et al., 2004), commonly referred to as shear-flexure interaction (SFI).

Analytical modeling of the nonlinear response of structural RC walls can be accomplished using microscopic (finite element) or macroscopic (behavioral) models. For models based on the finite element method (FEM), shear-flexure interaction can be captured (Kolozvari et al., 2019); however, due to high computational cost, and complexity in their implementation and analysis of results, these type of models are currently less used than behavioral models. Most of macroscopic models available nowadays do not account for shear-flexure interaction (flexural models) as the Multiple-Vertical-Line-Element-Model (MVLEM; Orakcal et al., 2004), which is adequate for relative slender walls; nevertheless, they lead to an overestimation of the capacity and ductility of medium-rise and squat walls (Massone et al., 2006). Few macroscopic models that include shear-flexure interaction exist nowadays (Kolozvari et al., 2019) with various assumptions that increase the range of applicability compared to flexural models; however, computational cost make these models actually less used in engineering practice than uncoupled models.

1.2. Scope

Although several analytical models are currently available to predict the nonlinear behavior of RC walls, a simple yet effective macro-model that incorporates the axial-shear-flexure interaction with accurate predictions of the global, flexural, and shear deformation responses, from squat to slender walls, is a need. Even more, when performance-based methodologies require for design a reliable prediction of the nonlinear response of structural members under generalized loading conditions. The proposed model, based on the SFI-MVLEM model (Kolozvari et al., 2015), incorporates a calibrated expression for computing the horizontal normal strain (ε_x) in terms of local variables of the panel, such as the shear strain (γ_{xy}) and the horizontal reinforcement ratio (ρ_h); therefore, the additional degree of freedom per RC panel element is removed from the SFI-MVLEM formulation.

In summary, the primary objectives of this study are to:

1. develop a calibrated expression for the horizontal normal strain (ε_x) in terms of the panel local variables without distinction between different boundary conditions and global wall parameters, by using a database provided by a 2D-FEM RC wall analysis;

2. develop a macroscopic modeling approach for RC structural walls under reversed cyclic loading conditions that includes the shear-flexure interaction with the proposed calibrated expression for computing the horizontal normal strain;

3. investigate the model sensitivity to different modeling parameters to assess its robustness and accuracy, providing recommendations for its use;

4. assess the model capabilities to predict the shear strength of RC structural walls and its dependence on wall parameters, by comparing the model prediction with the experimentally measured shear strength for a database of 252 RC wall tests reported in the literature;

5. assess the model capabilities to predict the nonlinear hysteretic behavior of RC walls from squat to slender walls and different failure mechanisms, by comparing the predicted and experimentally measured hysteretic behaviors of ten heavily instrumented wall specimens reported in the literature;

6. assess the model efficiency compared to the MVLEM and SFI-MVLEM models in terms of runtime and convergence rate;

7. request the incorporation of the wall model to OpenSees for public use and future development.

1.3. Organization

This dissertation is divided into five chapters. Chapter two provides a review of the shear-flexure interaction phenomenon, the modeling approaches of structural systems, and a general description of the principal macroscopic and microscopic models developed up to date. Chapter three describes the proposed analytical model, the adopted reinforced concrete panel model, and the constitutive models used for concrete and reinforcing steel. Chapter four present a sensitivity analysis of the analytical model to shear resisting parameters and mesh size, a comparison between the analytically predicted and experimentally measured shear strength for a database of tests reported in the literature, a validation of the predicted hysteretic response of ten densely-instrumented reinforced concrete wall specimens reported in the literature, and a benchmarking to assess the model efficiency. A summary and conclusions are presented in chapter five.

Chapter 2

Literature Review

At the beginning of this chapter, a review of the experimentally observed shear and axial-flexural interaction is presented, followed by an overview of the main macroscopic modeling approaches of RC structural walls with uncoupled and coupled shear and axial-flexural behaviors, as well as the main microscopic modeling approaches of RC structural walls reported in the literature.

2.1. Experimental evidence of shear-flexure interaction

The coupled shear and axial-flexural behavior of RC walls was first observed by Oesterle et al. (1976, 1979), indicating that shear yielding occurred in each specimen near-simultaneously with flexural yielding. Further studies to assess deformation associated with flexure and shear of RC wall specimen tests RW2 (Thomsen & Wallace, 2004) and SRCW1 (Sayre, 2003) was developed by Massone & Wallace (2004). The applied lateral load versus flexural and shear displacement responses of specimen RW2 is presented in Figure 2.1, indicating that inelastic flexural and shear behaviors occur at a lateral load close to that associated with the load to reach the wall nominal moment, despite a nominal shear capacity of approximately twice the applied load, indicating an interaction between both deformation components, even for slender walls dominated by flexure. Similar behavior was observed for specimen SRCW1.

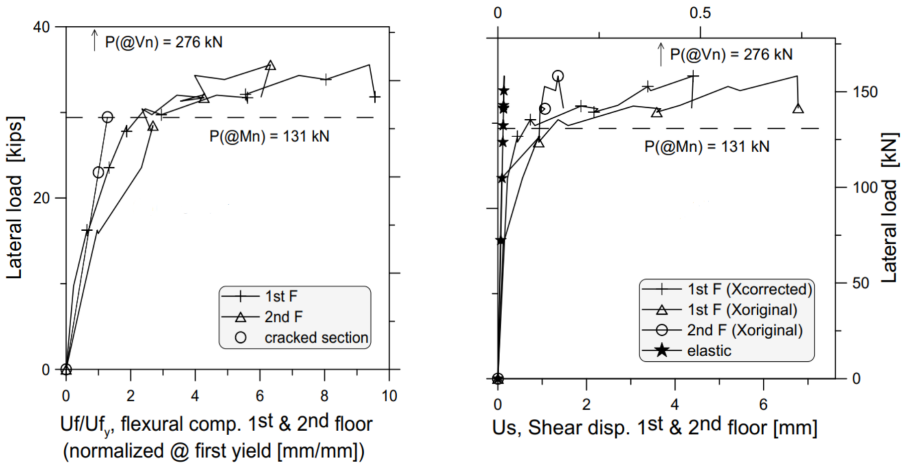

(a) Flexure (b) Shear

Figure 2.1: Story deformations of specimen RW2 (Massone, 2006).

Additional evidence of the shear-flexure interaction phenomenon in RC wall specimens can be found in more recent researches as developed by Massone et al. (2006), Tran & Wallace (2012), and Terzioglu et al. (2018), among others.

2.2. Modeling approaches of structural systems

Modeling approaches for nonlinear analysis of structural systems can be classified according to the level of complexity of their formulation, which is directly related to the computational effort, from simple models such as those of concentrated plasticity to more complex models such as those based on the finite element method. Simple uncoupled lumped plasticity models, depicted in Figure 2.2(a), consider an equivalent linear elastic beam-column element at the element centroidal axis with rotational, shear, and axial springs located at each end of the element. The nonlinear behavior is described by an implemented moment-rotation and force-deformation relationships for rotational and shear/axial springs, respectively. In distributed plasticity fiber-based models, illustrated in Figure 2.2(b), material nonlinearity can occur at any selected section (quadrature points), which are integrated to obtain the element response. The cross-section of a fiber-based model is simulated by a series of longitudinal uniaxial fibers, the Bernoulli-Euler hypothesis is generally implemented at the element level, and constitutive stress-strain relationships for materials are used, which enables coupling of axial-flexure behavior. Fiber-based models are less computationally efficient than lumped plasticity models; however, model resisting force is more accurate when the plastic hinge region occurs into the element interior. Finally, the most sophisticated models are those based on the finite element method, depicted in Figure 2.2(c), which consider a generalized stress-strain relationship of materials with no kinematic assumptions, allowing them to be used under more generalized conditions than the model types mentioned above. The selection of a proper model type for a given application is based on a balance between reliability and computational efficiency, where the reliability of the model is given by an accurate prediction of the critical types of deformation.

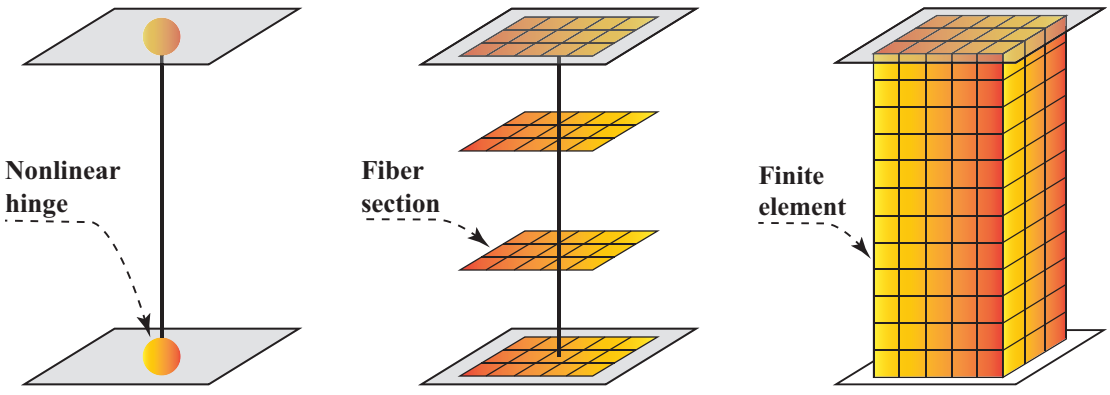

(a) Lumped plasticity (b) Distributed plasticity (c) Finite element

Figure 2.2: Modeling type of structural elements.

2.3. Macroscopic models for RC structural walls

Macroscopic modeling approaches for RC structural walls can be divided into two mains groups, models with uncoupled and coupled shear and axial-flexural behaviors. Uncoupled models are generally accurate at both global and local response levels for relative slender walls; however, they overestimate the lateral load capacity and ductility of medium-rise and squat walls (Massone et al., 2006). On the other hand, coupled models can accurately predict global and local responses from slender to squat walls, increasing the range of applicability compared to flexural models, although its assumptions can limit the accuracy and range of applicability.

2.3.1. Uncoupled models

2.3.1.1. Lumped plasticity models

As illustrated in Figure 2.3, lumped plasticity models consider an equivalent linear elastic beam-column element at the wall centroidal axis with rotational, axial, and shear springs located at each end of the element. The nonlinear behavior is described by an implemented moment-rotation and force-deformation relationship for rotational and axial/shear springs, respectively. Although these models are computationally efficient, they do not capture the neutral axis along the wall cross-section and may not correctly consider the effects of rocking of the wall and interaction with the connecting girders, in-plane of the wall and perpendicular to the wall (Orakcal et al., 2004).

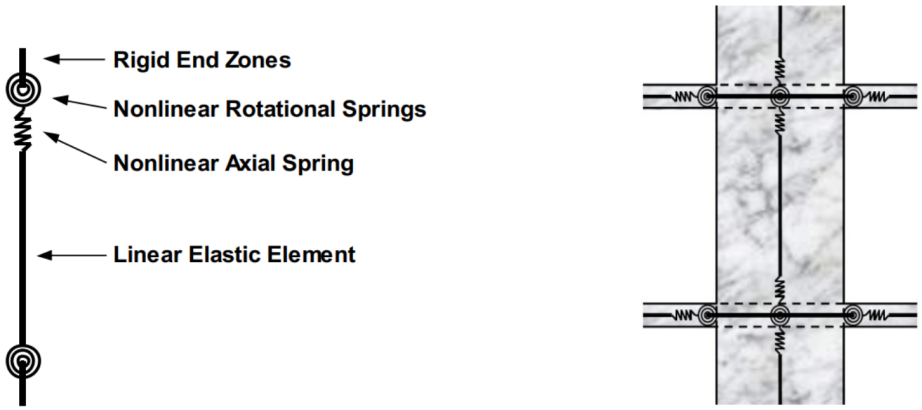

(a) Beam-column element (b) Model configuration

Figure 2.3: Beam-column element model (Orakcal et al., 2004).

2.3.1.2. Multiple vertical line element model

The multiple vertical line element model (MVLEM) is similar to distributed plasticity fiber-based models but with a single integration point. The model was proposed originally by Vulcano et al. (1988), and subsequently calibrated and validated against extensive experimental data at both local and global response levels by Orakcal & Wallace (2004), who incorporated detailed cyclic stress-strain constitutive relationships for concrete and steel. The model is available in the computational framework OpenSees (McKenna et al., 2010) as implemented by Kolozvari et al. (2018). As shown in Figure 2.4, an MVLEM element is described by six external degrees of freedom (DOFs) that represent horizontal and vertical displacements and rotations at the top and bottom element nodes $\{\delta_N\}$. Also, the kinematic assumption of plane sections remain plane (Bernoulli-Euler hypothesis) is considered to obtain the vertical strain of each one of the m uniaxial elements over the element length. A horizontal spring placed at height ch is incorporated to account for shear response; therefore, flexural and shear modes of deformation of the wall member are uncoupled.

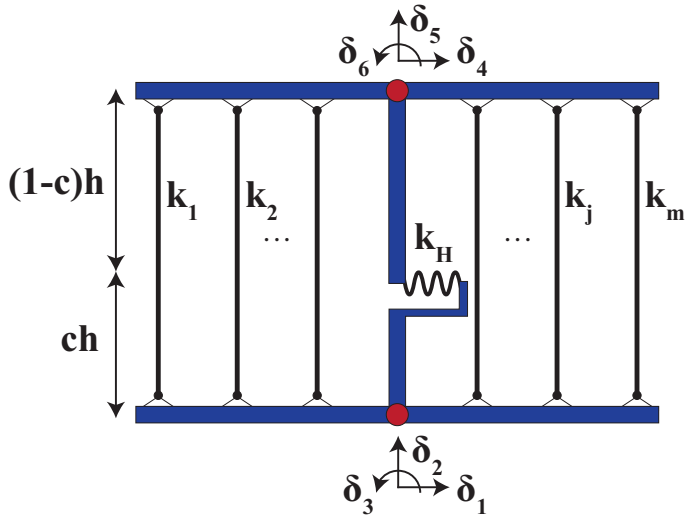

Figure 2.4: MVLEM element.

The curvature of an MVLEM element is assumed to be uniform, whereas displacement-based element curvature is linear, and the resultant rotation is concentrated at height ch. A value of $c = 0.4$ is recommended based on comparison with experimental test results (Vulcano et al., 1988). Rotations and resulting flexural displacements are calculated based on the wall curvature, as shown in Figure 2.5. A structural wall is modeled as a stack of n elements placed one upon the other, resulting in a total number of $N = 3(n + 1)$ degrees of freedom. The global stiffness matrix $[K]$ for a wall model is a square matrix of dimension $N \times N$, and the global force vector $\{F_{int}\}$ is of dimension $N \times 1$. The nonlinear problem to solve consists of reaching force equilibrium in each one of the N degrees of freedom. The MVLEM has shown to be an effective modeling approach for the flexural response prediction of slender RC walls by contrasting the experimentally measured and predicted values of the lateral load capacity and stiffness at different drift levels, yield point, cyclic properties of the load-displacement response, displacement profile, average rotations and displacements over the region of inelastic deformations (Orakcal et al., 2004).

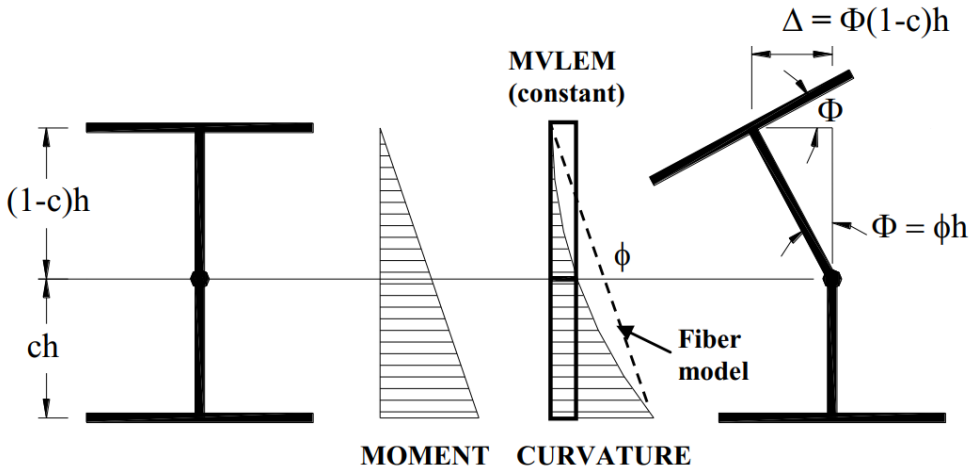

Figure 2.5: Flexural deformations of the MVLEM (Orakcal et al., 2004).

2.3.1.3. Force wall element

The force wall element (FWE) proposed by Vásquez et al. (2016) is a distributed plasticity fiber-based beam-column model with a force-based element formulation. The kinematic assumption of plane sections remain plane (Bernoulli-Euler hypothesis) is implemented at element level. As depicted in Figure 2.6(a), axial and flexural behaviors are simulated by longitudinal fibers representing concrete and vertical reinforcing steel, whose properties at each integration point are based on generalized cyclic stress-strain constitutive relationships. On the other hand, as shown in Figure 2.6(b), the shear behavior is incorporated into the model using a shear section characterized by a backbone relationship. The model was validated against the cyclic response of slender shear walls (rectangular, U-shaped, and T-shaped) under two-dimensional and three-dimensional conditions, obtaining accurate predictions of the initial stiffness, peak strength, unloading/reloading stiffness, and ductility (Vásquez et al., 2016).

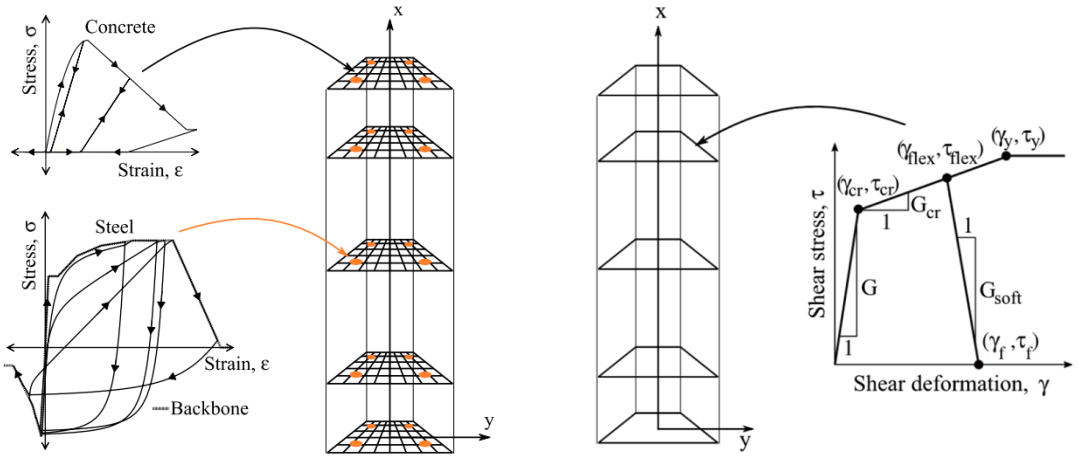

(a) Simulation of flexural behavior

(b) Simulation of shear behavior

Figure 2.6: Force wall element (Vásquez et al., 2016).

2.3.2. Coupled models

2.3.2.1. Shear-flexure interaction displacement-based fiber model

The shear-flexure interaction displacement-based fiber element model (dispBeamColumnInt) implemented in the computational platform OpenSees was developed by Massone et al. (2006) based on applying the methodology proposed by Petrangeli et al. (1999). As illustrated in Figure 2.7, the model incorporates the shear-flexure interaction phenomenon by replacing the m uniaxial elements of the MVLEM by two-dimensional RC panel elements (also called strip) subjected to membrane actions. The constitutive panel element follows the Rotating-Angle Softened-Truss-Model (RA-STM, Pang & Hsu, 1995) approach with a more refined constitutive stress-strain model for concrete in compression. The model modifies the original formulation of the MVLEM to accommodate displacement interpolation functions and integration points for practical implementation of the model into computational platforms, in which the displacement-based fiber model formulation is already built-in. The vertical normal strain (ε_y) and shear distortion (γ_{xy}) are obtained for the entire section using the six external degrees of freedom, the kinematic assumption of plane sections remain plane (Bernoulli-Euler hypothesis), and the assumption of constant shear strain, similar as the MVLEM. The value of the horizontal normal strain (ε_x) is required to complete the strain field of each panel element. In this formulation, a numerical procedure is implemented to iterate over the unknown quantity of the horizontal normal strain (ε_x) to achieve zero resultant horizontal normal stress within each strip ($\sigma_x = 0$) for trial values of the vertical normal strain (ε_y) and the shear strain (γ_{xy}). When horizontal equilibrium is achieved within each strip, global equilibrium is checked for the overall wall model by comparing the applied and resisting forces. The analytical model prediction was contrasted with experimental test results for monotonic loading conditions, revealing an accurate prediction of strength and stiffness of RC structural walls with a shear-span to depth ratio greater than approximately 0.69, which is related to the assumption of zero resultant horizontal normal stress (Massone et al., 2006).

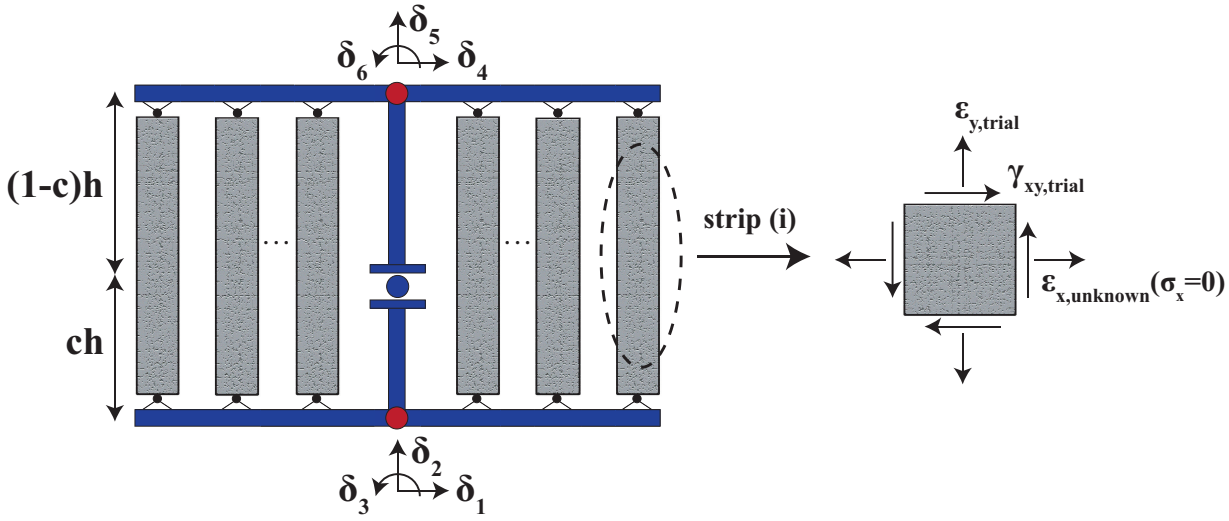

Figure 2.7: dispBeamColumnInt element.

2.3.2.2. Nonlinear beam-truss model

The three-dimensional nonlinear beam-truss model implemented in the computational platform OpenSees was proposed by Panagiotou et al. (2014) based on the strut-and-tie modeling approach. The model incorporates the shear-flexure interaction phenomenon by using diagonal truss elements to resemble principal stress directions of concrete when approaching the ultimate load. As seen in Figure 2.8, a structural wall model is composed of vertical and horizontal truss elements to represent the reinforcing bars and their surrounding concrete, and diagonal truss elements are used to represent the concrete behavior. Each truss element is connected to two nodes, and refined cyclic constitutive stress-strain relationships for concrete and steel are used. The analytical model was validated against RC wall specimen tests subjected to reversed-cyclic loading conditions, obtaining accurate predictions for post-cracking response in terms of strength and stiffness. Some shortcomings of the model are the overestimation of the initial stiffness and strength due to the overlapping of elements, the selection of the orientation for concrete struts, and a large number of degrees of freedom in a wall model.

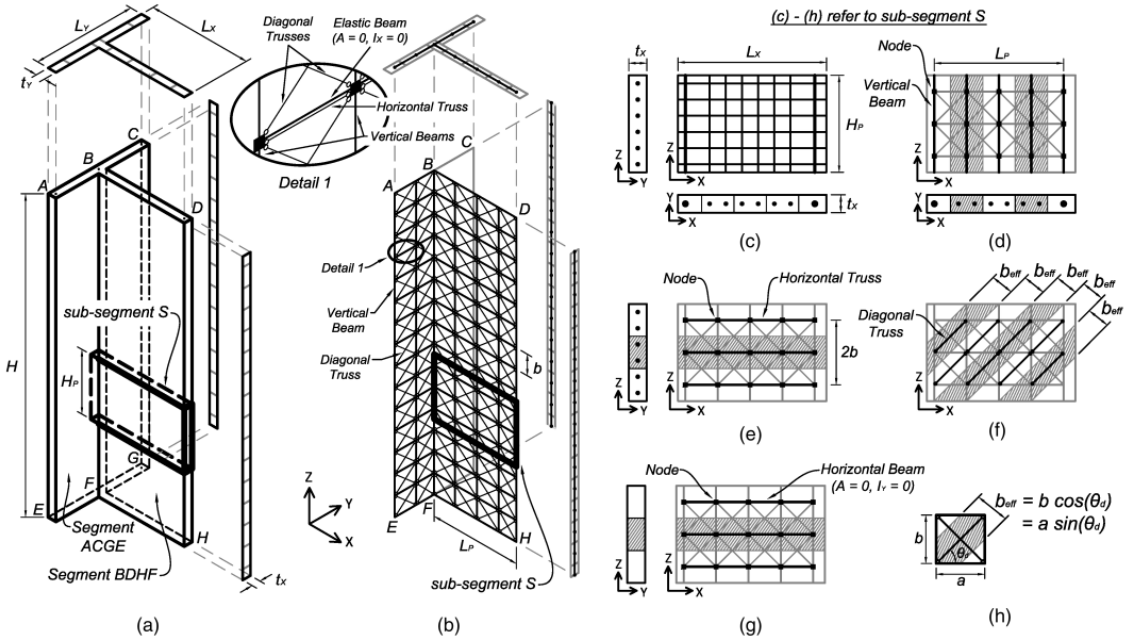

Figure 2.8: Schematic description of the beam-truss model approach for a T-shape section wall (Lu & Panagiotou, 2014).

2.3.2.3. Shear-flexure interaction multiple vertical line element model

The shear-flexure interaction multiple vertical line element model (SFI-MVLEM) available in the computational platform OpenSees, was developed by Kolozvari et al. (2015) based on the methodology proposed by Massone et al. (2006). The model incorporates the shear-flexure interaction by replacing the m uniaxial elements of the MVLEM by two-dimensional RC panel elements. The panel constitutive behavior follows the Fixed-Strut-Angle-Model (FSAM, Orakcal et al., 2019) formulation. As shown in Figure 2.9, an SFI-MVLEM element computes the vertical normal strain (ε_y) and the shear distortion (γ_{xy}) for the entire section using the same six external degrees of freedom $\{\delta_N\}$ as the MVLEM model. The element formulation considers the assumptions of plane sections remain plane and constant shear strain across the element section. To complete the strain field of each RC panel element and to improve computation efficiency compared to the model proposed by Massone et al. (2006), an additional horizontal degree of freedom is added in each one of the m number of strips $\{\delta_x\}$ to compute the unknown quantity of the horizontal normal strain (ε_x), by enforcing zero resultant horizontal normal stress ($\sigma_x = 0$). The number of degrees of freedom in a complete wall model is $N = 3 \cdot (n+1) + m \cdot n$, where n is the number of vertical SFI-MVLEM elements. The global stiffness matrix $[K]$ for a wall model is a square matrix of dimension $N \times N$, and the global force vector $\{F_{int}\}$ is of dimension $N \times 1$, the nonlinear problem to solve consist in reaching force equilibrium in each one of the N degrees of freedom. Comparisons between the analytically predicted and experimentally measured responses for reversed-cyclic loading conditions indicate an accurate prediction of lateral load versus top displacement response for all considered wall specimens (with shear span-to-depth ratios between 1.5 and 3.0) in terms of wall stiffness, lateral load capacity, and pinching behavior (Kolozvari et al., 2015). Similar to the model developed by Massone et al. (2006), due to the assumption of zero resultant horizontal stress, the model cannot accurately predict the behavior of squat walls.

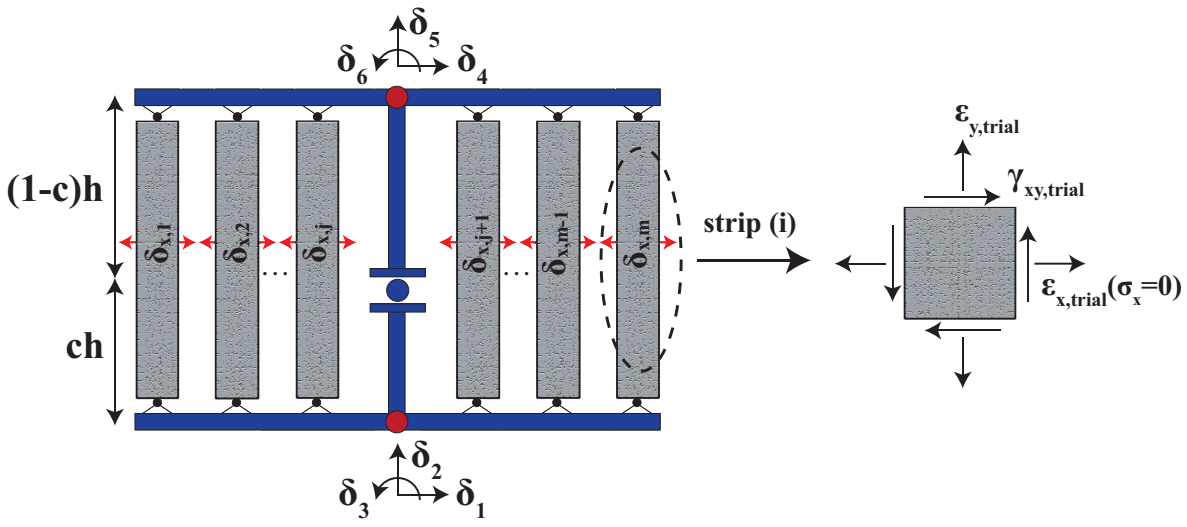

Figure 2.9: SFI-MVLEM element.

2.3.2.4. Shear-flexure interaction model with a calibrated expression for the horizontal normal strain

A couple of researches were developed to include a calibrated expression for the horizontal normal strain (ε_x) into a shear-flexure interaction model; therefore, no additional iterative procedures or degrees of freedom are incorporated into a flexural model formulation, as illustrated in Figure 2.10. The calibration performed by Massone (2010) was made over the maximum magnitude of the average normal horizontal strain over the wall height ($\varepsilon_{x,max}$), differentiating between double and single curvature conditions, and incorporating parameters such as the horizontal reinforcement ratio (ρ_h); wall height (h_w); wall length (l_w); axial load (N); concrete compressive strength (f'_c); wall cross-sectional area (A_g); and wall drift (δ). Also, a shape function was incorporated for each boundary condition to represent the distribution of the horizontal normal strain over the wall height ($\varepsilon_x(y)$). A database of two-dimensional finite element analysis of RC walls was considered to perform the calibration. For double curvature condition, the calibrated expression is presented in Equation 2.1. The shape function is obtained considering that the maximum value of the horizontal normal strain occurs at wall mid-height ($\varepsilon_{x,max} = \varepsilon_x(h_w/2)$) and tends to reduce to zero at the wall top and bottom ends, represented by Equation 2.2.

$$\varepsilon_{x,max} = 0.0033(100\rho_h + 0.25)^{-0.53}\left(\frac{h_w}{l_w} + 0.5\right)^{0.47}\left(\frac{100N}{f'_c A_g} + 5\right)^{0.25}(100\delta)^{1.4} \tag{2.1}$$

$$\frac{\varepsilon_x(y)}{\varepsilon_{x,max}} = sin^{0.75}\left(\frac{y}{h_w}\pi\right) \tag{2.2}$$

For cantilever configuration (single curvature), the calibrated expression obtained by Massone (2010) is presented in Equation 2.3. The shape function is obtained considering that the maximum value of the horizontal normal strain occurs at height $y = 0.38h_w$ and tends to reduce to zero at the wall top and bottom ends, represented by Equation 2.4.

$$\varepsilon_{x,max} = 0.0055(100\rho_h + 0.25)^{-0.44}(100\delta)^{1.4} \tag{2.3}$$

$$\frac{\varepsilon_x(y)}{\varepsilon_{x,max}} = \begin{cases} sin^{0.75}\left(\frac{y}{0.76h_w}\pi\right) & 0 \le y \le 0.38h_w \\ sin^{0.75}\left(\frac{(y+0.24h_w)}{1.24h_w}\pi\right) & 0.38h_w \le y \le h_w \end{cases} \tag{2.4}$$

The expressions obtained by Massone (2010) were incorporated into a shear-flexure interaction model. A comparison between the predicted and the experimentally measured shear strength was performed for 252 RC wall specimen tests reported in the literature. The average shear strength ratio (V_{model}/V_{test}) for all the wall specimens was 1.13, with a coefficient of variation of 0.25. The maximum and minimum strength ratios were 1.97 and 0.56, respec-

tively, although most of them range between 0.7 and 1.6 (89%). The shear-flexure model was also validated against cyclic response of RC wall specimen tests reported in the literature (Kolozvari et al., 2019), demonstrating an accurate prediction of the hysteretic behavior of shear-dominated walls.

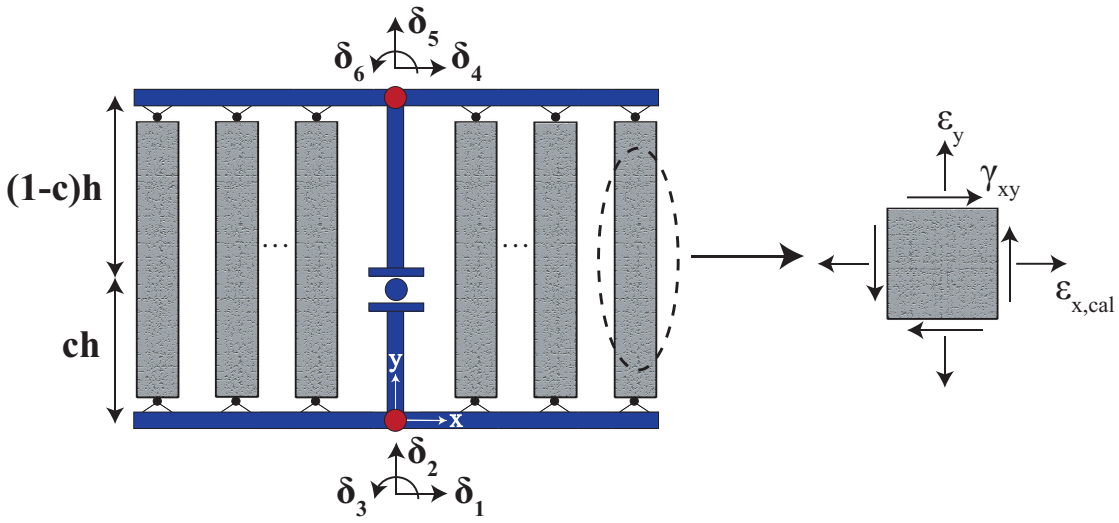

Figure 2.10: SFI element with calibrated horizontal normal strain.

Another research was developed by Massone et al. (2020). In this approach, the calibration of the horizontal normal strain (ε_x) was performed based on the vertical normal strain (ε_y) and the shear strain (γ_{xy}) of each panel element. The same database of two-dimensional finite element analysis of RC walls used by Massone (2010) was considered to perform the calibration. A single expression was obtained without distinguishing between different boundary conditions, nor wall parameters, as shown in Equation 2.5. The expression was incorporated into a shear-flexure interaction model. The shear strength ratio (V_{model}/V_{test}) was determined for 252 RC wall test specimens reported in the literature. The average shear strength ratio for all the wall specimens was 0.96, with a coefficient of variation of 0.26. The maximum strength ratio was 1.82, whereas the minimum was 0.44; however, most of them range between 0.6 and 1.4 (90%). The analytical model was validated against the cyclic response of two RC wall specimen tests reported in the literature, showing the ability of the model to accurately reproduce the hysteretic behavior of squat and slender RC walls.

$$\varepsilon_x = -0.166 \cdot |\varepsilon_y| + 0.444 \cdot |\gamma_{xy}| \tag{2.5}$$

2.4. Microscopic models for RC structural walls

Several microscopic analytical models for RC structural walls have been reported in the literature over the past years, obtaining accurate predictions with fewer limitations in their applicability than macroscopic models, due to a more generalized formulation. Some of the more relevant micro-models that represent state of the art in modeling the nonlinear response of RC structural walls include the VecTor2 wall element (Wong et al., 2013); the Fixed-Strut-Angle Finite Element Model (FSAFE; Gullu & Orakcal, 2019); a four-node quadrilateral curved shell element available in the commercial software DIANA (Diana, 2011); the Quadrilateral Layered Membrane Element with Drilling Degrees of Freedom (QLMEDD; Rojas et al., 2016); and a composite layered shell element available in the commercial software LS-DYNA (Belytschko et al., 1984); among others. The main characteristics of the aforementioned micro-models are summarized in Table 2.1, whereas the available strength degradation mechanisms of the models are presented in Table 2.2, and a typical wall discretization for each formulation is presented in Figure 2.11. A benchmarking between the five micro modeling approaches was developed by Kolozvari et al. (2019), revealing a reasonably accurate prediction, at global and local levels, of the inelastic behavior of planar RC walls for a wide range of walls characteristics regardless of the chosen formulation.

Table 2.1: Main characteristics of microscopic models for reinforced concrete walls.

Model Acronym	Number of DOFs per node	Out-of-plane behavior	Number of integration points	Inter-polation function	Layered section	Crack orientation	Shear resisting mechanisms	Definition of reinforcement
VecTor2	2	No	4	Linear	No	Rotating	No	Disc./Smear.
FSAFE	2	No	1	Linear	No	Fixed	Yes	Smeared
DIANA	2	Yes	12	Linear	Yes	Rotating	No	Discrete
QLMEDD	3	No	9	Blended	Yes	Rotating	No	Smeared
LS-DYNA	2	Yes	7	Linear	Yes	Fixed	Yes	Discrete

Table 2.2: Available strength degradation mechanisms of microscopic models.

Model Acronym	Concrete Crushing	Reinforcement Buckling	Reinforcement Fracture	Diagonal Tension	Diagonal Compresion	Shear Sliding	Out-of-plane inestability
VecTor2	Yes	Yes	Yes	Yes	Yes	Yes	No
FSAFE	Yes	No	No	Yes	Yes	Yes	No
DIANA	Yes	No	No	Yes	Yes	Yes	Yes
QLMEDD	Yes	Yes	No	Yes	Yes	No	No
LS-DYNA	Yes	Yes	No	Yes	Yes	Yes	Yes

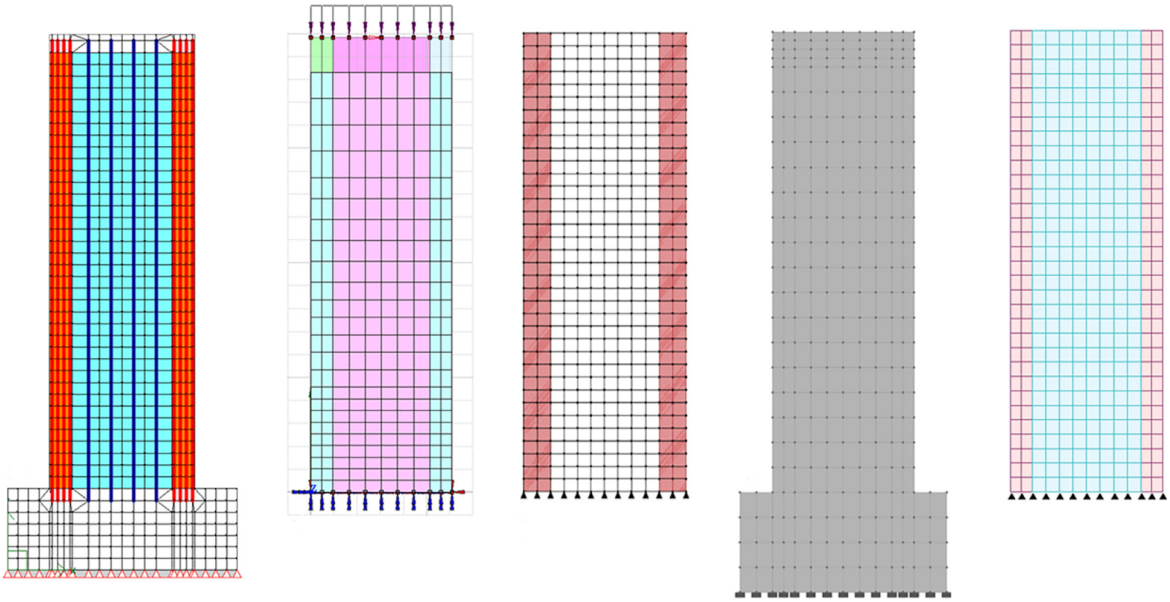

(a) VecTor2 (b) DIANA (c) FSAFE (d) QLMEDD (e) LS-DYNA

Figure 2.11: Typical wall discretization of micromodels (Kolozvari et al., 2019).

Chapter 3

Proposed Analytical Model

3.1. General description

The novel model, referred to as Efficient-Shear-Flexure-Interaction (E-SFI), was developed based on the methodology proposed by Kolozvari et al. (2015) and implemented in an in-house version of the OpenSees framework (McKenna et al., 2010). The model incorporates the shear-flexure interaction phenomenon by replacing the m number of uniaxial elements of the MVLEM by two-dimensional RC panel elements subjected to membrane actions following the Fixed-Strut-Angle-Model formulation (FSAM; Orakcal et al., 2019). As illustrated in Figure 3.1, an E-SFI element is described by six degrees of freedom, and therefore no additional degrees of freedom are incorporated into the original MVLEM formulation. The curvature of an E-SFI element is assumed to be uniform, and the resultant rotation is concentrated at height ch. A value of $c = 0.4$ is recommended based on comparison with experimental test results (Vulcano et al., 1988). The kinematic assumption of plane sections remain plane (Euler-Bernoulli hypotheses), as well as the assumption of constant shear strain along the element length, are considered for computing the axial strain (ε_y) and the shear distortion (γ_{xy}) for each panel over the entire section. To complete the strain field of a panel element, a calibrated expression for the horizontal normal strain (ε_x) in terms of internal variables of the panel, such as the shear strain (γ_{xy}) and the horizontal reinforcement ratio (ρ_h), is derived in order to obtain accurate predictions from squat to slender RC walls.

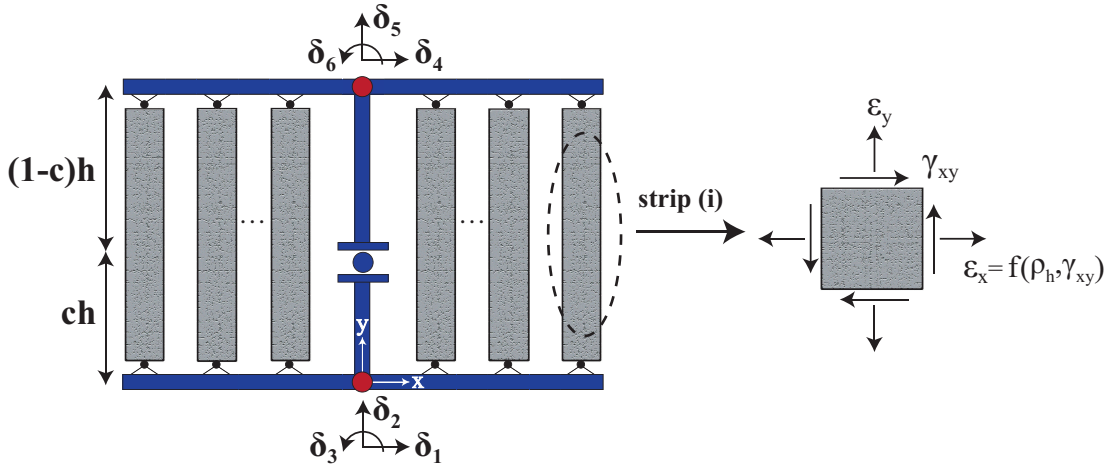

Figure 3.1: E-SFI model idealization.

3.2. Element degrees of freedom

As shown in Figure 3.2(a), an E-SFI element is characterized by two nodes located at the center of the rigid top and bottom beams, each node with three degrees of freedom that represent horizontal and vertical displacements, and rotation. Based on the six prescribed degrees of freedom $\{\delta\} = \{\delta_1\ \delta_2\ \delta_3\ \delta_4\ \delta_5\ \delta_6\}^T$, the kinematic assumption of plane sections remain plane (Euler-Bernoulli hypotheses), and the assumption of constant shear strain along wall element, the vertical normal strain (ε_y) and the shear distortion (γ_{xy}) are computed for each one of the m number of RC panel elements (macro-fibers) along the element. To complete the strain field of each panel element, a calibrated expression for the horizontal normal strain (ε_x) is incorporated. Therefore, no additional degrees of freedom nor iterative procedures are added to the original MVLEM formulation. As shown in Figure 3.2(b), a structural wall is modeled as a stack of n E-SFI elements, which are placed one upon the other, resulting in a total number of $N = 3 \cdot (n + 1)$ degrees of freedom.

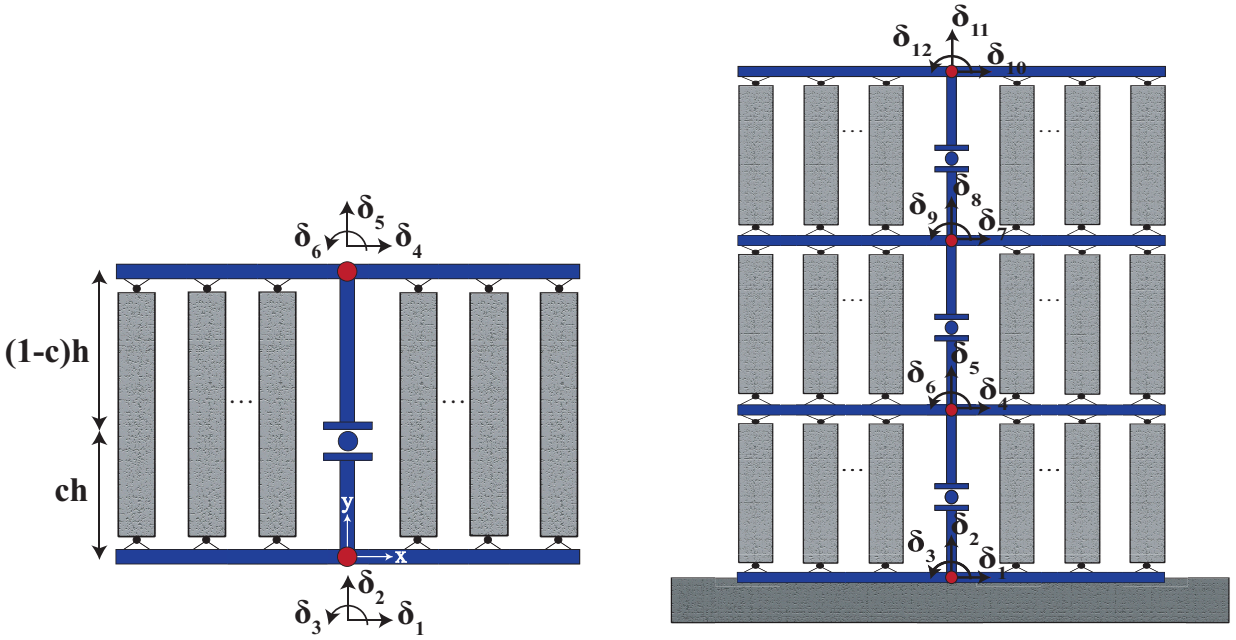

(a) E-SFI element.

(b) E-SFI wall model.

Figure 3.2: E-SFI model degrees of freedom.

3.3. Element stiffness matrix

Considering the six degrees of freedom located at the center of the rigid top and bottom beams of an E-SFI element $\{\delta\}$, the element stiffness matrix relative to these degrees of freedom $[K_e]$ is obtained as,

$$[K_e] = [\beta]^T \cdot [K] \cdot [\beta] \tag{3.1}$$

where $\{\beta\}$ denotes the transformation matrix converting the element degrees of freedom $\{\delta\}$ to the element pure deformations of extension, relative rotation at the bottom, and relative rotation at the top of each wall element, as illustrated in Figure 3.3. The transformation matrix is given by,

$$[\beta] = \begin{pmatrix} 0 & -1 & 0 & 0 & 1 & 0 \\ -1/h & 0 & 1 & 1/h & 0 & 0 \\ -1/h & 0 & 0 & 1/h & 0 & 1 \end{pmatrix} \tag{3.2}$$

and $[K]$ is the element stiffness matrix relative to the prescribed three pure deformations degrees of freedom given by the matrix presented in Equation 3.3,

$$[K] = \begin{pmatrix} \sum_{j=1}^{m} k_{y,j} & -\sum_{j=1}^{m} k_{y,j}x_j & \sum_{j=1}^{m} k_{y,j}x_j \\ & k_{sh}c^2h^2 + \sum_{j=1}^{m} k_{y,j}x_j^2 & k_{sh}c(1-c)h^2 - \sum_{j=1}^{m} k_{y,j}x_j^2 \\ symm. & & k_{sh}(1-c)^2h^2 + \sum_{j=1}^{m} k_{y,j}x_j^2 \end{pmatrix} \tag{3.3}$$

where $k_{y,j}$ is the vertical stiffness of the j-th RC panel, and k_{sh} is the shear element stiffness calculated as the sum of the shear stiffness of all m RC panel elements along the wall element length, as shown in Equation 3.4.

$$k_{sh} = \sum_{j=1}^{m} k_{sh,j} \tag{3.4}$$

For any prescribed strain field of the j-th RC panel, the axial vertical stiffness ($k_{y,j}$) and the shear stiffness ($k_{sh,j}$) for the panel is obtained by,

$$k_{y,j} = \left(\frac{\partial F_y}{\partial u_y}\right)_j = \left(\frac{\partial F_y}{\partial \sigma_y}\right)_j \cdot \left(\frac{\partial \sigma_y}{\partial \varepsilon_y}\right)_j \cdot \left(\frac{\partial \varepsilon_y}{\partial u_y}\right)_j = \left(\frac{\partial \sigma_y}{\partial \varepsilon_y}\right)_j \cdot \frac{A_{y,j}}{h} \tag{3.5}$$

$$k_{sh,j} = \left(\frac{\partial F_{sh}}{\partial u_{sh}}\right)_j = \left(\frac{\partial F_{sh}}{\partial \tau_{xy}}\right)_j \cdot \left(\frac{\partial \tau_{xy}}{\partial \gamma_{xy}}\right)_j \cdot \left(\frac{\partial \gamma_{xy}}{\partial u_{sh}}\right)_j = \left(\frac{\partial \tau_{xy}}{\partial \gamma_{xy}}\right)_j \cdot \frac{A_{y,j}}{h} \tag{3.6}$$

where $A_{y,j}$ is the cross-sectional area of the j-th RC panel, and the value of the partial derivatives are obtained from the RC panel partial stiffness matrix $[K_p]_j$ shown in Equation 3.7.

$$[K_p]_j = \begin{pmatrix} \frac{\partial \sigma_x}{\partial \varepsilon_x} & \frac{\partial \sigma_x}{\partial \varepsilon_y} & \frac{\partial \sigma_x}{\partial \gamma_{xy}} \\ \frac{\partial \sigma_y}{\partial \varepsilon_x} & \frac{\partial \sigma_y}{\partial \varepsilon_y} & \frac{\partial \sigma_y}{\partial \gamma_{xy}} \\ \frac{\partial \tau_{xy}}{\partial \varepsilon_x} & \frac{\partial \tau_{xy}}{\partial \varepsilon_y} & \frac{\partial \tau_{xy}}{\partial \gamma_{xy}} \end{pmatrix} \tag{3.7}$$

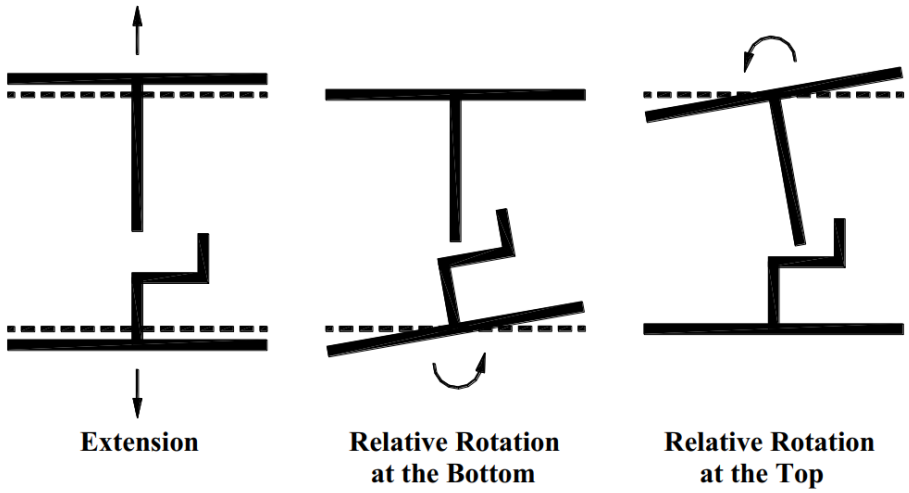

Figure 3.3: Element pure deformations (Orakcal & Wallace, 2006).

3.4. Element force vector

For an E-SFI element, the resisting force vector relative to the six degrees of freedom is obtained from equilibrium as,

$$\{F_e\} = \left\{ F_{sh};\ -\sum_{j=1}^{m} F_{y,j};\ -F_{sh}ch - \sum_{j=1}^{m} F_{y,j}x_j;\ -F_{sh};\ \sum_{j=1}^{m} F_{y,j};\ -F_{sh}(1-c)h + \sum_{j=1}^{m} F_{y,j}x_j \right\}^T \tag{3.8}$$

where F_{sh} is the resultant force in the horizontal direction obtained as the sum of the shear force on each macro-fiber, as presented in Equation 3.9.

$$F_{sh} = \sum_{j=1}^{m} F_{sh,j} \tag{3.9}$$

The values of $F_{y,j}$ and $F_{sh,j}$ correspond to the force in the vertical and horizontal direction, respectively, for the j-th RC panel element, given by,

$$F_{y,j} = \sigma_{y,j} \cdot A_{y,j} \tag{3.10}$$

$$F_{sh,j} = \tau_{xy,j} \cdot A_{y,j} \tag{3.11}$$

where $\sigma_{y,j}$ and $\tau_{xy,j}$ are the axial vertical and shear stresses, respectively, obtained from the constitutive RC panel behavior for the applied strain field, and $A_{y,j}$ is the panel tributary area where the stresses are acting.

3.5. Vertical normal strain and shear strain acting on RC panel elements

Considering the six nodal degrees of freedom $\{\delta\}$ of an E-SFI element in addition to the Euler-Bernoulli hypotheses, the vector containing the values of vertical deformation at each one of the m RC panel elements $\{u_y\} = \{u_{y,1}\ u_{y,2}\ \dots\ u_{y,m}\}^T$ is computed as,

$$\{u_y\} = [a] \cdot \{\delta\} \tag{3.12}$$

where $[a]$ is the geometric transformation matrix that converts the nodal degrees of freedom to the element vertical deformations given by Equation 3.13.

$$[a] = \begin{pmatrix} 0 & -1 & -x_1 & 0 & 1 & x_1 \\ \vdots & \vdots & \vdots & \vdots & \vdots & \vdots \\ 0 & -1 & -x_j & 0 & 1 & x_j \\ \vdots & \vdots & \vdots & \vdots & \vdots & \vdots \\ 0 & -1 & -x_m & 0 & 1 & x_m \end{pmatrix} \tag{3.13}$$

As shown in Equation 3.14, the vertical normal strain of the j-th RC panel ($\varepsilon_{y,j}$) is calculated by dividing the vertical deformation of the j-th RC panel ($u_{y,j}$) by the element height (h).

$$\varepsilon_{y,j} = \frac{u_{y,j}}{h} \tag{3.14}$$

The shear deformation of an E-SFI element (u_{sh}) is computed at height ch based on the element degrees of freedom $\{\delta\}$ as,

$$u_{sh} = \{b\}^T \cdot \{\delta\} \tag{3.15}$$

where $\{b\}$ is the geometric transformation matrix that converts the nodal degrees of freedom to the element shear deformation given by Equation 3.16.

$$\{b\}^T = \{1; \quad 0; \quad -c \cdot h; \quad -1; \quad 0; \quad -(1-c) \cdot h\} \tag{3.16}$$

Assuming a constant distribution of the shear strain along the wall cross-section, the shear strain of the j-th RC panel ($\gamma_{xy,j}$) is calculated by dividing the shear deformation (u_{sh}) by the element height (h), as shown in Equation 3.17.

$$\gamma_{xy,j} = -\frac{u_{sh}}{h} \tag{3.17}$$

To complete the strain field of the j-th RC panel element ($\varepsilon_{x,j}, \varepsilon_{y,j}, \gamma_{xy,j}$), a calibrated expression for the horizontal normal strain ($\varepsilon_{x,j}$) is incorporated into the model formulation, and therefore the resultant stress field ($\sigma_{x,j}, \sigma_{y,j}, \tau_{xy,j}$) of the panel is obtained. The derivation of the expression to compute the horizontal normal strain is discussed in Section 3.6.

3.6. Horizontal normal strain acting on RC panel elements

As mentioned in Section 2.3.2.3, a couple of work have been developed to include a calibrated expression for the horizontal normal strain (ε_x) into a shear-flexure interaction model. The model proposed by Massone (2010) has the main disadvantage that its implementation for general purpose is unclear (e.g., walls with openings; wall segments; walls with setbacks) due to the use of the expression for each boundary condition, and the incorporation of global wall parameters such as the wall height(h_w); wall length (l_w); axial load level (N/f'_cA_g); and wall drift (δ). The aforementioned issue was corrected by the model proposed by Massone et al. (2020), by calibrating at panel level in terms of the vertical normal strain (ε_y) and the shear strain (γ_{xy}); however, negative values of the horizontal normal strain (ε_x) are obtained when the wall is flexural-dominated because the magnitude of the vertical normal strain (ε_y) is more relevant than the magnitude of the shear strain (γ_{xy}), indicating a contraction of the wall, which is inconsistent with the experimentally observed behavior. Furthermore, the model is insensitive to changes in the horizontal reinforcement ratio (ρ_h). Based on both prior experiences, a new calibration for the horizontal normal strain (ε_x) is proposed using as the principal variable the shear strain (γ_{xy}) and incorporating the effect of the horizontal reinforcement ratio (ρ_h). The expression is calibrated using a database of two-dimensional finite element analysis of RC walls, with a unique expression to cover all boundary conditions and wall parameters.

3.6.1. Finite element analysis database

A database of finite element analysis (FEA) of RC walls is considered to perform the calibration of the horizontal normal strain (ε_x). The database was developed by Massone (2010) using a conventional two-dimensional finite element model (2D-FEM) formulation. A wall element is discretized in a series of 4-node rectangular elements with linear interpolation between the nodal displacements and a single Gauss integration point at element centroid. The FEA database is comprised of 262 cases, including the traditional boundary conditions, single and double curvature (131 cases for each one), and different parameters for a wide range of values such as: aspect ratio (h_w/l_w = 0.33 to 1.4); vertical web distributed reinforcement ratio (ρ_{wv} = 0 to 1 %); horizontal web distributed reinforcement ratio (ρ_{wh} = 0 to 1 %); longitudinal boundary reinforcement ratio (ρ_b = 1 to 6 %); and axial load (N = 0 to $0.3f'_cA_g$, where f'_c is the compressive strength of concrete, and A_g correspond to the wall cross-sectional area). A preliminary study of the importance of each parameter over the horizontal expansion (ε_x) indicates that the impact of material properties (f'_c = 30 to 50 MPa, and f_y = 280 to 420 MPa) is less important than the other parameters; therefore, the database does not include variation in these parameters. The wall models were discretized in eight horizontal and eight vertical panels, and the analysis was performed for monotonic loading until achieving the shear strength of the wall. To validate the results, the 2D-FEM model prediction was contrasted with the experimentally measured response of nine RC wall specimen tests, yielding good overall predictions in terms of shear strength, stiffness and horizontal normal strain profiles (Massone, 2010).

3.6.2. Sensitivity analysis of the relation between the horizontal normal strain and the shear strain

A sensitivity analysis was performed to study the relation between the horizontal normal strain (ε_x) and the shear strain (γ_{xy}) using the data provided by the finite element analysis database until reach the wall shear strength. For this purpose, a base case under cantilever configuration was selected with the following properties: h_w = 1500 mm; l_w = 3000 mm; t_w = 150 mm; f'_c = 30 MPa; f_y = 420 MPa; $\rho_{h,web}$ = 0.5 %; $\rho_{v,web}$ = 0.5 %; ρ_b = 6.0 %; and $N = 0.15A_gf'_c$. The average horizontal normal strain was obtained at each vertical level, and the maximum value over the height was stored for each step analysis ($\varepsilon_{x,max}$) with the respective value of the shear strain (γ_{xy}). As shown in Figure 3.4, the ratio between the maximum mean horizontal normal strain over the height ($\varepsilon_{x,max}$) and the shear strain (γ_{xy}), referred to as strain-ratio, was plotted over the shear strain (γ_{xy}) for the base case (blue line), and for different wall parameters. Figure 3.4(a) reveals that the axial load acting on the wall affects the ductility; however, it has a reduced effect on the maximum strain-ratio. Figure 3.4(b) indicates that the effect of the vertical reinforcement ratio is not relevant to perform the calibration. By contrast, Figure 3.4(c) reveals that the horizontal reinforcement ratio plays a significant role in the maximum value of the strain-ratio; therefore, this variable is incorporated to perform the calibration. Although external parameters are not intended to be included in the calibration, the effect of the aspect ratio (h_w/l_w) was analyzed in Figure 3.4(d), indicating that maximum strain-ratio increases with the aspect ratio. The sensitivity analysis was performed for different cases of the finite element analysis database, revealing a similar trend for most of them. It must be noted that the relation between the strain-ratio ($\varepsilon_{x,max}/\gamma_{xy}$) and the shear strain ($\gamma_{xy}$) is slightly nonlinear, described by an initial increasing

zone and tend to be constant as the magnitude of the shear strain increase; this behavior is incorporated to perform the calibration by the use of a shape function.

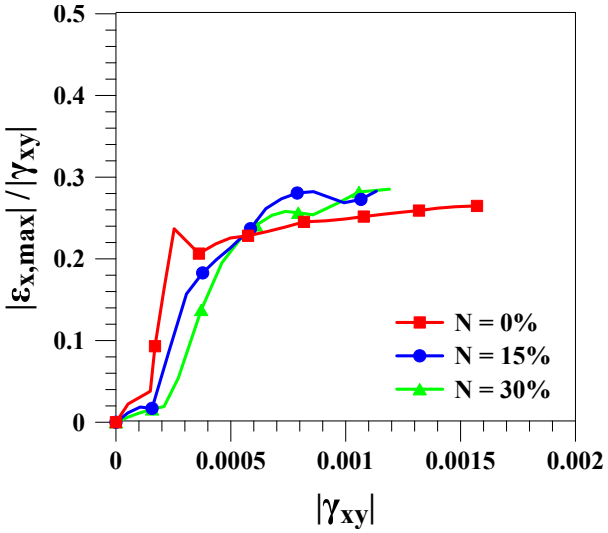

(a) Effect of the axial load.

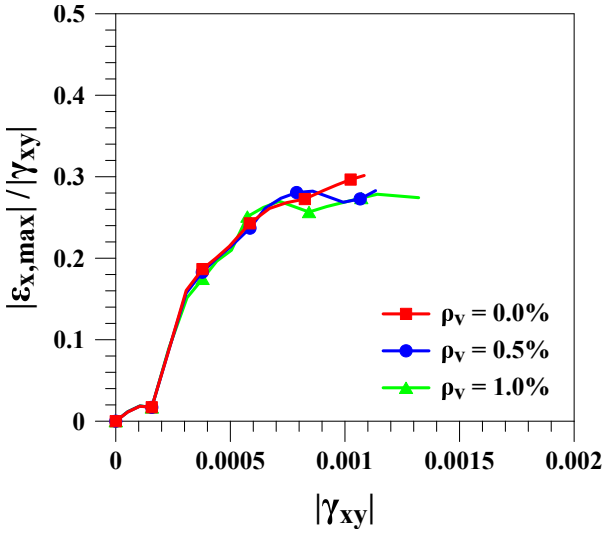

(b) Effect of the vertical reinforcement ratio.

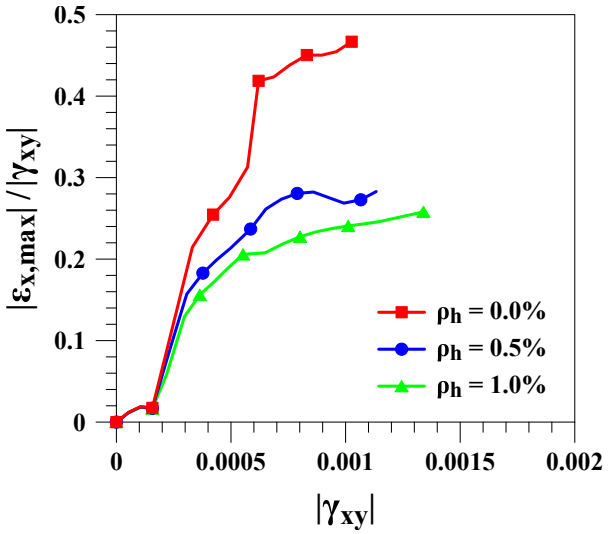

(c) Effect of the horizontal reinforcement ratio.

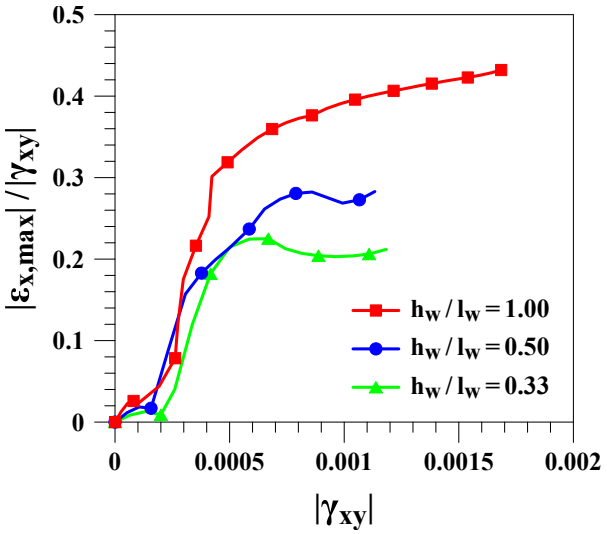

(d) Effect of the aspect ratio.

Figure 3.4: Sensitivity analysis of the relation between the horizontal normal strain and the shear strain.

3.6.3. Calibration of the horizontal normal strain

In this formulation, a unique calibrated expression for the horizontal normal strain (ε_x) using internal data of each RC panel is generated. Although the database includes information of the post-peak response of the 2D-FEM RC wall analysis, they were removed to perform the calibration to avoid damage localization issues. Based on the observed behavior in Section 3.6.2, the calibrated expression for the horizontal normal strain (ε_x) at panel level has the form of $\varepsilon_x = A(\rho_h) \cdot \Phi(\gamma_{xy}) \cdot |\gamma_{xy}|$, where $A(\rho_h)$ is the amplitude of the calibrated expression as a function of the horizontal reinforcement ratio ρ_h(-) to represent the maxi-

mum strain-ratio, $\Phi(\gamma_{xy})$ is a shape function as a function of the shear strain to represent the observed nonlinear behavior, and γ_{xy} is the shear strain of the panel at the current step. The best-fit curve analysis was performed by minimizing the mean squared error (MSE) of approximately 400.000 data points. Subsequently, the numbers of the fitted curve were rounded, obtaining the calibrated expression shown in Equation 3.18.

$$\varepsilon_x = 0.55\,(1+\rho_h)^{-60} \cdot \left(1 - 3^{-800\cdot|\gamma_{xy}|}\right) \cdot |\gamma_{xy}| \tag{3.18}$$

As shown in Figure 3.5, the horizontal normal strain values obtained by evaluating the calibration ($\varepsilon_{x,CAL}$) were plotted over those values provided by the finite element analysis database ($\varepsilon_{x,FEM}$), obtaining an R-squared value of 0.83. Although a significant dispersion is observed, it must be noted that the calibrated expression covers all possible RC wall configurations and boundary conditions with a single expression.

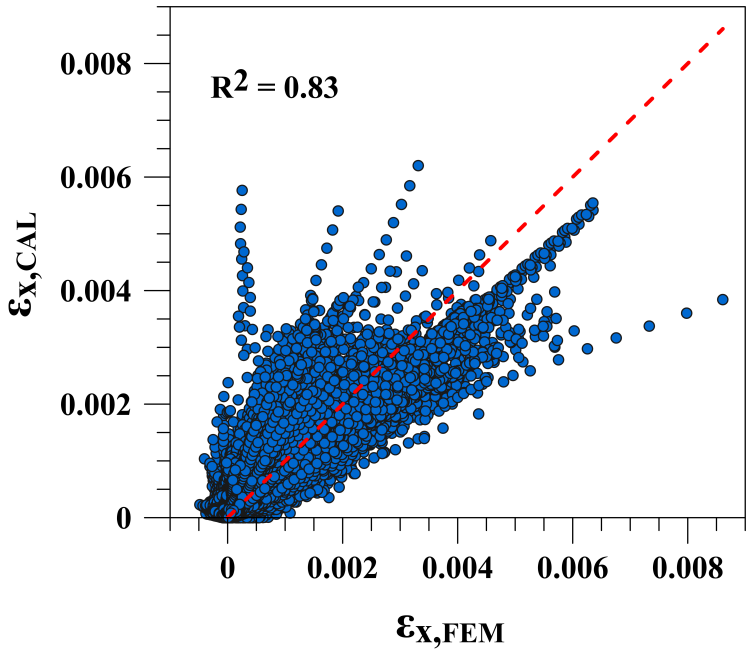

Figure 3.5: Predicted versus expected values of the horizontal normal strain.

Figure 3.6 shows the average horizontal normal strain profile at different drift levels (δ) obtained by the finite element analysis (FEM) and by evaluating the calibration (CAL) for the base case wall configuration described in Section 3.6.2 under single and double curvature conditions. The calibrated expression accurately reproduces the shape and magnitude of the horizontal normal strain profiles; however, near the boundary condition zones, the magnitude is generally overestimated. This behavior is observed in most 262 RC finite element analysis of the database.

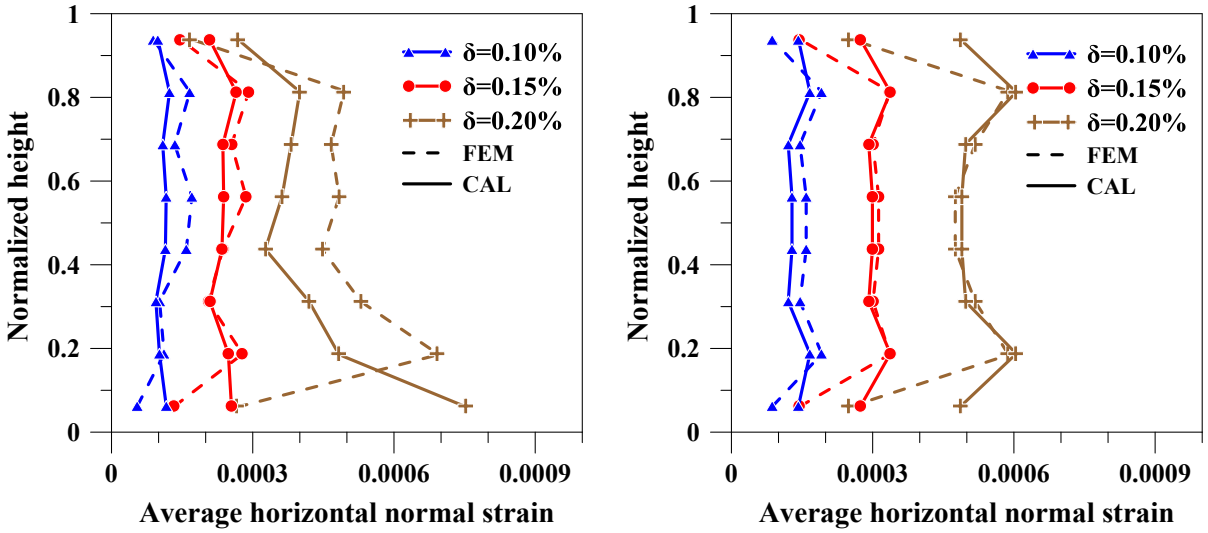

(a) Single curvature. (b) Double curvature.

Figure 3.6: Average horizontal normal strain profiles for the base case wall configuration of the finite element analysis database under different boundary conditions.

3.7. Reinforced concrete panel model

The adopted constitutive reinforced concrete panel behavior is the so-called Fixed-Strut-Angle-Model (FSAM; Orakcal et al., 2019) implemented in OpenSees by Kolozvari et al. (2018). As depicted in Figure 3.7, the FSAM is described by three stages: uncracked, after the formation of the first crack, and after the formation of the second crack. The initial state is described by a rotating-angle approach until the formation of the first crack; then, a fixed-angle approach that inherently sets the principal directions coincidentally with parallel and perpendicular directions to the first crack is used. The concrete stresses are obtained by applying a stress-strain uniaxial constitutive model in each principal direction (biaxial directions), whereas the uniaxial stress developing in the reinforcing steel bars are obtained using a uniaxial constitutive model in their longitudinal direction. Additionally, the panel model incorporates shear stress transfer across cracks due to shear aggregate interlock and dowel action, neglecting their effects in the principal stress directions of concrete.

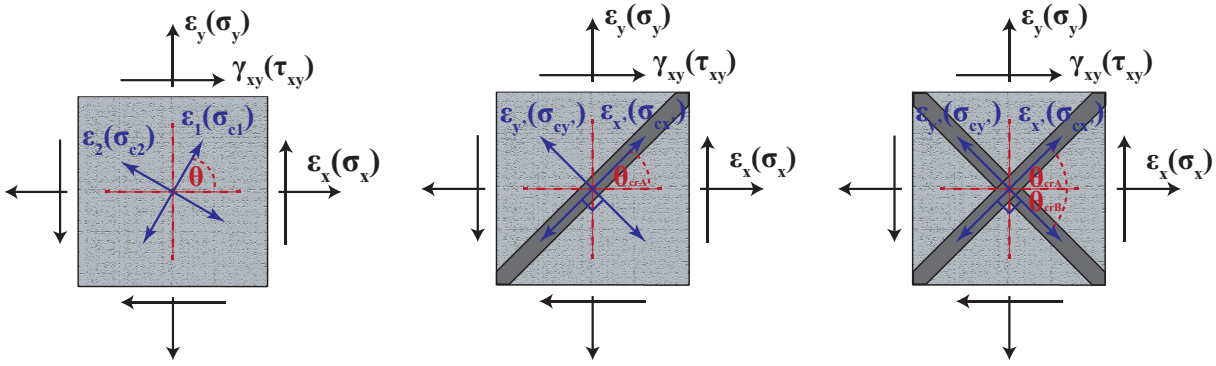

(a) uncracked behavior. (b) after the first crack. (c) after the second crack.

Figure 3.7: Concrete behavior in FSAM.

3.7.1. Uncracked panel response

The initial state of concrete is defined by the uncracked panel response, following a rotating-strut (rotating-crack) approach similar to the Modified Compression Field Theory (Vecchio & Collins, 1986) and the Rotating Angle Softened Truss Model (Pang & Hsu, 1995). In this stage, materials response is described by monotonic stress-strain relationships. Furthermore, principal strain directions are assumed to coincide with principal stress directions. For an applied strain field $(\varepsilon_x, \varepsilon_y, \gamma_{xy})$ on the panel element, the principal strain direction (θ) and the principal strains $(\varepsilon_1,\ \varepsilon_2)$ are computed as,

$$\theta = \frac{1}{2} \cdot \arctan\left(\frac{\gamma_{xy}}{\varepsilon_x - \varepsilon_y}\right) \tag{3.19}$$

$$\varepsilon_1 = \frac{\varepsilon_x + \varepsilon_y}{2} + \frac{\gamma_{xy}}{2 \cdot \sin(2\theta)} \tag{3.20}$$

$$\varepsilon_2 = \frac{\varepsilon_x + \varepsilon_y}{2} - \frac{\gamma_{xy}}{2 \cdot \sin(2\theta)} \tag{3.21}$$

The concrete principal stresses $(\sigma_{c1}, \sigma_{c2})$ are calculated based on the monotonic uniaxial stress-strain model of the material for the principal strains $(\varepsilon_1, \varepsilon_2)$. The uniaxial stress developing in the reinforcing steel bars in x-y directions $(\sigma_{sx}, \sigma_{sy})$ are obtained using the monotonic envelope of the material for the applied strains $(\varepsilon_x, \varepsilon_y)$, and are smeared over the panel based on the reinforcement ratios (ρ_{sx}, ρ_{sy}). The resultant stress field of the RC panel in Cartesian coordinates is given by,

$$\sigma_x = \frac{\sigma_{c1} + \sigma_{c2}}{2} + \frac{\sigma_{c1} - \sigma_{c2}}{2} \cdot \cos(2\theta) + \rho_{sx} \cdot \sigma_{sx} \tag{3.22}$$

$$\sigma_y = \frac{\sigma_{c1} + \sigma_{c2}}{2} - \frac{\sigma_{c1} - \sigma_{c2}}{2} \cdot \cos(2\theta) + \rho_{sy} \cdot \sigma_{sy} \tag{3.23}$$

$$\tau_{xy} = \frac{\sigma_{c1} - \sigma_{c2}}{2} \cdot \sin(2\theta) \tag{3.24}$$

3.7.2. Panel response after the formation of the first crack

The first crack (first fixed strut) is generated when the value of the principal tensile strain exceeds the monotonic cracking strain of concrete (ε_t) for the first time. The direction parallel to the crack (θ_{crA}) is assigned as the first fixed strut direction. For the following load steps, although principal strain direction continues to rotate based on the applied strain field, it is considered that principal stress direction remains parallel and perpendicular to the first fixed strut direction, implying a condition of zero shear stress developing along the crack. In this stage, materials behavior is represented by uniaxial hysteretic stress-strain relationships. For

an applied strain field $(\varepsilon_x, \varepsilon_y, \gamma_{xy})$ on the panel element, the strains in directions parallel and perpendicular to the first crack ($\varepsilon_{x'}$, $\varepsilon_{y'}$), and the shear strain along the crack surface ($\gamma_{x'y'}$) are defined by,

$$\varepsilon_{x'} = \frac{\varepsilon_x + \varepsilon_y}{2} + \frac{\varepsilon_x - \varepsilon_y}{2} \cdot \cos(2\theta_{crA}) + \frac{\gamma_{xy}}{2} \cdot \sin(2\theta_{crA}) \tag{3.25}$$

$$\varepsilon_{y'} = \frac{\varepsilon_x + \varepsilon_y}{2} - \frac{\varepsilon_x - \varepsilon_y}{2} \cdot \cos(2\theta_{crA}) - \frac{\gamma_{xy}}{2} \cdot \sin(2\theta_{crA}) \tag{3.26}$$

$$\gamma_{x'y'} = \gamma_{xy} \cdot \cos(2\theta_{crA}) - (\varepsilon_x - \varepsilon_y) \cdot \sin(2\theta_{crA}) \tag{3.27}$$

The concrete principal stresses $(\sigma_{cx'}, \sigma_{cy'})$ are computed based on the hysteretic stress-strain behavior of the material for the strains in directions parallel and perpendicular to the first crack $(\varepsilon_{x'}, \varepsilon_{y'})$. The uniaxial stress developing in the reinforcing steel bars in x-y directions $(\sigma_{sx}, \sigma_{sy})$ are obtained using the hysteretic stress-strain behavior of the material for the applied strains $(\varepsilon_x, \varepsilon_y)$, and are smeared over the panel based on the reinforcement ratios (ρ_{sx}, ρ_{sy}). The resultant stress field of the RC panel in Cartesian coordinates is given by,

$$\sigma_x = \frac{\sigma_{cx'} + \sigma_{cy'}}{2} + \frac{\sigma_{cx'} - \sigma_{cy'}}{2} \cdot \cos(2\theta_{crA}) + \rho_{sx} \cdot \sigma_{sx} \tag{3.28}$$

$$\sigma_y = \frac{\sigma_{cx'} + \sigma_{cy'}}{2} - \frac{\sigma_{cx'} - \sigma_{cy'}}{2} \cdot \cos(2\theta_{crA}) + \rho_{sy} \cdot \sigma_{sy} \tag{3.29}$$

$$\tau_{xy} = \frac{\sigma_{cx'} - \sigma_{cy'}}{2} \cdot \sin(2\theta_{crA}) \tag{3.30}$$

3.7.3. Panel response after the formation of the second crack

The second crack (second fixed strut) is formed when the perpendicular direction to the first fixed strut reaches the cyclic cracking strain; therefore, this approach considers the first and second strut perpendicular to each other due to formulation simplicity. In this stage, the concrete is simulated by two independent struts (strut A and B), working under interchanging compression and tension based on the applied strain field. Furthermore, materials behavior is defined by uniaxial hysteretic stress-strain relationships. The direction parallel to the second strut (θ_{crB}) is given by $\theta_{crB} = \theta_{crA} \pm \pi/2$. For an applied strain field $(\varepsilon_x, \varepsilon_y, \gamma_{xy})$ on the panel element, the uniaxial strains acting in direction parallel to the first and second crack ($\varepsilon_{x'}$, $\varepsilon_{y'}$), and the shear strain along the two crack surfaces ($\gamma_{x'y'A}$, $\gamma_{x'y'B}$) are defined by,

$$\varepsilon_{x'} = \frac{\varepsilon_x + \varepsilon_y}{2} + \frac{\varepsilon_x - \varepsilon_y}{2} \cdot \cos(2\theta_{crA}) + \frac{\gamma_{xy}}{2} \cdot \sin(2\theta_{crA}) \tag{3.31}$$

$$\varepsilon_{y'} = \frac{\varepsilon_x + \varepsilon_y}{2} + \frac{\varepsilon_x - \varepsilon_y}{2} \cdot \cos(2\theta_{crB}) + \frac{\gamma_{xy}}{2} \cdot \sin(2\theta_{crB}) \tag{3.32}$$

$$\gamma_{x'y'A} = \gamma_{xy} \cdot \cos(2\theta_{crA}) - (\varepsilon_x - \varepsilon_y) \cdot \sin(2\theta_{crA}) \tag{3.33}$$

$$\gamma_{x'y'B} = \gamma_{xy} \cdot \cos(2\theta_{crB}) - (\varepsilon_x - \varepsilon_y) \cdot \sin(2\theta_{crB}) \tag{3.34}$$

The concrete principal stresses $(\sigma_{cx'}, \sigma_{cy'})$ are computed through the hysteretic constitutive relationship of the material in directions parallel to the first and second crack $(\varepsilon_{x'}, \varepsilon_{y'})$. The stresses developed by concrete struts (A and B) are back-transformed in x-y coordinates by using transformation equations as follow,

$$\sigma_{cxA} = \frac{\sigma_{cx'} + 0}{2} + \frac{\sigma_{cx'} - 0}{2} \cdot \cos(2\theta_{crA}) \tag{3.35}$$

$$\sigma_{cyA} = \frac{\sigma_{cx'} + 0}{2} - \frac{\sigma_{cx'} - 0}{2} \cdot \cos(2\theta_{crA}) \tag{3.36}$$

$$\tau_{cxyA} = \frac{\sigma_{cx'} - 0}{2} \cdot \sin(2\theta_{crA}) \tag{3.37}$$

$$\sigma_{cxB} = \frac{\sigma_{cy'} + 0}{2} + \frac{\sigma_{cy'} - 0}{2} \cdot \cos(2\theta_{crB}) \tag{3.38}$$

$$\sigma_{cyB} = \frac{\sigma_{cy'} + 0}{2} - \frac{\sigma_{cy'} - 0}{2} \cdot \cos(2\theta_{crB}) \tag{3.39}$$

$$\tau_{cxyB} = \frac{\sigma_{cy'} - 0}{2} \cdot \sin(2\theta_{crB}) \tag{3.40}$$

The uniaxial stress developing in the reinforcing steel bars in x-y directions $(\sigma_{sx}, \sigma_{sy})$ are obtained using the hysteretic stress-strain behavior of the material for the applied strains $(\varepsilon_x, \varepsilon_y)$, and are smeared over the panel based on the reinforcement ratios (ρ_{sx}, ρ_{sy}). The resultant stress field of the RC panel in Cartesian coordinates is given by,

$$\sigma_x = \sigma_{cxA} + \sigma_{cxB} + \rho_{sx} \cdot \sigma_{sx} \tag{3.41}$$

$$\sigma_y = \sigma_{cyA} + \sigma_{cyB} + \rho_{sy} \cdot \sigma_{sy} \tag{3.42}$$

$$\tau_{xy} = \tau_{cxyA} + \tau_{cxyB} \tag{3.43}$$

3.7.4. Shear stress transfer across cracks

The shear aggregate interlock model along a crack is defined by simple hysteretic rules, as depicted in Figure 3.8. The model starts with a linear loading/unloading behavior that relates the sliding shear strain along a crack to the shear stress developing along the crack surface. The constitutive model sets to zero the shear stress when the concrete normal stress in the perpendicular direction to the crack is tensile (crack open); and is bounded by the product of a friction coefficient (η) and the concrete normal stress in the perpendicular direction to the crack (σ_{cr}) when the concrete normal stress perpendicular to the crack is compressive (crack closed). The linear unloading/reloading slope of the shear stress versus sliding strain relationship is taken as $G = 0.4E_c$, where E_c is the elastic modulus of concrete.

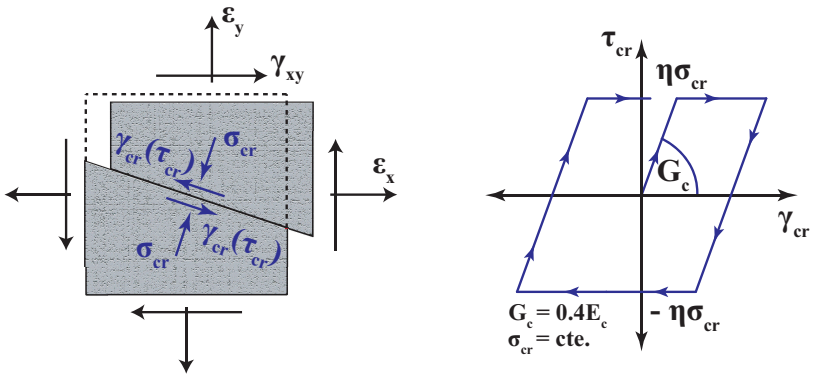

Figure 3.8: Shear aggregate interlock model.

Figure 3.9 illustrates the adopted dowel action model, as proposed by Kolozvari (2018). The contribution of reinforcing steel to shear resistance is modeled by a simple linear elastic model that relates the shear strain acting in the horizontal plane of the wall (γ_{xy}) to the resulting shear stress (τ_{sxy}). The model is characterized by an elastic modulus taken as a fraction (α) of the elastic modulus of steel (E_s). The optimal value of the the friction coefficient (η) and the fraction coefficient (α) for the wall model is discussed in Chapter 4 (Section 4.3) based on comparisons between model prediction and experimental results of RC wall specimen tests.

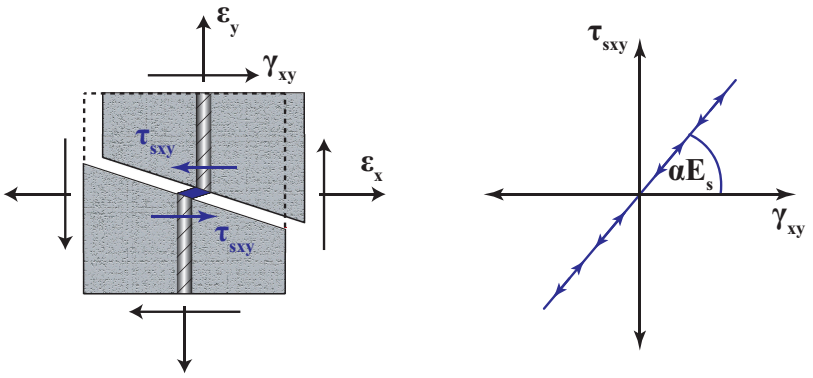

Figure 3.9: Dowel action model.

3.8. Material constitutive models

A description of the uniaxial hysteretic models for concrete and reinforcing steel; compression softening in concrete; tension stiffening effect on concrete and steel; and biaxial damage on concrete, are summarized in the following sub-sections.

3.8.1. Constitutive model for concrete

The nonlinear hysteretic constitutive model developed by Chang & Mander (1994) was selected in this study to represent the stress-strain behavior of concrete. The model is available in OpenSees as implemented by Kolozvari et al. (2018). The material model is a refined, rule-based, and non-dimensional model that can simulate the hysteretic behavior under generalized load conditions for ordinary or high-strength, confined or unconfined concrete, shown in Figure 3.10. The constitutive model formulation incorporates some important features such as continuous hysteretic response under cyclic compression and tension, the progressive degradation of stiffness at unloading and reloading curves, and the effects of gradual crack closure and tension stiffening. The model envelope is defined by the peak coordinate for compression (ε_c, f'_c) and tension (ε_t, f_t); the elastic modulus of concrete (E_c); the Tsai's (Tsai, 1988) equation shape factor (r); and the critical strain (ε_{cr}) where the envelope curve starts following a straight line. For cyclic response, several internal calibrated parameters and key points $(E_{sec}, E_{pl}, \varepsilon_{pl}, \varepsilon_{c0}, \Delta f, \Delta\varepsilon, etc.)$ allows to define the complete hysteretic behavior.

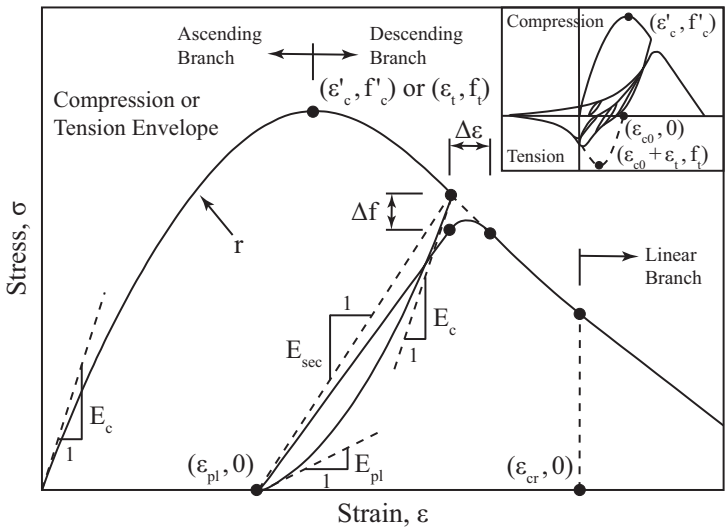

Figure 3.10: Envelope of concrete constitutive model.

According to empirical relationships derived by Chan & Mander (1994), the parameters E_c, ε'_c and r for confined and unconfined concrete, can be calculated as a function of the compressive strength f'_c (MPa) as,

$$E_c = 8200 \cdot (f'_c)^{3/8} \quad (MPa) \tag{3.44}$$

$$\varepsilon'_c = \frac{(f'_c)^{1/4}}{1150} \tag{3.45}$$

$$r = \frac{f'_c}{5.2} - 1.9 \tag{3.46}$$

3.8.2. Constitutive model for reinforcing steel

The nonlinear hysteretic constitutive model of Menegotto & Pinto (1973) as extended by Filippou et al. (1983) to incorporate the isotropic hardening effects and extended by Kolozvari et al. (2018) to overcome stress overshooting, was selected in this study to represent the stress-strain behavior of reinforcing steel. The model is available in OpenSees as implemented by Kolozvari et al. (2018). It can be observed from Figure 3.11 that the constitutive model is in the form of curved transitions, each from a straight-line asymptote with slope E_0 to another straight-line asymptote with slope $E_1 = b \cdot E_0$. The model envelope is defined by the yield strength (f_y); the initial tangent modulus (E_0); the strain hardening ratio (b); and the initial value of the curvature (R_0). To define the cyclic response, the curvature degradation parameters (a_1, a_2) must be defined, and internally defined key parameters and points ($\xi_1, \xi_2, \varepsilon_0, \sigma_0, \varepsilon_r, \sigma_r, etc.$) are used to define the complete hysteretic behavior. In this study, two sets of values for parameters R_0, a_1 and a_2 are used, based on prior research studies of cyclic test on reinforcing steel bars, which are: (1) $R_0 = 20$, $a_1 = 18.5$, $a_2 = 0.15$, as suggested by Menegotto & Pinto (1973); and (2) $R_0 = 20$, $a_1 = 18.5$, $a_2 = 0.0015$, as suggested by Elmorsi et al. (1998).

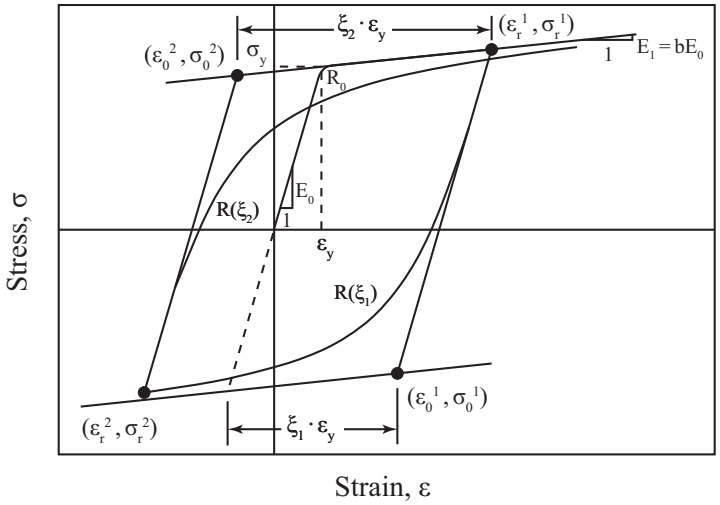

Figure 3.11: Hysteretic constitutive model of steel.

3.8.3. Compression softening in concrete

The compression softening effect is the experimentally observed (e.g., Vecchio & Collins, 1986) reduction in the strength and stiffness of the compressive principal direction of the concrete, due to presence of tensile strains in the perpendicular principal direction; therefore, as illustrated in Figure 3.12, the response of RC panel elements under membrane actions could be substantially different that of plain uniaxially compressed concrete. Most compression softening models were formulated for monotonic loading; however, some of them were implemented into cyclic analysis method (e.g., Belarbi & Hsu, 1995; Vecchio & Collins, 1993).

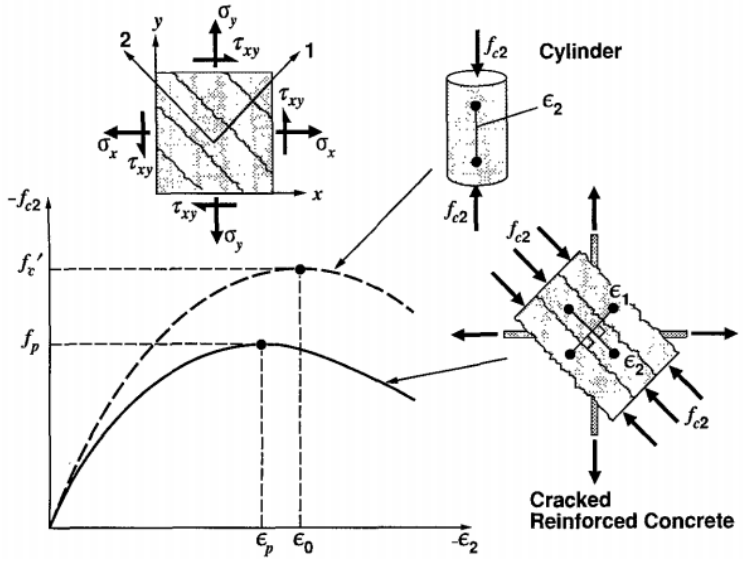

Figure 3.12: Deteriorated compression response in cracked reinforced concrete elements (Vecchio & Collins, 1993).

In this study, the so-called "Model B" by Vecchio & Collins (1993), which considers only a reduction in the peak compressive stress, is used into the constitutive panel model formulation, due to its simplicity in the implementation and, as observed by Vecchio & Collins (1993), the use of more sophisticated models that also include the reduction in the strain at peak stress does not significantly improve the prediction of the compression softening effect. The softening coefficient β_m for the reduction of the compressive stress along the principal compressive direction is defined by,

$$\beta_m = \frac{1}{1 + 0.27 \cdot \left(\frac{\varepsilon_1}{\varepsilon_0} - 0.37\right)} \tag{3.47}$$

where ε_1 is the tensile strain in the principal tensile stress direction and ε_0 is the strain corresponding to peak stress of concrete in compression.

3.8.4. Tension stiffening effect on concrete and steel

In an RC member, the concrete between cracks, which still bonded to the reinforcing steel bars, contributes to the tensile resistance of the member; therefore, the stress and strain distribution of concrete and steel are not constant along element length as illustrated in Figure 3.13. The phenomenon described above is known as the tension stiffening effect. As proven by many researchers (e.g., Stevens, 1987; Belarbi & Hsu, 1994; Pang & Hsu, 1995; M. Y. Mansour, Hsu, & Lee, 2002; Bentz, 2005), the tension stiffening effect has a significant role in the post-cracking stiffness, yield capacity and shear behavior of reinforced concrete members. In this study, the model proposed by Belarbi & Hsu (1994) to represent the tension stiffening effect is used, which considers an average (smeared) tensile stress-strain behavior for cracked concrete, and an average stress-strain curve for steel bars stiffened by concrete between cracks. The tensile stress-strain behavior of concrete is described using a linear elastic relationship up to cracking $(f_{cr}, \varepsilon_{cr})$, and a descending branch for the post-cracked stress-strain. The complete average tensile stress-strain behavior $(\sigma_c, \varepsilon_c)$ for concrete is described by,

$$\sigma_c = \begin{cases} E_c \cdot \varepsilon_c & \varepsilon_c \leq \varepsilon_{cr} \\ f_{cr} \cdot (\varepsilon_{cr}/\varepsilon_c)^{0.4} & \varepsilon_c > \varepsilon_{cr} \end{cases} \tag{3.48}$$

where $E_c = 3875\sqrt{f'_c\ (\text{MPa})}$, $f_{cr} = 0.31\sqrt{f'_c\ (\text{MPa})}$ and $\varepsilon_{cr} = 0.00008$.

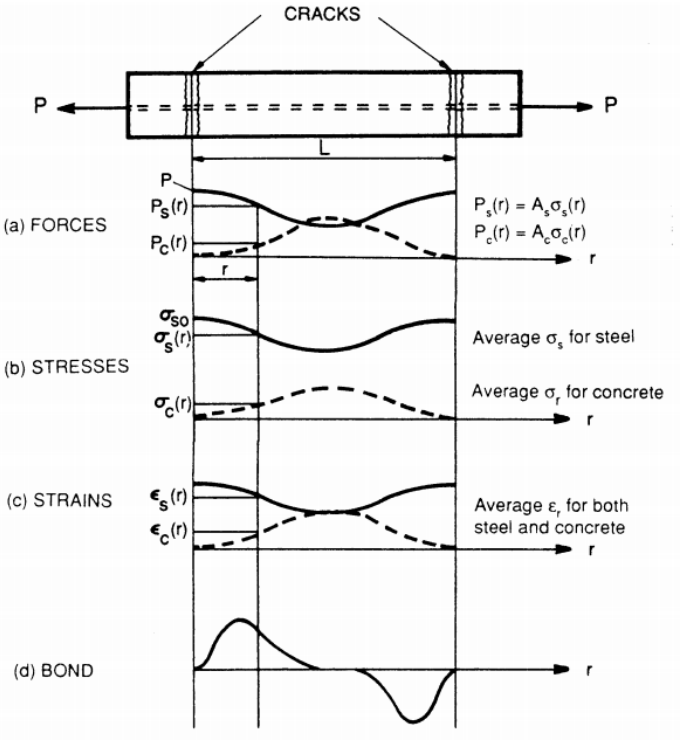

Figure 3.13: Schematic distribution of forces, strains, normal stress, and bond stress along a cracked reinforced concrete member (Belarbi & Hsu, 1994).

3.8.5. Biaxial damage on concrete

The constitutive RC panel element incorporates a damage coefficient to represent the cyclic damage on concrete, using the model proposed by Mansour & Hsu (2005). The model considers the use of a damage coefficient for cyclic analysis (does not apply for monotonic loading) and is applied as a multiplier to the compressive stress based on the cyclic strain history of concrete. Accordingly to the model, the damage coefficient (β_{damage}) is computed as a function of the ratio between the maximum value of the compressive strain experienced in the direction perpendicular to the compressive strut direction considered ($\varepsilon_{\perp max}$), to the peak compressive strain (ε'_c), and is given by Equation 3.49.

$$\beta_{damage} = \left(1 - 0.4 \cdot \frac{\varepsilon_{\perp max}}{\varepsilon'_c}\right) \tag{3.49}$$

Chapter 4

Analytical Model Validation

This chapter presents an extensive validation of the E-SFI model against experimental data of RC wall specimen tests. A description of the selected specimens and calibration of material models, along with calibration of the shear resisting parameters and mesh size, are presented in this chapter. Furthermore, a large database of 252 RC wall specimen tests reported in the literature is used to assess the capabilities of the model to predict the shear strength and its dependence to wall parameters. Also, analytical model predictions are compared with experimental results at both global and local levels for ten RC wall specimens. These comparisons are used to evaluate the performance of the model to predict the hysteretic response for various wall characteristics. Finally, the efficiency of the E-SFI model is analyzed against the MVLEM and SFI-MVLEM models in terms of elapsed time and current tangent convergence ratio.

4.1. Description of the selected RC wall specimen tests

Ten RC wall specimen tests with rectangular cross-section, tested under constant axial load and reversed-cyclic lateral loading conditions, were selected for the experimental validation of the E-SFI model, including a slender wall specimen (RW2) tested by Thomsen & Wallace (2004), four medium-rise specimens (RW-A20-P10-S38; RW-A20-P10-S63; RW-A15-P10-S51; RW-A15-P10-S78) tested by Tran & Wallace (2012), three squat walls specimens (SW-T2-S3-4; SW-T4-S1-6; SW-T6-S1-8) tested by Terzioglu et al. (2018), and two squat walls specimens (WP-T5-N0-S1; WP-T5-N5-S1) tested by Massone et al. (2009). All wall specimens were tested under single curvature condition, except for both specimens tested by Massone et al. (2009), which were tested under double curvature condition. The specimens cover a wide range of wall properties, such as the horizontal web reinforcement ratio ($\rho_{h,web}$) ranging from 0.27 to 0.73%; the vertical web reinforcement ratio ($\rho_{v,web}$) ranging from 0.23 to 0.73%; the longitudinal boundary reinforcement ratio (ρ_b) ranging from 1.33 to 9.75%; the shear span-to-depth ratio (M/Vl_w) ranging from 0.44 to 3.0; and the axial load level ($P/A_g f'_c$) ranging from 0 to 10%. For walls tested under single curvature condition, the wall height (h_w) is measured from the top of the pedestal to the point where the load was applied, whereas for walls under double curvature condition, the wall height corresponds to the length of clear span measured face-to-face of pedestals. The length (l_w) and thickness (t_w) are obtained from the gross section of the walls. The main properties of the selected RC wall specimens are summarized in Table 4.1.

Table 4.1: Main properties of RC wall specimens

Specimen ID	h_w (mm)	l_w (mm)	t_w (mm)	$\rho_{h,web}$ (%)	$\rho_{v,web}$ (%)	ρ_{bound} (%)	$\frac{M}{Vl_w}$	$\frac{P}{A_g f'_c}$	$\frac{V_{max}}{A_{cw}\sqrt{f'_c}}$	$\frac{V_{max}}{V_n}$	Failure Mode[1]
RW2	3660	1220	102	0.33	0.33	2.93	3.00	0.09	0.20	0.52	CB
RW-A20-P10-S38	2440	1220	152	0.27	0.27	3.23	2.00	0.10	0.36	0.98	CB/DT
RW-A20-P10-S63	2440	1220	152	0.61	0.61	7.11	2.00	0.10	0.56	1.02	CB/LI
RW-A15-P10-S51	1830	1220	152	0.32	0.32	3.23	1.50	0.10	0.46	0.93	CB/DT
RW-A15-P10-S78	1830	1220	152	0.73	0.73	6.06	1.50	0.10	0.61	0.89	DC/SS/LI
SW-T2-S3-4	950	1500	120	0.68	0.68	5.15	0.63	0.00	0.84	1.01	DC
SW-T4-S1-6	700	1500	120	0.68	0.68	3.95	0.47	0.00	0.82	0.99	DC
SW-T6-S1-8	1720	1500	120	0.68	0.68	9.75	1.15	0.00	0.86	1.03	DC
WP-T5-N0-S1	1220	1370	152	0.28	0.23	1.33	0.44	0.00	0.36	0.65	DT
WP-T5-N5-S1	1220	1370	152	0.28	0.23	1.33	0.44	0.05	0.55	1.02	DT

[1] CB: concrete crushing/bar buckling; LI: lateral instability; DT: diagonal tension; DC: diagonal compression; SS: shear sliding. (According to the authors).

4.1.1. Specimen tested by Thomsen and Wallace (2004)

The specimen RW2 was an approximately quarter-scale RC wall tested by Thomsen & Wallace (2004) with a rectangular cross-section, 3660 mm tall, 1220 mm length, and 102 mm thick, tested in an upright position under single curvature condition with an applied axial load at the wall top of approximately $0.07 f'_c A_g$. The specimen was part of an experimental program to verify the proposed displacement-based design approach by Wallace (1994, 1995), providing well-detailed boundary elements at the edges of the wall over the bottom 1.22 m. The shear capacity was provided accordingly to the requirements of the ACI 318-89 Equation 21-6 to resist the shear that develops for the probable wall moment. The vertical reinforcement was anchored within the pedestal at the base of the wall with sufficient development length as well as 90-degrees hooks. Figure 4.1 shows the cross-section with the reinforcing steel configuration.

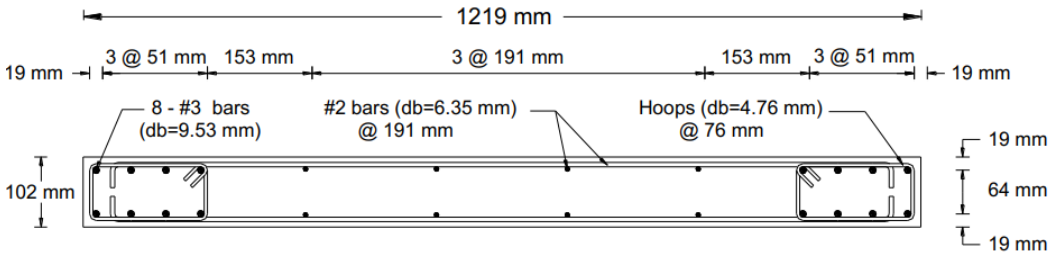

Figure 4.1: Cross-sectional view of specimen RW2 (Orakcal et al., 2004).

As shown in Figure 4.2(a), the specimen RW2 was heavily instrumented to measure displacements, loads, and strains at critical locations. The cyclic lateral displacement was applied to the wall using a hydraulic actuator mounted horizontally to a reaction wall, reaching drift levels of approximately 0.1%, 0.25%, 0.5%, 0.75%, 1.0%, 1.5%, 2.0%, and 2.5%. The

failure mode of the wall was governed by concrete crushing and buckling of the longitudinal boundary reinforcement, as observed in Figure 4.2(b).

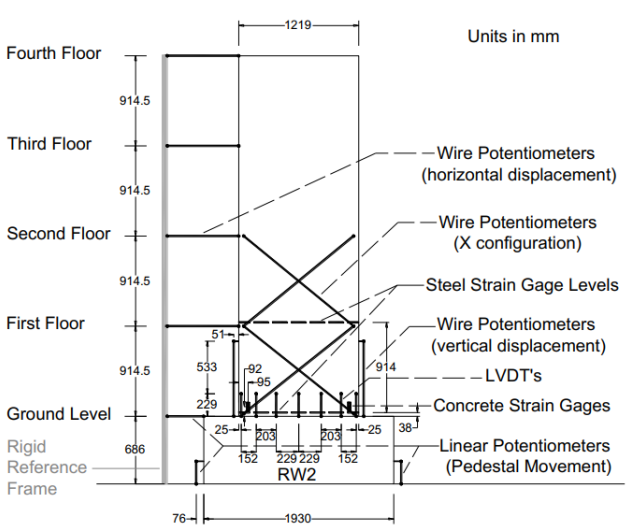

(a) Instrumentation (Orakcal et al., 2004).

(b) Failure mode (Thomsen & Wallace, 2004).

Figure 4.2: Instrumentation and failure mode of specimen RW2 specimen.

4.1.2. Specimens tested by Massone et al. (2009)

An experimental program carried out at UCLA Structural/Earthquake Engineering Research Laboratory (SEERL) was developed by Massone et al. (2009) to provide experimental data of low-rise structural RC walls. The program included five different three-quarter scale walls (two spandrels and three piers) to represent walls constructed in California between approximately 1940 and 1970. An identical specimen was constructed for each wall configuration, resulting in ten RC wall specimens. The wall spandrels were 1520mm tall, 1520mm length, and 152mm thickness, whereas de wall piers were 1220 mm tall, 1370 mm length, and 152 mm thick. The specimens were instrumented with DC-LVDTs (DC-excited linear variable differential transducers) over the height to provide measurement of deformations and rotations. The walls were tested in an upright position under double curvature condition (zero-rotation at wall top end), and were subjected to displacement-controlled cycles with target drift levels of 0.2%, 0.3%, 0.4%, 0.6%, 0.8%, 1.2%, 1.6%, 2.0%, 2.4%, and 3.2%; however, in some specimens, the cyclic protocol was modified.

Two wall piers of this program were selected for validation of the shear-flexure interaction model, including the specimens WP-T5-N0-S1 and WP-T5-N5-S1, which differentiate in the axial load level (0 and 5%, respectively). As shown in Figure 4.3, the distributed vertical reinforcement of the piers was #4@330mm, the distributed horizontal reinforcement was #4@305mm, and the longitudinal boundary reinforcement was 2#4 bars. It must be noted that the self-weight of the steel reaction frame that generates the zero-rotation at wall top end provides an extra vertical load of 53 kN.

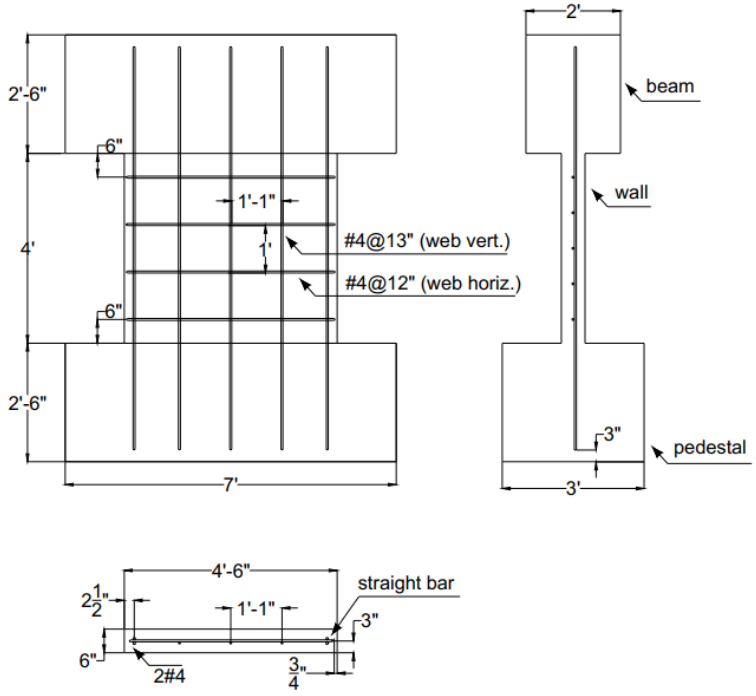

Figure 4.3: Layout of pier specimens tested by Massone et al. (2006).

The specimen WP-T5-N0-S1 reached its lateral load capacity at 0.8% drift due to the high wideness of the principal diagonal crack. For the following drift cycles, as the crack widths widened, sliding along the primary diagonal crack and lateral strength degradation were observed, as well as concrete crushing at mid-height, indicating a diagonal tension failure. Figure 4.4 shows the wall specimen at different drift levels.

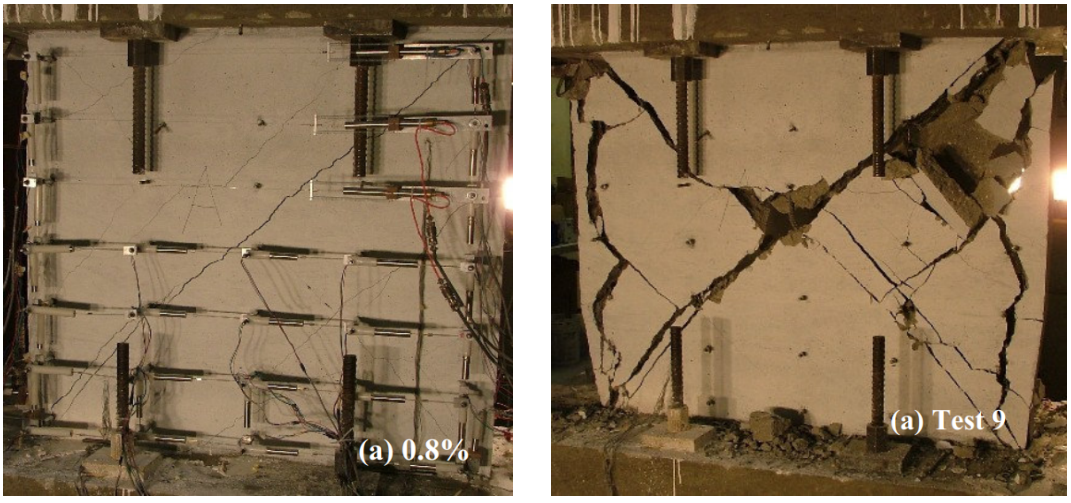

(a) 0.8% drift (b) 3.2% drift

Figure 4.4: Observed damage for specimen WP-T5-N0-S1 (Massone, 2006).

The specimen WP-T5-N5-S1 reached its lateral load capacity at 0.8% drift due to a combination of concrete crushing at mid-height at the center of the wall and widening of the

primary diagonal cracks. For the following drift cycles, as the crack widths widened, sliding along the primary diagonal crack and lateral strength degradation were observed, as well as concrete crushing, indicating a diagonal tension type of failure. Figure 4.5 shows the wall specimen at different drift levels.

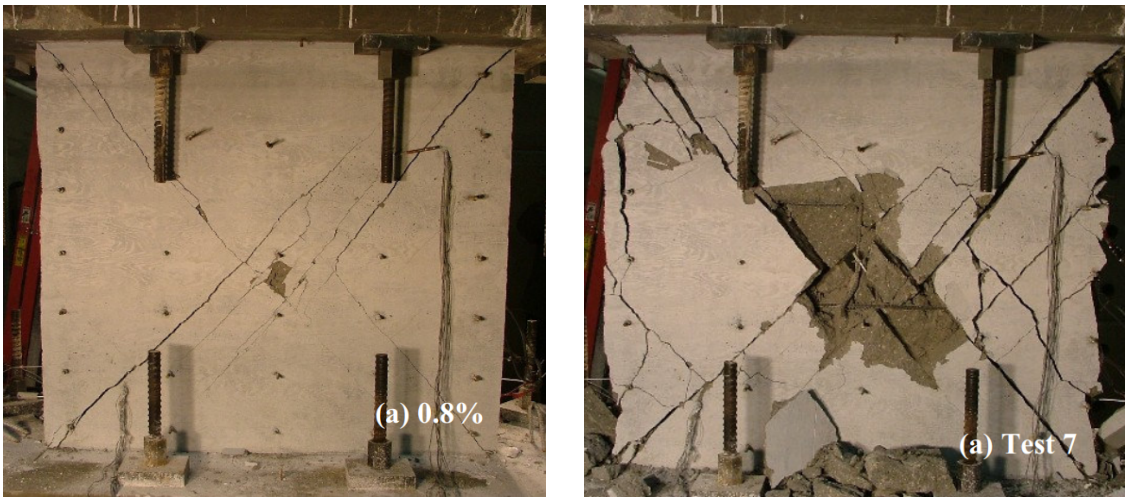

(a) 0.8% drift (b) 3.2% drift

Figure 4.5: Observed damage for specimen WP-T5-N5-S1 (Massone, 2006).

4.1.3. Specimens tested by Tran and Wallace (2012)

An experimental program carried out at the University of California Los Angeles (UCLA) was developed by Tran & Wallace (2012) to study the nonlinear cyclic response of moderate aspect ratio RC structural walls. The program included five large-scale cantilever structural wall specimens of 2440 mm or 1830 mm tall, 1220 mm length, and 152 mm thick, tested in an upright position under constant axial load. The specimens were designed according to the ACI 318-11 code to yield in flexure before loss of lateral load capacity; however, an important contribution of nonlinear shear deformation was observed. Four of the five specimens were selected to study the shear-flexure interaction model, including the specimens RW-A20-P10-S38; RW-A20-P10-S63; RW-A15-P10-S51; and RW-A15-P10-S78, representing a large variety of medium-rise walls configurations. A typical wall cross-section is shown in Figure 4.6, whereas a typical detailing of the special boundary element (with alternated crosstie over the height) is presented in Figure 4.7. Wall reinforcement details are presented in Table 4.2.

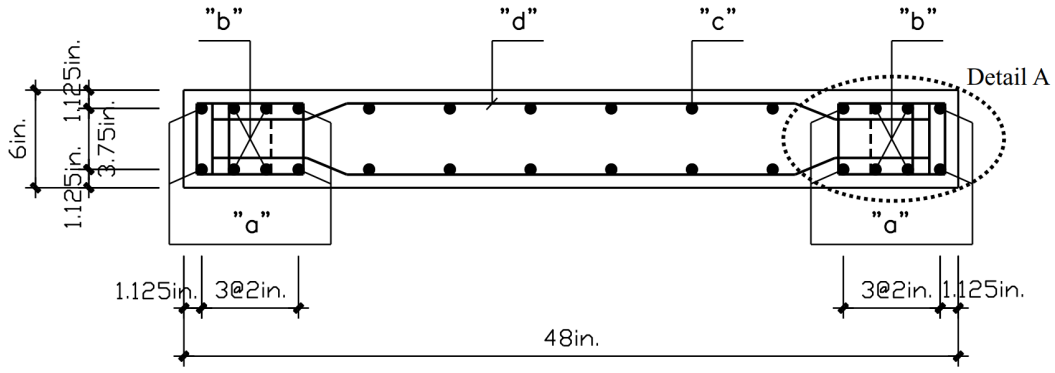

Figure 4.6: Typical wall cross-section (Tran, 2012).

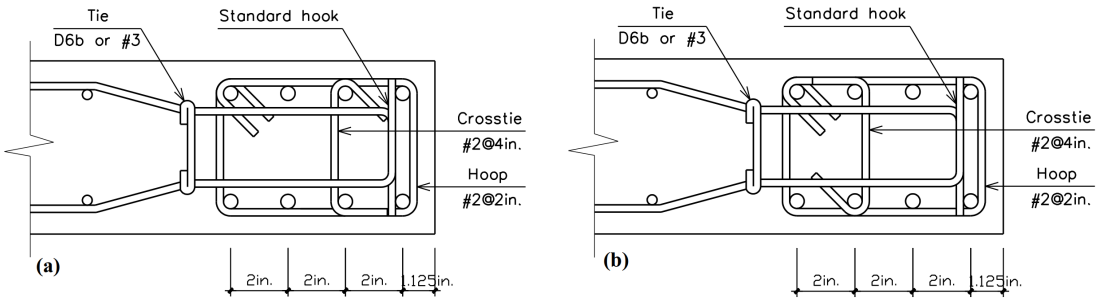

(a) (b)

Figure 4.7: Typical wall boundary detailing, Detail A (Tran, 2012).

Table 4.2: Wall reinforcement details.

Specimen ID	"a"	"b"	"c"	"d"
RW-A20-P10-S38	4#4	4#4	6D6a @ 140 mm	D6b @ 140 mm
RW-A20-P10-S63	4#6	4#6	5#3 @ 152 mm	#3 @ 140 mm
RW-A15-P10-S51	4#4	4#4	7D6a @ 114 mm	D6b @ 114 mm
RW-A15-P10-S78	4#6	4#5	6#3 @ 127 mm	#3 @ 127 mm

The specimens were heavily instrumented with Linear Variable Differential Transformers (LVDTs) to measure wall foundation sliding and uplift, lateral wall displacement at various height levels (including flexural, shear, and sliding shear components), and average concrete strains over specified gauge lengths. Reinforcement strains were measured using strain gauges affixed to the longitudinal boundary and transverse reinforcement, and the web vertical and horizontal reinforcement, over a height of about $l_w/2$ from the wall-foundation block interface (length of expected plastic hinge region). The walls were subjected to displacement-controlled cycles using a horizontal hydraulic actuator, applying the force at either 1830 mm or 2440 mm above the wall-foundation block interface. Displacement-controlled cycles were typically performed at drift ratios of 0.5%, 0.75%, 1.0%, 1.5%, 2.0%, 3.0%, and 4.0%.

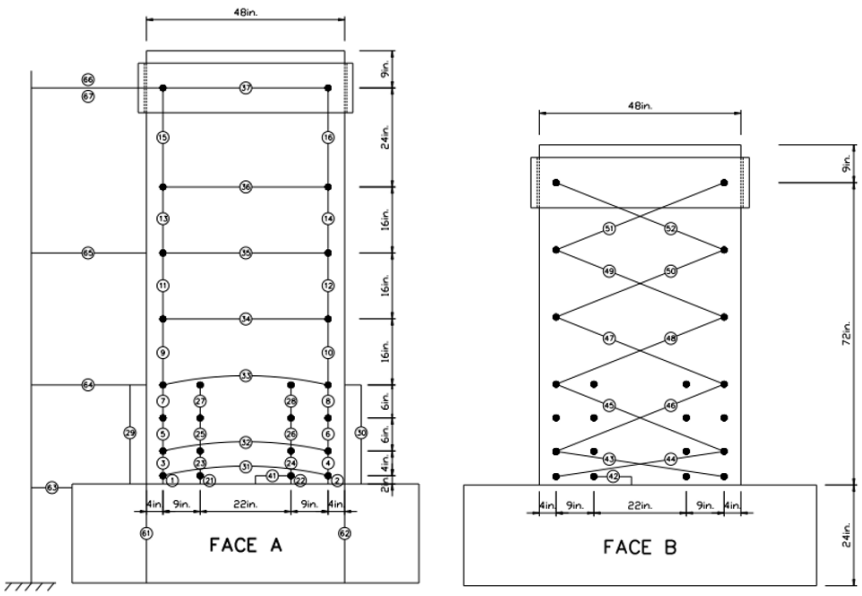

(a) Face A, aspect ratio 2.0 (b) Face B, aspect ratio 1.5

Figure 4.8: LVDTs layout of wall specimens (Tran, 2012).

The specimen RW-A20-P10-S38 failed during the second positive cycle of 3.1% drift due to concrete crushing and buckling of the longitudinal boundary reinforcement at the right (south) wall boundary. Immediately, a sudden diagonal tension failure occurred, with fracture of the horizontal web bars along a diagonal crack. Figure 4.9 shows the crack pattern developed over the entire wall at different drift levels, whereas Figure 4.10 shows the wall boundaries at the end of the test.

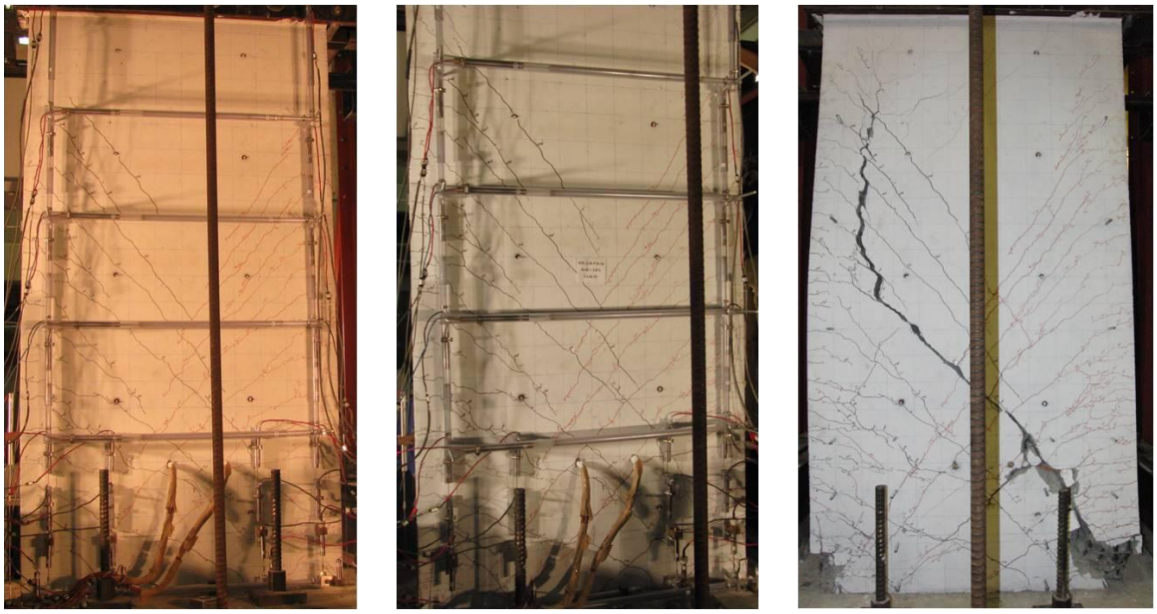

(a) Drift: 0.56% (b) Drift: 1.5% (c) End of test

Figure 4.9: Cracking pattern of specimen RW-A20-P10-S38 (Tran, 2012).

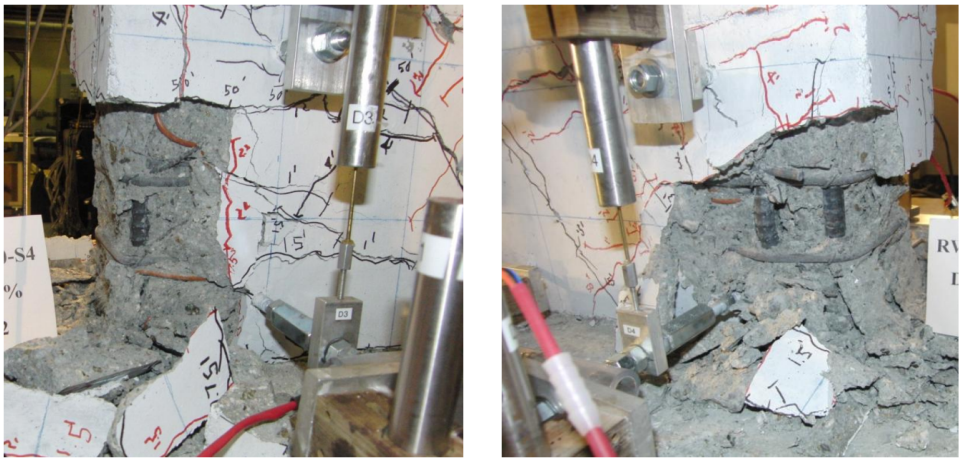

(a) North boundary (b) South boundary

Figure 4.10: Boundaries at end of test of specimen RW-A20-P10-S38 (Tran, 2012).

The specimen RW-A20-P10-S63 failed during the second negative cycle of 3.0% drift due to concrete crushing and buckling of the longitudinal boundary and some vertical web reinforcement at the north (left) wall boundary. Also, lateral instability (out-of-plane buckling) of the boundary zone was observed. A similar failure mode occurred when the loading was reversed. Figure 4.11 shows the crack pattern developed over the entire wall at different drift levels, whereas Figure 4.12 shows the wall boundaries at the end of the test.

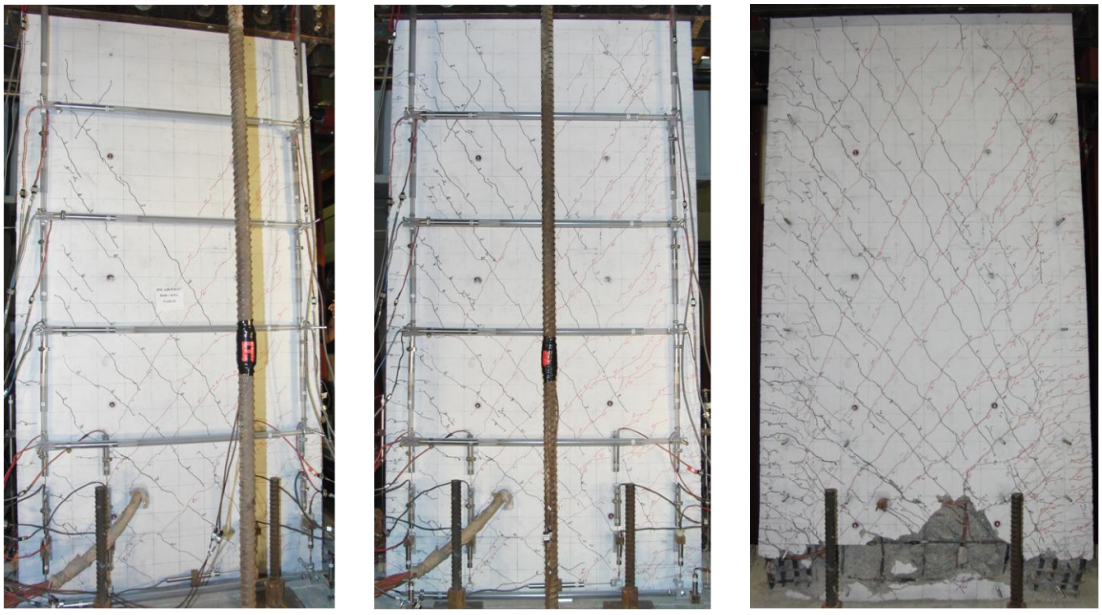

(a) Drift: 0.5% (b) Drift: 1.5% (c) End of test

Figure 4.11: Cracking pattern of specimen RW-A20-P10-S63 (Tran, 2012).

(a) North boundary (b) South boundary

Figure 4.12: Boundaries at end of test of specimen RW-A20-P10-S63 (Tran, 2012).

The specimen RW-A15-P10-S51 failed during the first positive cycle of 4.0% drift due to concrete crushing and buckling of the vertical boundary reinforcement at the south wall boundary, which initiated diagonal tension failure along a mayor crack with fracture of several horizontal web bars. When the loading was reversed, concrete crushing and buckling of the vertical boundary reinforcement at north wall boundary was observed, along with fracture of two longitudinal bars of the south wall boundary. Figure 4.13 shows the crack pattern developed over the entire wall at different drift levels (indicating with a * the crack were diagonal tension failure occurred), whereas Figure 4.14 shows the wall boundaries at the end of the test.

(a) Drift: 0.5% (b) Drift: 1.5% (c) End of test

Figure 4.13: Cracking pattern of specimen RW-A15-P10-S51 (Tran, 2012).

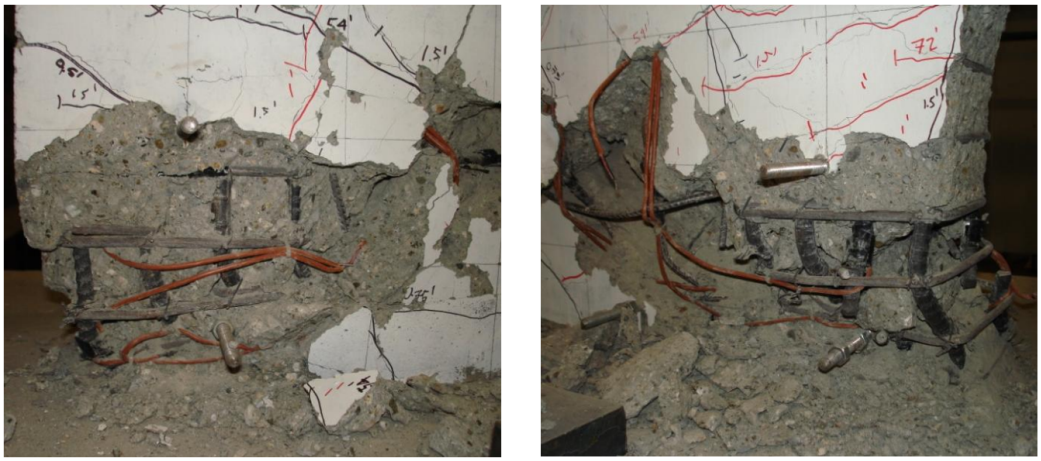

(a) North boundary (b) South boundary

Figure 4.14: Boundaries at end of test of specimen RW-A15-P10-S51 (Tran, 2012).

The specimen RW-A15-P10-S78 initiated its degradation during the first cycle of 3.0% drift due to concrete spalling along diagonal compressive struts near the wall-foundation block interface at the wall boundaries. As a result, the wall lost about 9% of its peak lateral load in both directions. The wall failed during the second positive cycle of 3.0% drift due to shear sliding, followed by out-of-plane buckling at south wall boundary. When the loading was reversed, out-of-plane buckling at north wall boundary was observed. Figure 4.15 shows the crack pattern developed over the entire wall at different drift levels, whereas Figure 4.16 shows the wall boundaries at the end of the test.

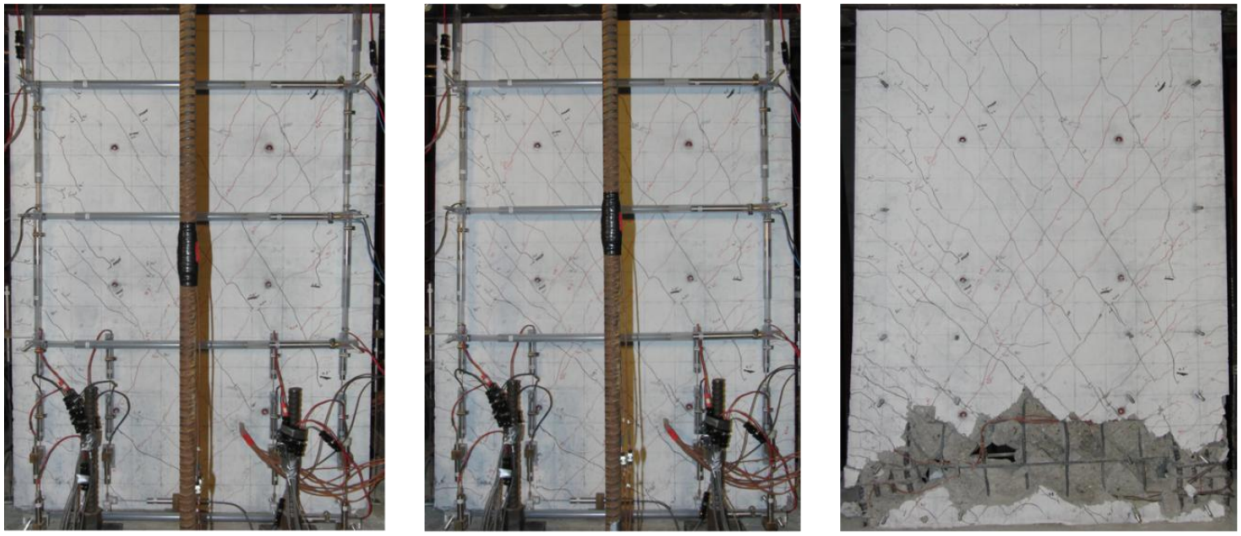

(a) Drift: 0.5% (b) Drift: 1.5% (c) End of test

Figure 4.15: Cracking pattern of specimen RW-A15-P10-S78 (Tran, 2012).

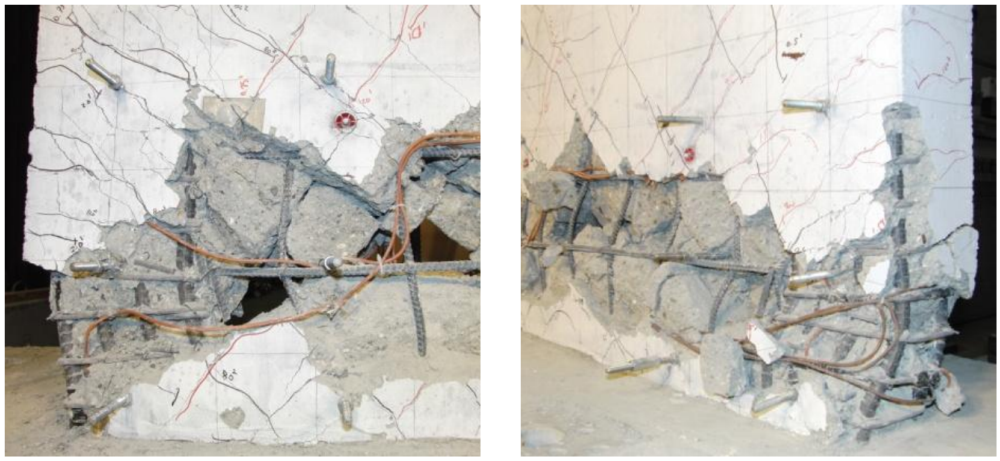

(a) North boundary (b) South boundary

Figure 4.16: Boundaries at end of test of specimen RW-A15-P10-S78 (Tran, 2012).

4.1.4. Specimens tested by Terzioglu et al. (2018)

An experimental program carried out at Bogazici University Structural Engineering Laboratory was developed by Terzioglu et al. (2018) to study the behavior of shear-controlled RC walls designed to resist seismic actions and to provide experimental data for the development of analytical modeling methodologies. The program included eleven squat wall specimens of 1500 mm length and 120 mm thickness, with varying heights to attain different aspect ratios. The specimens were instrumented with several LVDTs to measure displacements and rotations over the height, and sliding shear deformations at the wall-pedestal interface. Additionally, strain gauges were mounted on the reinforcing bars to monitoring yielding in specific rebars. The walls were tested in an upright position under cantilever configuration, and were subjected to displacement-controlled cycles with target drift levels of 0.05%, 0.1%, 0.15%, 0.2%, 0.3%, 0.4%, 0.6%, 0.8%, 1.0%, 1.2%, 1.4%, 1.6%, 1.8%, 2.0%, 2.4%, and 3.2%, however, in some cases additional drift levels were imposed.

Three of the eleven wall specimens were selected to study the shear-flexure interaction model, including the specimens SW-T2-S3-4; SW-T4-S1-6; and SW-T6-S1-8, representing a large variety of wall aspect ratios for shear-controlled walls under single curvature condition. The geometry and reinforcement of the selected wall specimens are shown from Figure 4.17 to 4.19.

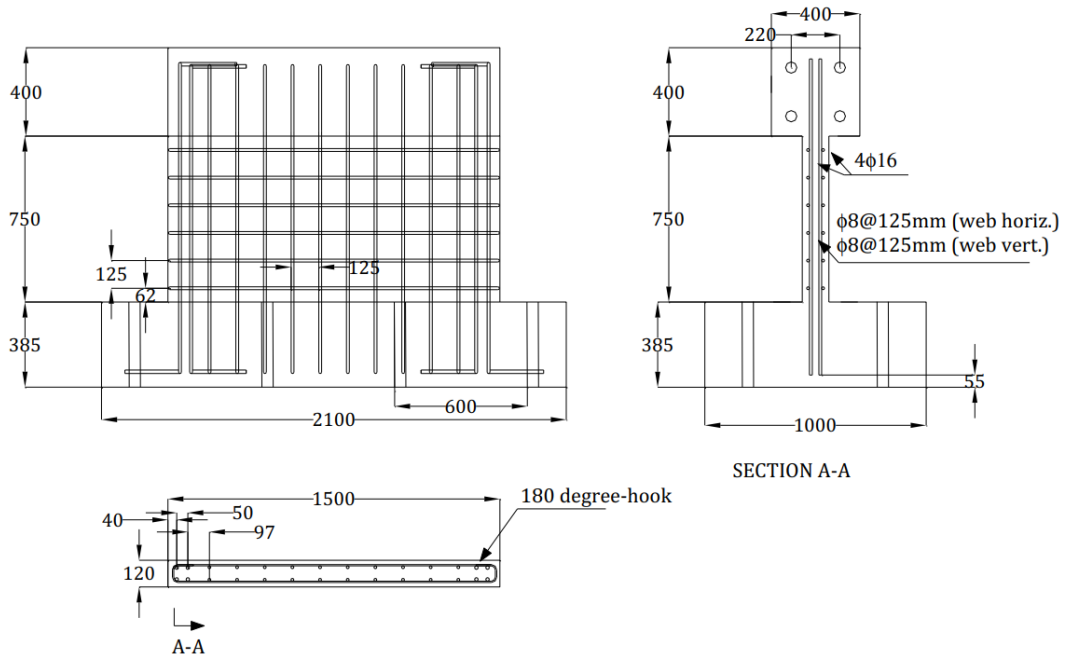

Figure 4.17: Layout of specimen SW-T2-S3-4 (Terzioglu, 2011).

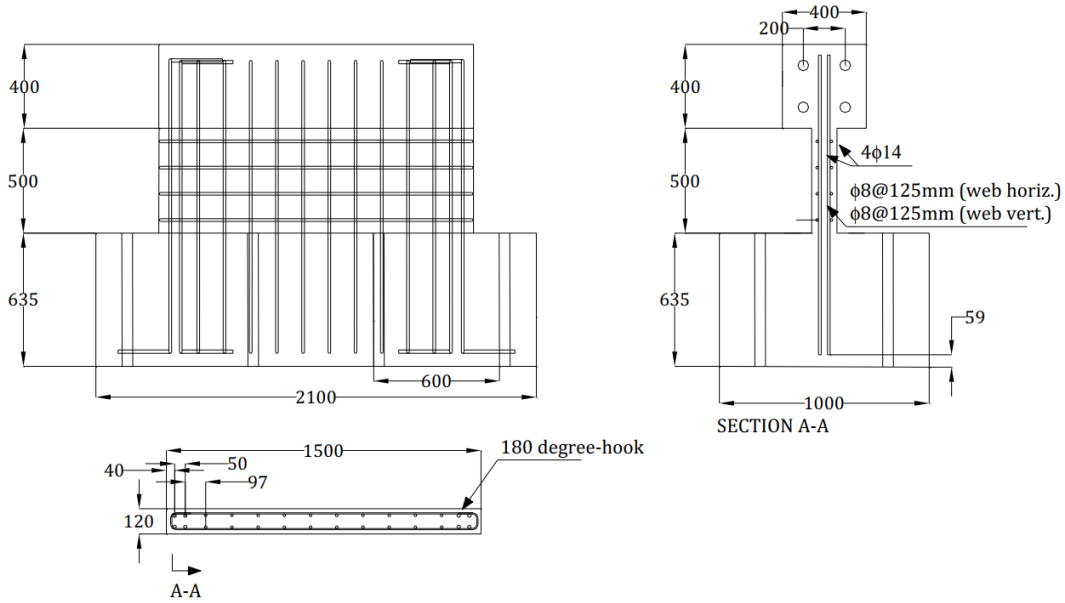

Figure 4.18: Layout of specimen SW-T4-S1-6 (Terzioglu, 2011).

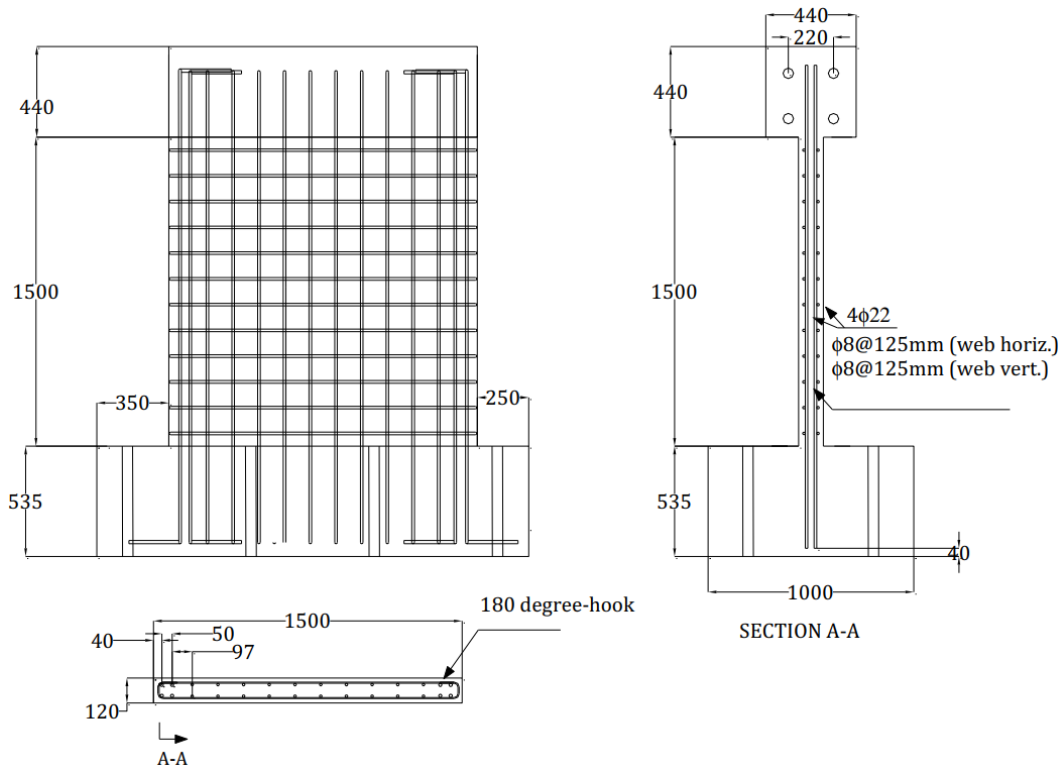

Figure 4.19: Layout of specimen SW-T6-S1-8 (Terzioglu, 2011).

The specimen SW-T2-S3-4 reached its lateral load capacity at 0.6% drift ratio; however, strength degradation started at negative cycle of 1% drift due to crushing of concrete at the bottom left corner. Crushing of concrete propagated along the width of the wall bottom for the subsequent cycles, indicating a diagonal compression failure mode. Figure 4.20 shows the wall specimen under different levels of damage.

(a) Medium damage level

(b) High damage level

Figure 4.20: Damage levels for specimen SW-T2-S3-4 (Terzioglu, 2011).

The specimen SW-T4-S1-6 reached its lateral load capacity at 0.6% drift; however, strength degradation started at 1% drift due to crushing of the concrete at the wall bottom corner and center. Crushing of concrete propagated along the width of the wall bottom for the subsequent cycles, indicating a diagonal compression failure mode. Figure 4.21 shows the wall specimen under different levels of damage.

(a) Medium damage level (b) High damage level

Figure 4.21: Damage levels for specimen SW-T4-S1-6 (Terzioglu, 2011).

The specimen SW-T6-S1-8 reached its lateral load capacity at 1.0% drift; however, strength degradation started at 1.2% drift due to crushing of concrete at the bottom corner of the wall. Crushing of the concrete propagated from the wall bottom corners toward the bottom center for the subsequent cycles, indicating a diagonal compression failure mode. Figure 4.22 shows the wall specimen under different levels of damage.

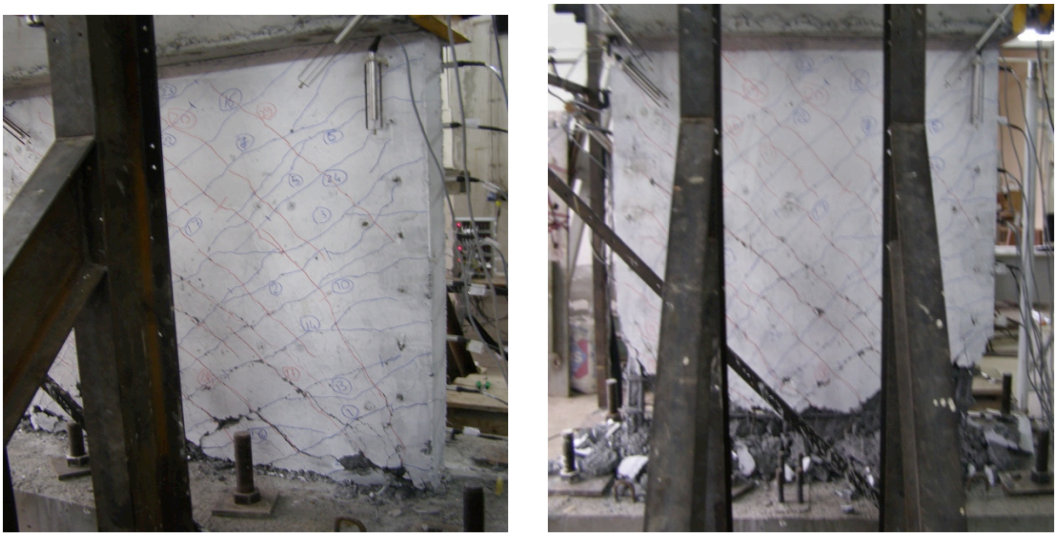

(a) Medium damage level (b) High damage level

Figure 4.22: Damage levels for specimen SW-T6-S1-8 (Terzioglu, 2011).

4.2. Calibration of material models

The concrete compressive strength (f'_c) and the strain at compressive strength (ε'_c) obtained from monotonic test results on standard cylinder specimens of concrete used in the construction of the walls and reported in the literature were used for the unconfined stress-strain model of concrete in compression. For the confined stress-strain model of concrete in compression, the confined concrete compressive strength (f'_{cc}) and the strain at confined compressive strength (ε'_{cc}) were obtained according to the model proposed by Mander et al. (1988). The elastic modulus (E_c) and the shape factor in compression (r_c), for both confined and unconfined concrete, were obtained according to the empirical equations proposed by Chang & Mander (1994). The post-peak slope of the model envelope for confined and unconfined concrete in compression was adjusted to agree with the model proposed by Saatcioglu & Razvi (1992). As suggested by Belarbi & Hsu (1994), the tensile strength for concrete was computed as $f_t = 0.31\sqrt{f'_c}$ (MPa) for a tensile strain equal to $\varepsilon_t = 0.00008$. The shape factor for concrete in tension was taken as $r_t = 1.2$, as proposed by Orakcal & Wallace (2006). For the reinforcing steel stress-strain model, the yield strength (f_y) and the strain hardening ratio (b) were adjusted to agree with the obtained properties of bare bars used in the construction of the walls and reported in the literature. For reinforcing steel in tension, the yield strength and the strain hardening ratio were modified to account for the tension stiffening effect, as proposed by Belarbi & Hsu (1994). The elastic modulus for reinforcing steel was taken as $E_0 = 200.000$ MPa, and the curvature parameters were calibrated as $R_0 = 20$, $a_1 = 18.5$, and $a_2 = 0.15$, as proposed by Menegotto & Pinto (1973); however, for specimen RW2 a value of $a_2 = 0.0015$ was used based on a prior work (Orakcal & Wallace, 2006). The main materials properties are summarized in Table 4.3.

Table 4.3: Materials properties of RC wall specimens

Specimen ID	f'_c (MPa) unconf./conf.	ε'_c unconf./conf.	f_t (MPa)	$f_{yh,web}$ (MPa)	$f_{yv,web}$ (MPa)	b_{web}	$f_{y,bound.}$ (MPa)	$b_{bound.}$
RW2	42.8/47.6	0.0021/0.0033	2.03	448	448	0.020	434	0.020
RW-A20-P10-S38	47.1/62.2	0.0023/0.0060	2.13	516	450	0.020	473	0.010
RW-A20-P10-S63	48.6/65.4	0.0020/0.0055	2.16	443	443	0.020	477	0.010
RW-A15-P10-S51	48.8/63.9	0.0022/0.0056	2.16	516	450	0.020	473	0.010
RW-A15-P10-S78	55.8/72.2	0.0024/0.0059	2.31	443	443	0.020	476	0.010
SW-T2-S3-4	29.0/– –	0.0020/– –	1.67	584	584	0.008	473	0.008
SW-T4-S1-6	34.8/– –	0.0021/– –	1.83	584	584	0.008	519	0.008
SW-T6-S1-8	22.6/– –	0.0019/– –	1.47	584	584	0.008	528	0.008
WP-T5-N0-S1	29.9/– –	0.0025/– –	1.70	424	424	0.008	424	0.008
WP-T5-N5-S1	31.9/– –	0.0023/– –	1.75	424	424	0.008	424	0.008

4.3. Sensitivity analysis to shear resisting parameters

A sensitivity analysis of model prediction to the shear aggregate interlock friction coefficient (η) and the dowel action coefficient (α) is performed to reveal their effects in the global response, as well as their effect on the shear contribution to the global deformation. The sensitivity analysis results are presented from Figure 4.23 to 4.27, considering only one cycle per drift level. The analysis reveals that increasing the shear friction coefficient (η) as well as the dowel action coefficient (α) leads to an increase in the shear strength of the wall, as well as a reduction of the shear contribution to the global response, suggesting an optimal value for the shear friction coefficient of $\eta = 0.35$ for all cases, whereas the dowel action coefficient must be taken as $\alpha = 0.005$ for medium-rise and slender walls ($M/Vl_W \geq 1.5$), and $\alpha = 0.0001$ for squat walls ($M/Vl_W < 1.5$). The reduction of the dowel action coefficient for squat walls is related to the fact of no dowel capacity degradation mechanism into the model formulation, and therefore the dowel action contribution needs to be re-calibrated for walls with a high shear demand.

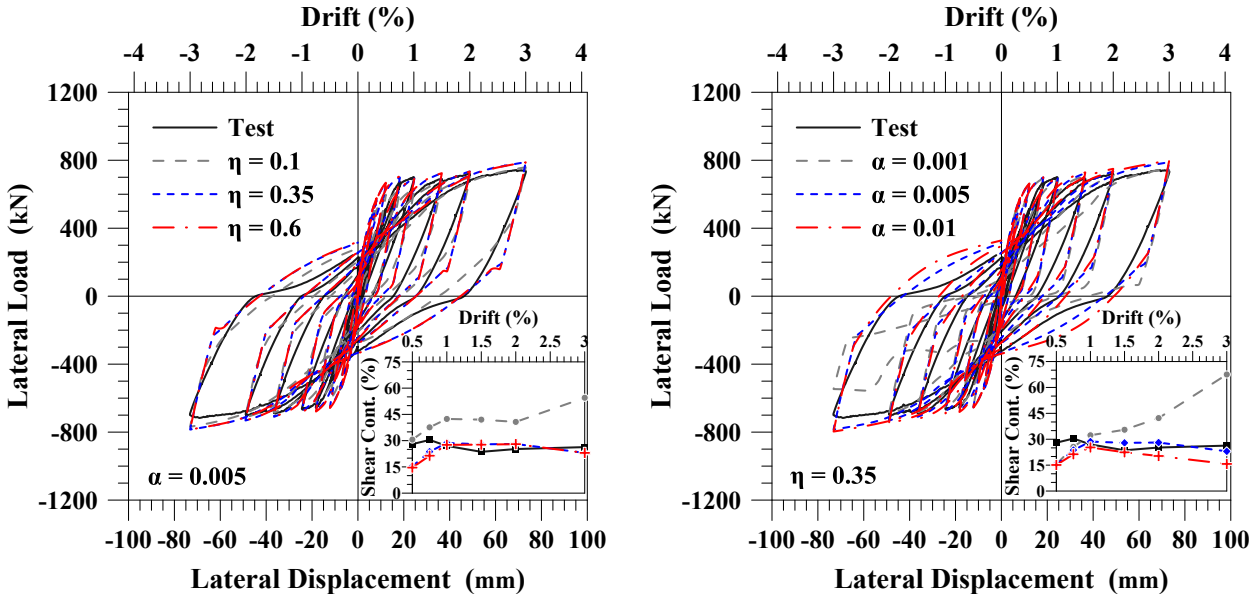

(a) Sensitivity to shear friction coefficient.

(b) Sensitivity to dowel action coefficient.

Figure 4.23: Sensitivity of model response to shear resisting mechanisms for specimen RW-A20-P10-S63.

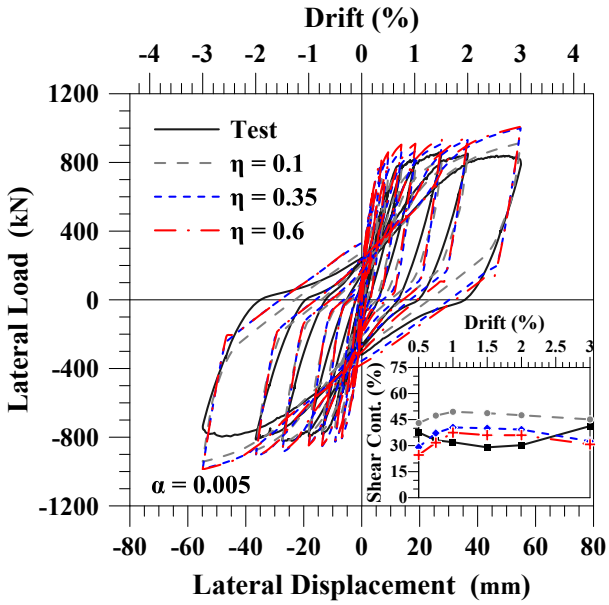

(a) Sensitivity to shear friction coefficient.

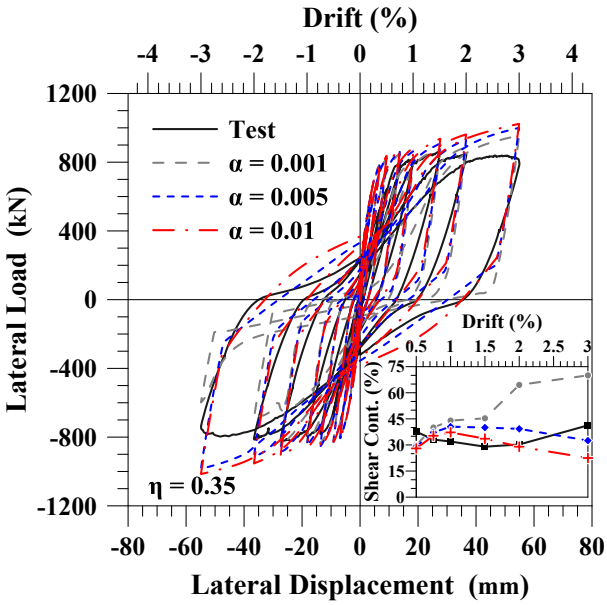

(b) Sensitivity to dowel action coefficient.

Figure 4.24: Sensitivity of model response to shear resisting mechanisms for specimen RW-A15-P10-S78.

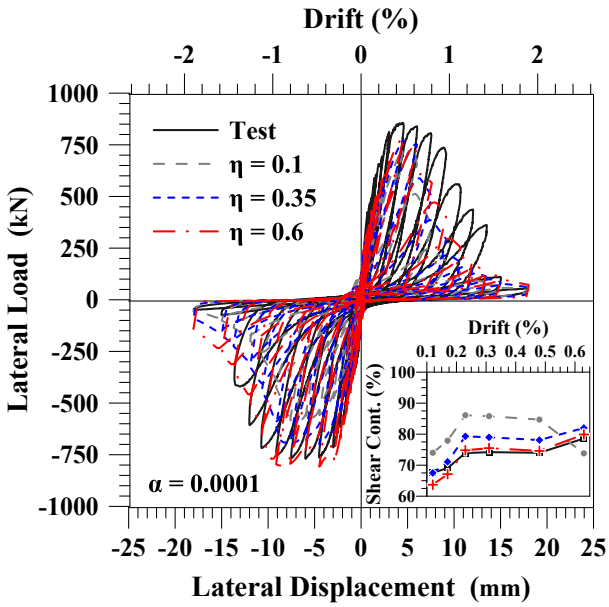

(a) Sensitivity to shear friction coefficient.

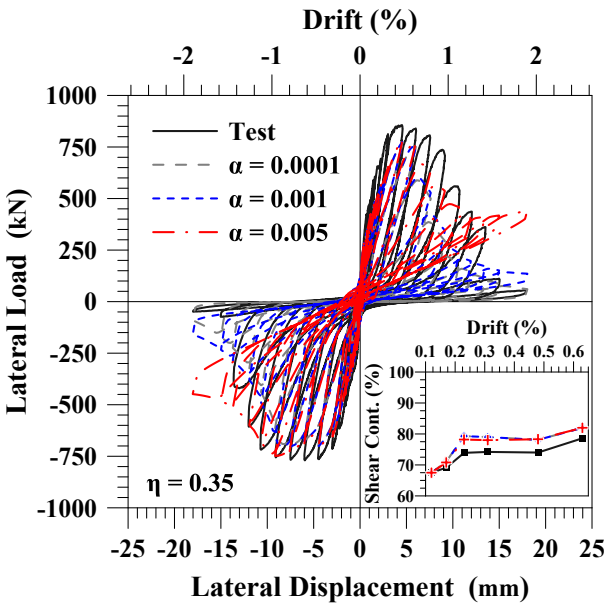

(b) Sensitivity to dowel action coefficient.

Figure 4.25: Sensitivity of model response to shear resisting mechanisms for specimen T2-S3-4.

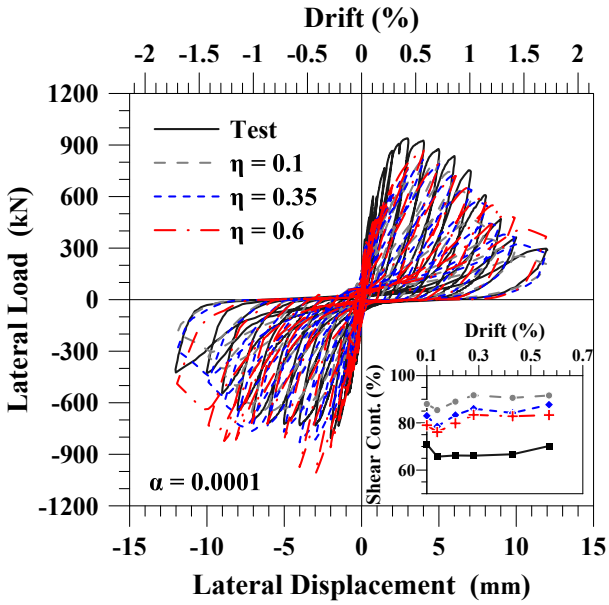

(a) Sensitivity to shear friction coefficient.

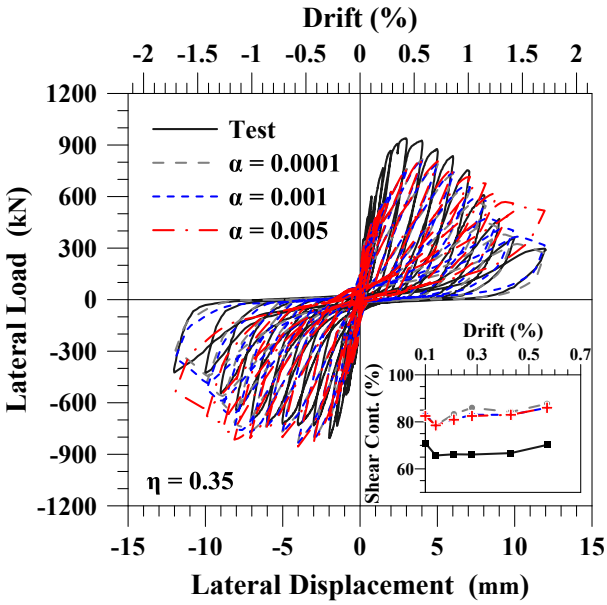

(b) Sensitivity to dowel action coefficient.

Figure 4.26: Sensitivity of model response to shear resisting mechanisms for specimen T4-S1-6.

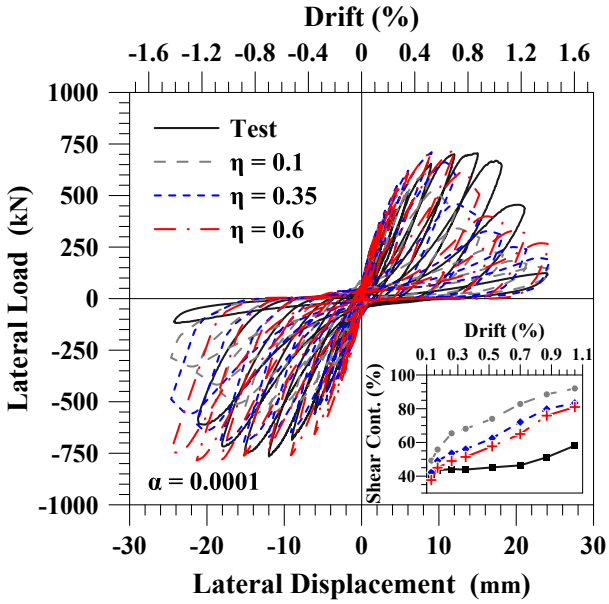

(a) Sensitivity to shear friction coefficient.

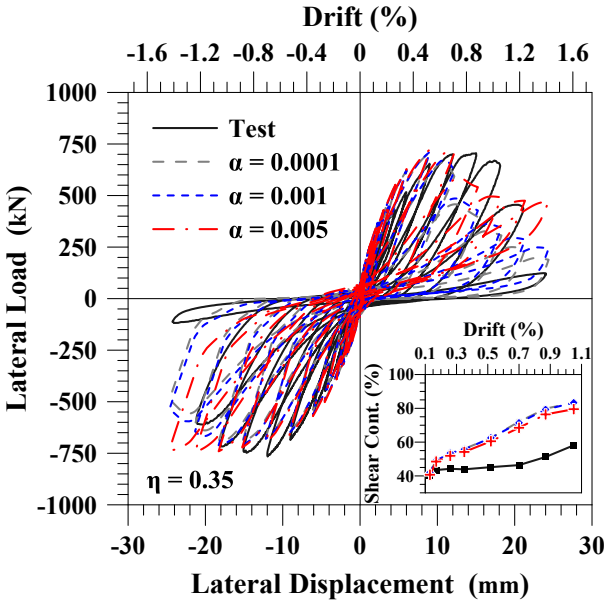

(b) Sensitivity to dowel action coefficient.

Figure 4.27: Sensitivity of model response to shear resisting mechanisms for specimen T6-S1-8.

4.4. Sensitivity analysis to mesh size

A wall model can be defined by a user-defined number of E-SFI elements stacked one upon the other (n), as well as a number of RC panel elements along an E-SFI element (m). To understand the effect of discretization in a wall model, a sensitivity analysis is performed for a squat wall specimen (SW-T2-S3-4) and a medium-rise wall specimen (RW-A20-P10-S63). Figure 4.28(a) and 4.29(a), shows the sensitivity analysis to the number of equal-size vertical E-SFI elements (n) for a constant number of $m = 6$ RC panel elements. The results reveal that global response is almost objective in the hardening zone and becomes non-objective in the softening zone; however, local response of the most-strained element is non-objective for the whole range of behavior. Also, it is observed that change the number of equal-size E-SFI elements over the height leads to differences in the peak resistance and deformation, as well as the degradation rate due to differences in the local response. This behavior is a common shortcoming in displacement-based elements, due to the formulation does not strictly satisfy the equilibrium into element interior, as opposed to a force-based formulation,; therefore, the element equilibrium is satisfied in an average sense. As described by Calabrese et al. 2010, a typical regularization technique for displacement-based elements with one integration point consist of adjusting the element size of the most strained element to the plastic hinge length (L_p) to have an appropriate integration of the inelastic response. With regularization of the most-strained (extremity) elements' height, the wall global and local responses are objective regardless of the number of elements over the height, as shown in Figure 4.28(b) and 4.29(b). The adopted regularization technique is depicted in Figure 4.30.

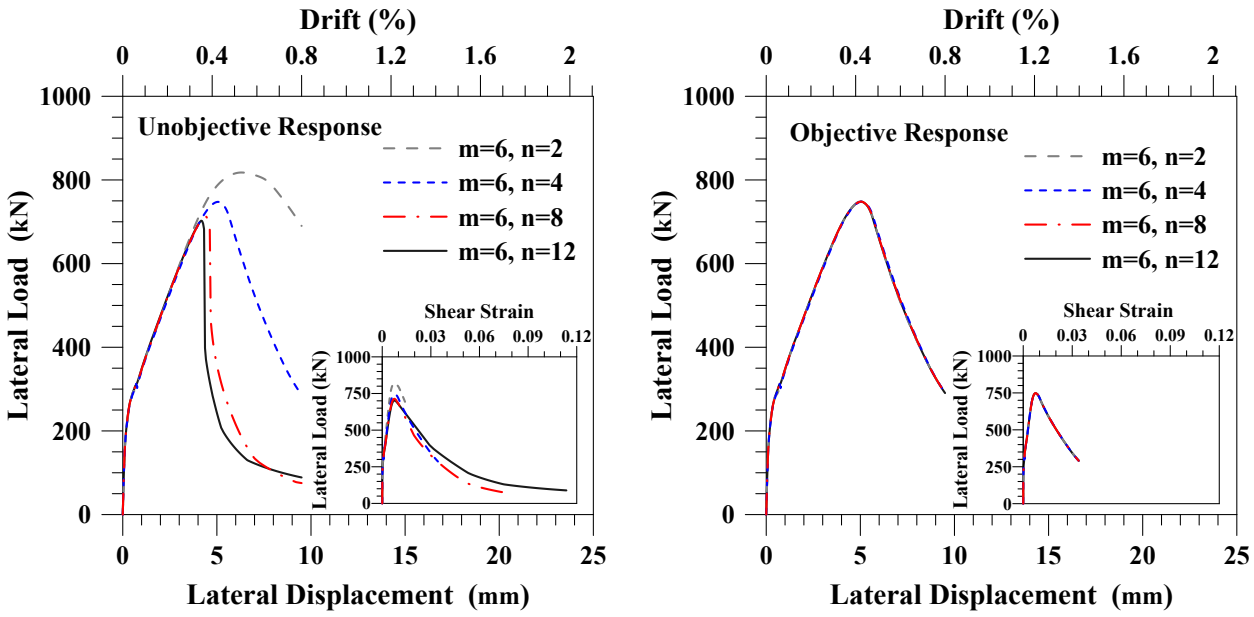

(a) Unregularized response.

(b) Regularized response by plastic hinge length.

Figure 4.28: Sensitivity analysis of the model to the number of vertical wall elements for specimen SW-T2-S3-4.

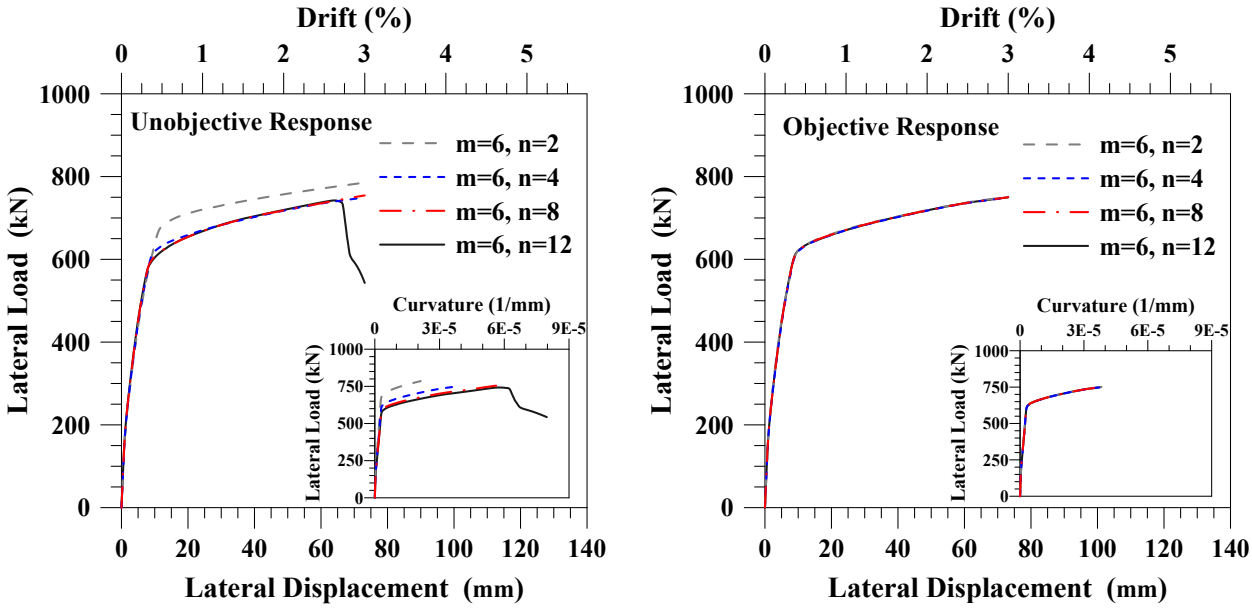

(a) Unregularized response.

(b) Regularized response by plastic hinge length.

Figure 4.29: Sensitivity analysis of the model to the number of vertical wall elements for specimen RW-A20-P10-S63.

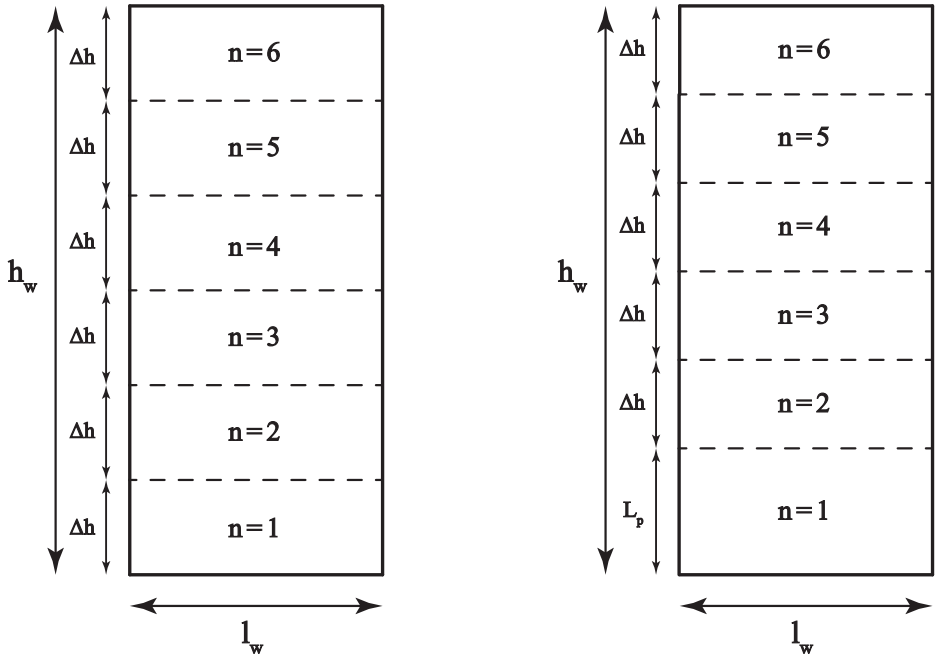

(a) Unregularized response.

(b) Regularized response.

Figure 4.30: Layout of wall model vertical discretization for n=6 E-SFI elements.

Figure 4.31 shows the effect of the number of RC panels along an E-SFI element (m) for a constant number of $n = 6$ E-SFI elements over the height. For the cases of $m = 4$ and $m = 6$ horizontal elements, one component was used for each boundary element, whereas for the case of $m = 12$ panels, two components per boundary were used, and the remaining

horizontal panels were equal-size distributed. The results indicate that the global response is almost insensitive to the number of horizontal elements above $m = 4$, although increase the number of RC panels leads to a more accurate distribution of strains over the wall length; however, computational effort increases.

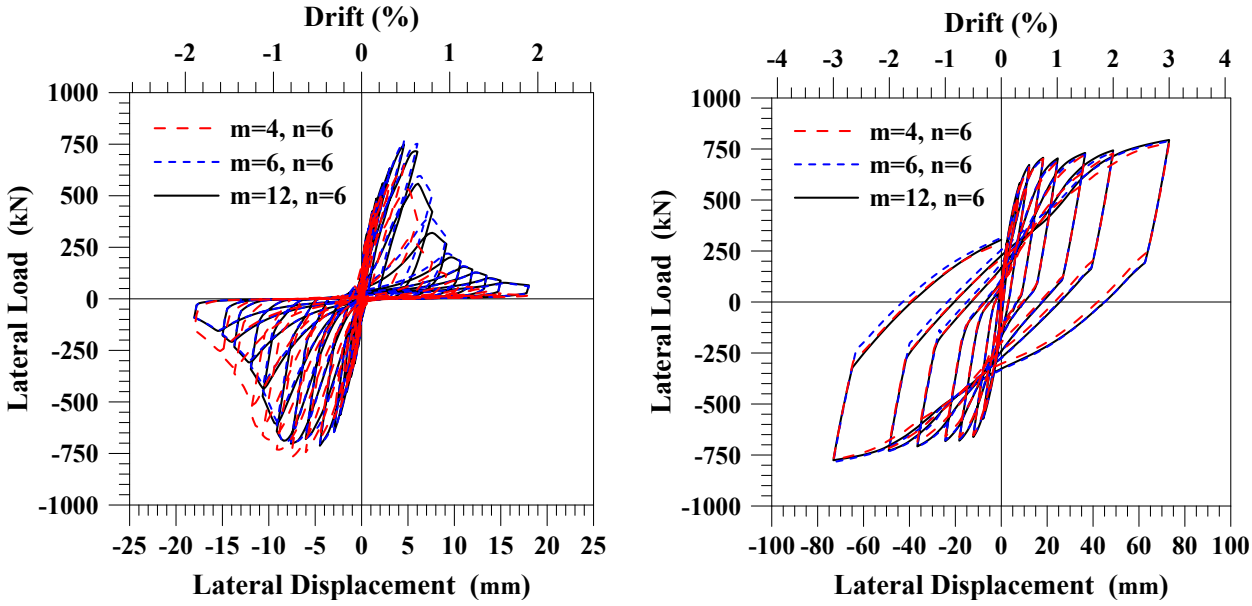

(a) SW-T2-S3-4.

(b) RW-A20-P10-S63.

Figure 4.31: Sensitivity analysis of the model to the number of RC panel elements.

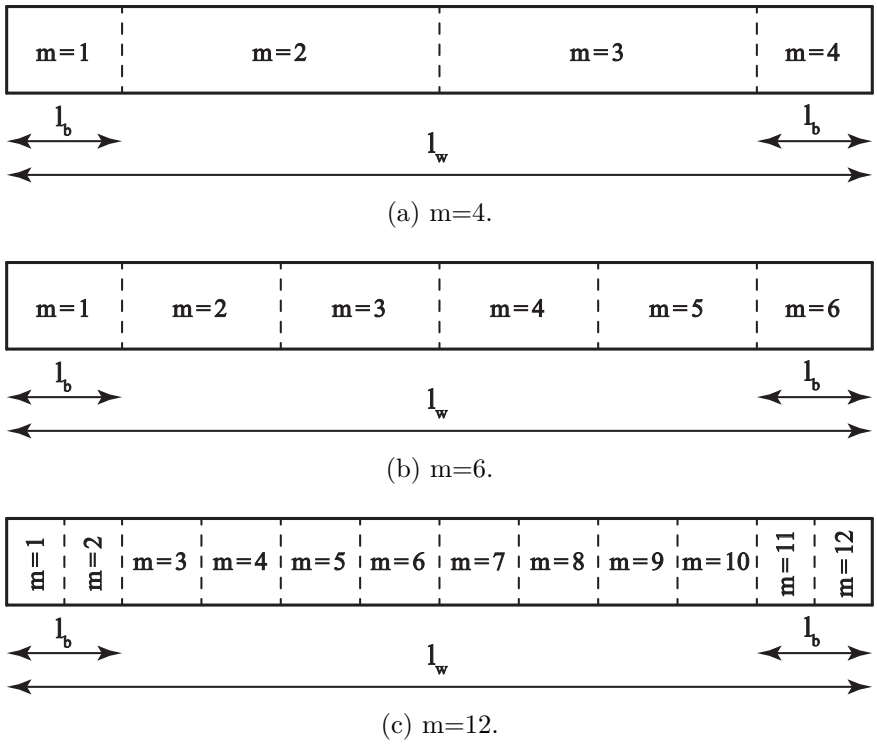

(a) m=4.

(b) m=6.

(c) m=12.

Figure 4.32: Layout of wall model horizontal discretization analysis.

In this study a number of at least $n = 6$ E-SFI elements and $m = 6$ RC panel elements are used to have an accurate representation of damage distribution, and the most strained element size match with the expected plastic hinge length to have an objective response. A plastic hinge length of $L_p = 0.5L_w$ is adopted for walls with a shear span-to-depth ratio greater than 1.0, whereas a value of $L_p = 2.0t_w$ is used for walls with a shear span-to-depth ratio less than or equal to 1.0 based on the work developed by Arteta (2015).

4.5. Shear strength test database comparison

The shear strength predicted by the E-SFI model is compared to a large database of 252 RC wall specimen tests reported in the literature, including the publications by Hirosawa (1975); Mohammadi-Doostdar & Saatcioglu (2002); Massone et al. (2009); Hidalgo et al. (2002); Yamada et al. (1974); Antebi et al. (1960); Barda et al. (1977); Benjamin & Williams (1957); Cardenas et al. (1980); and Galletly (1952). The database, described in Table A.1, includes walls with an aspect ratio (h_w/l_w) and a shear span-to-depth ratio (M/Vl_w) ranging from 0.29 to 2.0, tested under single curvature condition (cantilever configuration, 85%) or double curvature condition (zero rotation at wall ends, 15%), and with enlarged end section (flanged or barbell, 68%) or rectangular cross-sections (32%). The longitudinal boundary reinforcement ratio for the wall specimens ranges between 0.7% and 11.0% measured over the boundary cross-section, whereas the horizontal and vertical web reinforcement ratios vary from 0% to 3.7%. The yield strength of all reinforcing bars ranges between 209 MPa and 624 MPa, whereas the concrete compressive strength (f'_c) varies from 12.4 MPa to 63.4 MPa. A few cases of the wall specimens in the database were under axial load (28%), reaching values up to $0.27f'_c l_w t_w$, where l_w and t_w are the length and thickness of the wall, respectively. The shear strength is also estimated for the walls of the database using the ACI 318-19 code (Equation 18.10.4.1) as $V_n = \left(\alpha_c \lambda \sqrt{f'_c} + \rho_t f_{yt}\right) \cdot A_{cv}$, where λ is 1.0 for normal-weight concrete; α_c is 0.25 for $h_w/l_w \leq 1.5$, 0.17 for $h_w/l_w \geq 2.0$, and linearly interpolated between the limit aspect ratios, A_{cv} is the cross-sectional web area of the wall, ρ_t is the transverse web reinforcement ratio, and f_{yt} is the yield strength of the transverse reinforcement. Furthermore, the nominal shear strength for individual walls cannot be greater than $0.83A_{cw}\sqrt{f'_c}$, where A_{cw} represents the entire cross-sectional area of the wall (SI units). The cases where a flexural failure was expected were removed to avoid distortions in the analysis of the ACI 318-19 equation. The flexural capacity (M_n) was estimated based on the ACI 318-19 recommendations.

The analytical models were discretized in eight vertical elements and eight horizontal fibers, and the material models were adjusted to match with the as-tested material properties. To model a specimen under single curvature condition, the wall model is fully-fixed at the base and free to rotate at the wall top end, whereas to model a specimen under double curvature condition, the wall model is fully-fixed at the base and restrained to rotate at the wall top end. A top displacement-control analysis was performed to reach the shear strength of each computational model. As shown in Figure 4.33, the predicted shear stress by the model ($V_{model}/t_w l_w$) and by the ACI 318-19 code ($V_{ACI}/t_w l_w$) is compared to the experimentally measured shear stress ($V_{test}/t_w l_w$). Also, a trend line over the data is obtained for each case, and a dotted line in 45 degrees is added to represent a perfect relationship between both variables. The shear-flexure model trend line reveals that the model accurately reproduces

the shear stress of the tests with a R-squared value of 0.73. On the other hand, the ACI 318-19 code trend line reveals a more conservative prediction of the shear stress with a R-squared value of 0.28, indicating a larger dispersion than the shear-flexure model.

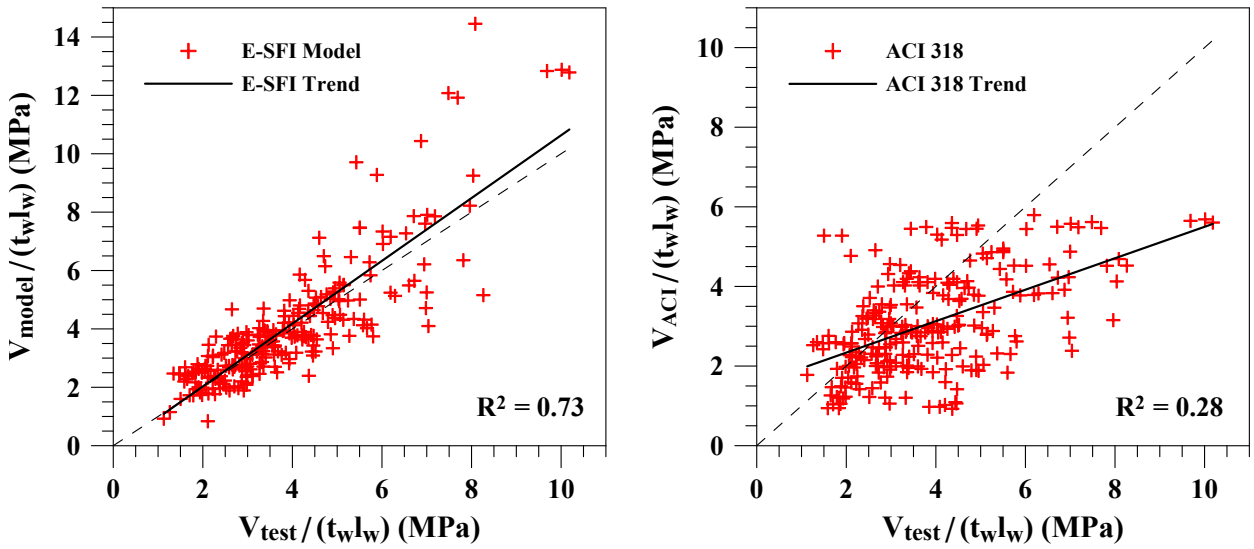

(a) Shear-flexure interaction model.

(b) ACI 318-19 code.

Figure 4.33: Predicted vs. experimentally measured shear stress.

The ratio of the predicted over the experimentally measured shear strength, also called strength ratio (V_{model}/V_{test}), was computed for all cases. The average strength ratio obtained using the shear-flexure model was 1.04, with a coefficient of variation (CV) of 0.23, indicating a good correlation of the shear-flexure interaction model with test results, and a relatively small dispersion. The maximum strength ratio was 1.83, whereas the minimum value was 0.54, however, most amount of them range between 0.6 and 1.4 (90%). A similar analysis was performed using the ACI 318-19 code, although, as mentioned above, a reduced version of the database is used to include only the cases were a shear failure was expected, obtaining an average strength ratio of 0.77, with a coefficient of variation of 0.37, indicating a much more conservative prediction and with a larger dispersion than the shear-flexure model. The maximum and minimum strength ratios were 1.93 and 0.21, respectively, although, most of them range between 0.3 and 1.3 (93%). The shear strength database used for the E-SFI model is the same used by Massone (2010) and Massone et al. (2020). The results obtained for each model are summarized in Table 4.4, revealing that the E-SFI formulation has a better correlation with experimental test results than both prior models.

Table 4.4: Comparative analysis of the strength ratio (V_{model}/V_{test}).

Model	Average	CV	Maximum	Minimum
Massone 2010	1.13	0.25	1.97	0.56
Massone et al. 2020	0.96	0.26	1.82	0.44
E-SFI	1.04	0.23	1.83	0.54
ACI 318-19	0.77	0.37	1.93	0.21

Although the E-SFI model has shown an accurate correlation with experimental test results, a sensitivity analysis of the shear strength ratio (V_{model}/V_{test}) was performed to investigate the performance of the model to variations in wall parameters. The sensitivity analysis was developed using the prescribed database, considering variation in parameters such as steel reinforcing ratios, concrete compressive strength, level of axial load, cross-section type, boundary condition, shear span-to-depth ratio, and observed average shear stress. The sensitivity analysis includes the strength ratio obtained by the shear-flexure model for all 252 cases, and by the ACI 31-19 code for the 210 shear controlled cases; furthermore, a trend line is obtained for each case by a linear best-fit analysis of the data, and a horizontal dotted line ($V_{model}/V_{test} = 1$) is added into figures to represent a perfect correlation. The sensitivity analysis is presented in the following sub-sections.

4.5.1. Sensitivity to horizontal web reinforcement

As shown in Figure 4.34, the shear strength ratio was plotted over the horizontal web reinforcing steel ratio times its yield strength, and therefore the horizontal axis indicates the force that the reinforcing steel can develop per unit area. The general trend of the E-SFI model shows a little dependence between the model prediction and the horizontal reinforcement, with a variation of approximately 20% over the whole range and an increasing tendency. The ACI 318-19 shear strength equation reveals a higher dependence to the horizontal reinforcement than the obtained by the shear-flexure model, with a variation of the prediction of about 30% over the whole range and an increasing tendency.

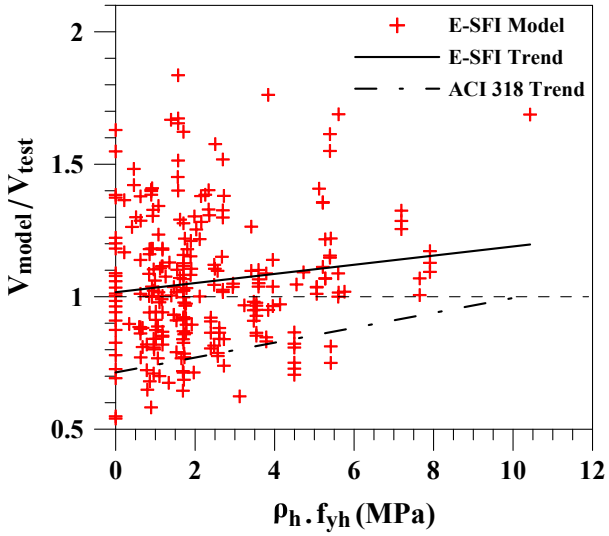

Figure 4.34: Shear strength ratio vs. horizontal web reinforcement.

4.5.2. Sensitivity to vertical web reinforcement

Figure 4.35 shows the model prediction sensitivity to the vertical web reinforcing steel ratio times its yield strength. The trend line of the E-SFI model reveals a little dependence between the model prediction and the vertical reinforcement, with a variation of approximately 15% over the whole range and an increasing tendency. On the other hand, the ACI 318-19 strength equation shows a higher dependence to the vertical reinforcement than the obtained by the shear-flexure model, with a variation of the prediction of about 30% over the whole range and an increasing tendency.

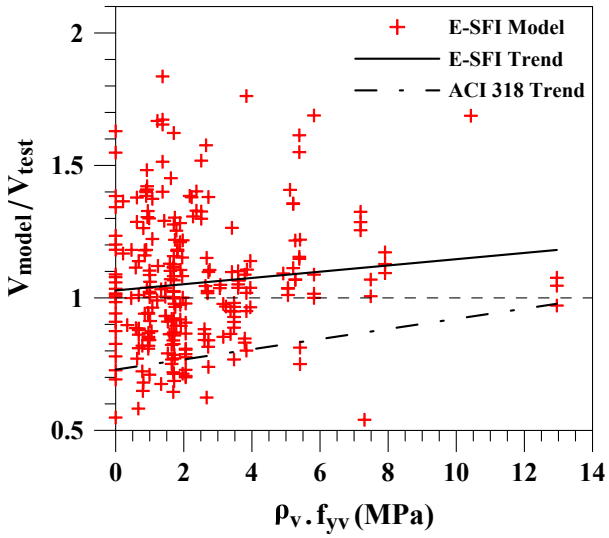

Figure 4.35: Shear strength ratio vs. vertical web reinforcement.

4.5.3. Sensitivity to longitudinal boundary reinforcement

As shown in Figure 4.36, the shear strength ratio was plotted over the longitudinal boundary reinforcing steel ratio times its yield strength. The general trend of the E-SFI model shows a relatively small dependence between the model prediction and the longitudinal boundary reinforcement, with a variation of approximately 10% over the whole range and an increasing tendency. The ACI 318-19 shear strength equation reveals a higher dependence to the longitudinal boundary reinforcement than the obtained by the shear-flexure model, with a variation of about 15% over the whole range and a decreasing tendency.

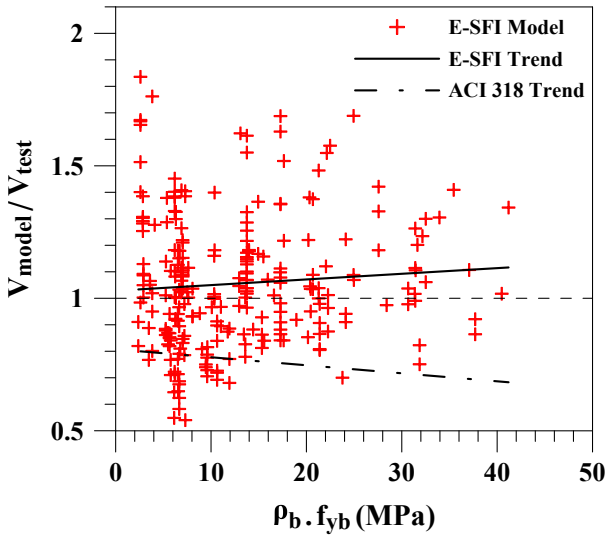

Figure 4.36: Shear strength ratio vs. longitudinal boundary reinforcement.

4.5.4. Sensitivity to concrete compressive strength

Figure 4.37 shows the model prediction sensitivity to the concrete compressive strength. The trend line of the E-SFI model data shows a relatively small dependence between the model and the concrete compressive strength, with a variation of approximately 10% over the whole range and an increasing tendency. The ACI 318-19 shear strength equation reveals a higher dependence to the concrete compressive strength than the obtained by the shear-flexure model, with a variation of the prediction of about 30% over the whole range and a decreasing tendency.

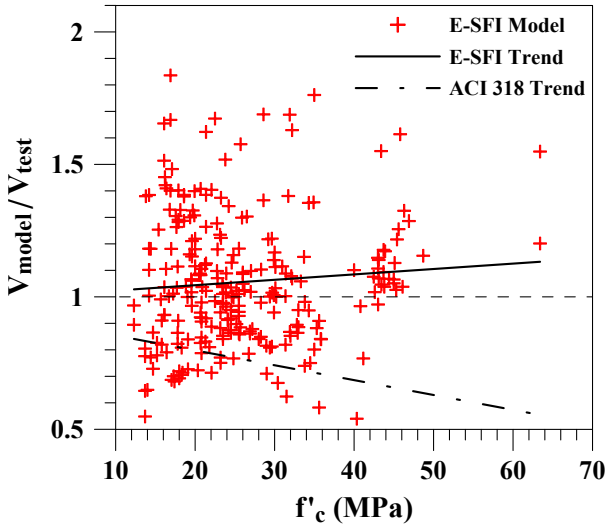

Figure 4.37: Shear strength ratio vs. concrete compressive strength.

4.5.5. Sensitivity to shear span-to-depth ratio

As shown in Figure 4.38, the shear strength ratio was plotted over the shear span-to-depth ratio. The trend line of the E-SFI model shows a variation of approximately 20% over the whole range, indicating a little dependence of the model with the shear span-to-depth ratio; furthermore, the model tendency reveals an over-estimation of the shear capacity for small values of the parameter under study. The ACI 318-19 shear strength equation shows a lower dependence to the shear span-to-depth ratio than the obtained by the shear-flexure model, with a variation of the prediction of about 10% and a decreasing tendency; furthermore, the shear strength is underestimated over the whole range.

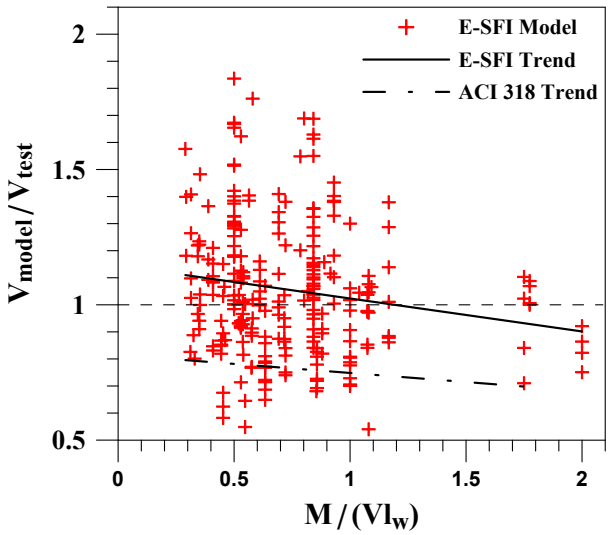

Figure 4.38: Shear strength ratio vs. shear span-to-depth ratio.

4.5.6. Sensitivity to axial load

Figure 4.39 shows the model prediction sensitivity to the axial load level; however, it must be noted that only a few cases have an axial load level grater than $0.01 f'_c t_w l_w$ (15% of the database). The general trend of the E-SFI model shows a variation of approximately 30% over the whole range, indicating a moderate dependence of the model with the axial load level. On the other hand, the ACI 318-19 shear strength equation reveals a slightly lower dependence to the axial load level than the obtained by the shear-flexure model, with a variation of the prediction of about 25% and a decreasing tendency, furthermore, the shear strength equation shows a conservative behavior over the whole range.

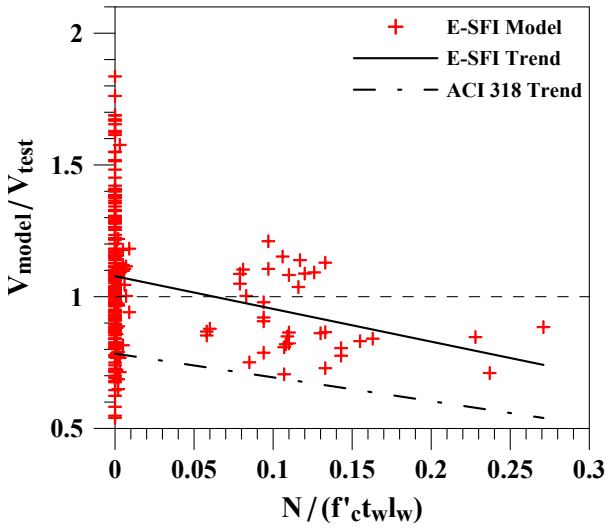

Figure 4.39: Shear strength ratio vs. axial load level.

4.5.7. Sensitivity to wall shape and boundary condition

As shown in Figure 4.40, the shear strength ratio was plotted over the cross-sectional wall shape (enlarged or rectangular) and the boundary condition (single and double curvature). The E-SFI model results reveal an average slightly better prediction for walls with rectangular cross-sectional shape and with single curvature boundary conditions; however, no-dependence of the model with the cross-sectional shape nor the boundary condition of the wall is observed, as well as for the ACI 318-19 shear strength equation.

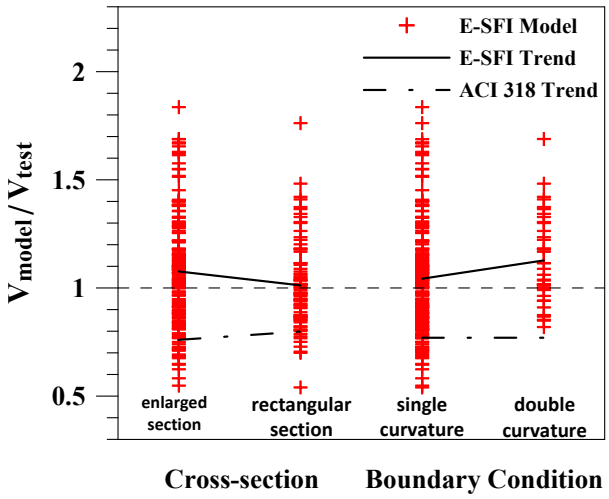

Figure 4.40: Shear strength ratio vs. cross-sectional shape and boundary condition.

4.5.8. Sensitivity to average observed (experimental) shear stress

Figure 4.41a shows the model prediction sensitivity to the average observed (experimental) shear stress. The general trend of the E-SFI model shows a variation of approximately 20% over the whole range, indicating a little dependence of the model to the average observed shear stress; furthermore, the model tendency reveals an over-estimation of the shear capacity for small values of the parameter under study. The ACI 318-19 shear strength equation shows a higher dependence to the average shear stress than the obtained by the shear-flexure model, with a variation of the prediction of about 70% and a decreasing conservative tendency. Figure 4.41b includes the analytical results for the ACI 318-19 strength equation for all 252 specimens of the database, including those expected to have a flexural failure, differentiating the cases where shear or flexural failure mode is expected. As can be seen from Figure 4.41b, large over-predictions of the shear capacity (V_n) based on the ACI 318-19 shear strength equation are obtained for walls expected to have a flexural behavior; however, they are partially corrected based on the flexural capacity (M_n). Therefore, over-prediction is expected when a different failure mode governs the response.

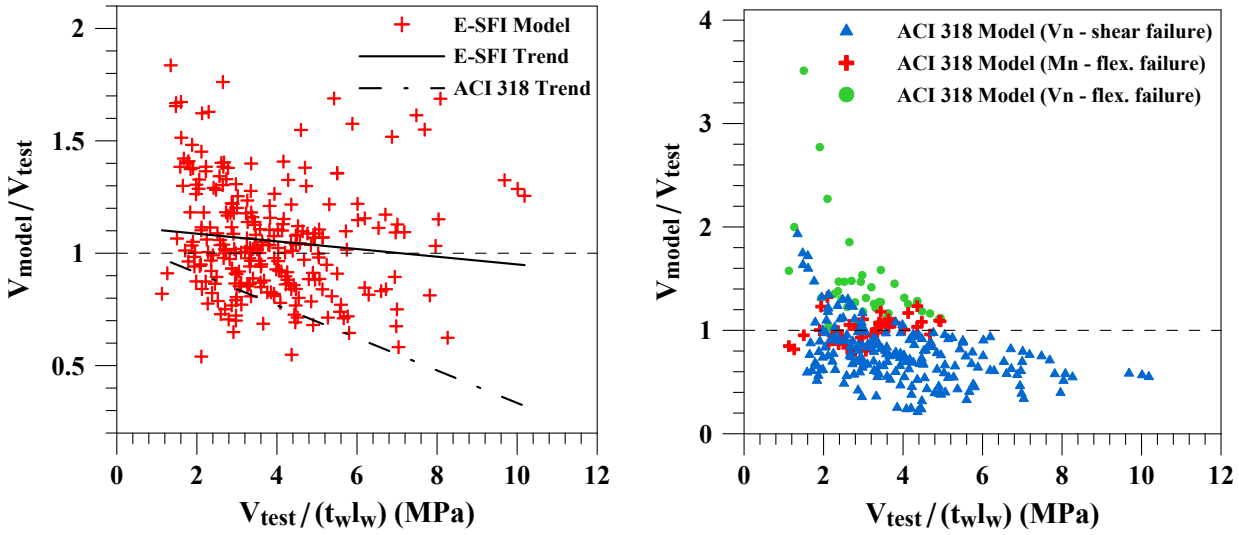

(a) Shear-flexure interaction model.

(b) ACI 318-19 code.

Figure 4.41: Shear strength ratio vs. experimental shear stress.

4.6. Comparison of model predictions with experimental data

The analytically predicted and experimentally measured responses, at both global and local response levels, are compared for the ten selected RC walls described in Section 4.1. The predicted cracking pattern is obtained using the orientation and strains of the concrete struts from each RC panel model when a crack is formed. A blue line is used for compressive strains (crack closed), whereas a red line is used for tensile strains (crack open). The line-width represents the magnitude of the strains proportional to the width-scale presented in each figure; however, a minimum line-width is used to facilitate the visualization.

4.6.1. Specimen RW2

As shown in Figure 4.42, the analytical model accurately replicates the shape of the hysteretic loops of the global response for the slender wall specimen RW2. The stiffness is initially overestimated and is well represented for drift levels greater than 0.2%. The lateral load attained at each drift level is accurately estimated; however, the model does not predict the initiation of lateral load capacity degradation, probably due to the absence of a rebar buckling mechanism into the model formulation, as occurred in the experimental test. The flexural and shear deformation responses at first story level (at the bottom quarter of the wall) are presented in Figure 4.43. The analytical model slightly underestimates the shear deformation component; however, due to their relatively small magnitude is not relevant since the wall is flexural-dominated, indicating that the model captures reasonably well the interaction between flexural and shear deformation components. The predicted cracking pattern at drift level of 3.0% is shown in Figure 4.44, revealing typical crack orientations of flexural-dominated walls.

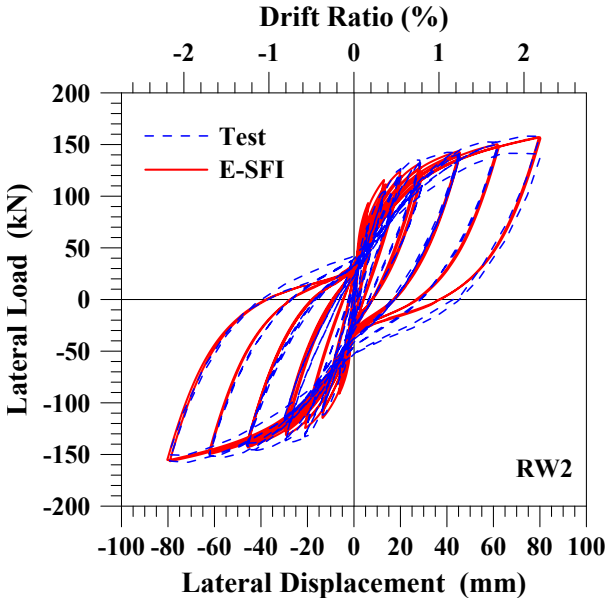

Figure 4.42: Lateral load vs. top displacement response for specimen RW2.

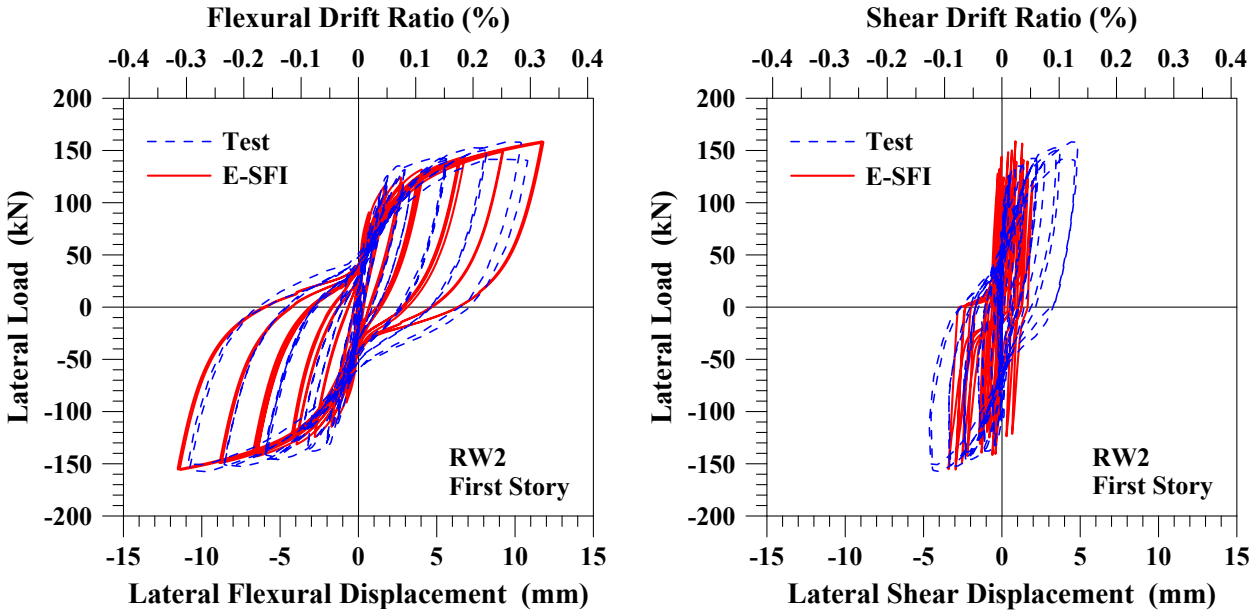

(a) Flexural response.

(b) Shear response.

Figure 4.43: Lateral load vs. first story flexural and shear displacement responses of specimen RW2.

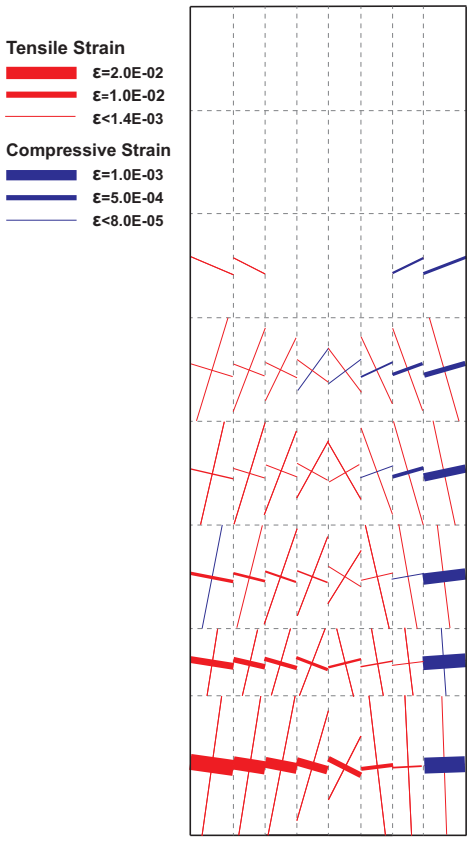

Figure 4.44: Analytical cracking pattern for specimen RW2 at 3.0% drift.

4.6.2. Specimen RW-A20-P10-S38

The global response for the medium-rise wall specimen RW-A20-P10-S38 is shown in Figure 4.45, revealing an accurate analytical model prediction of the hysteretic loops with a slight overestimation of the pinching behavior. The stiffness is initially overestimated and is in reasonable agreement for drift levels greater than 0.5%. The lateral load attained at each drift level is slightly underestimated for the major part of the test. The initiation of lateral load capacity degradation during the last cycle is not captured, probably due to the absence of a rebar buckling mechanism into the model formulation, as occurred in the experimental test. The top flexural and shear displacement responses are presented in Figure 4.46. The analytical model accurately replicates the flexural and shear deformation components at each drift level. Figure 4.47 reveals that the analytical model developed flexural cracks at wall boundaries and shear cracks towards the wall center, extended to approximately 3/4 of the wall height, which is in agreement with the experimentally observed cracking pattern.

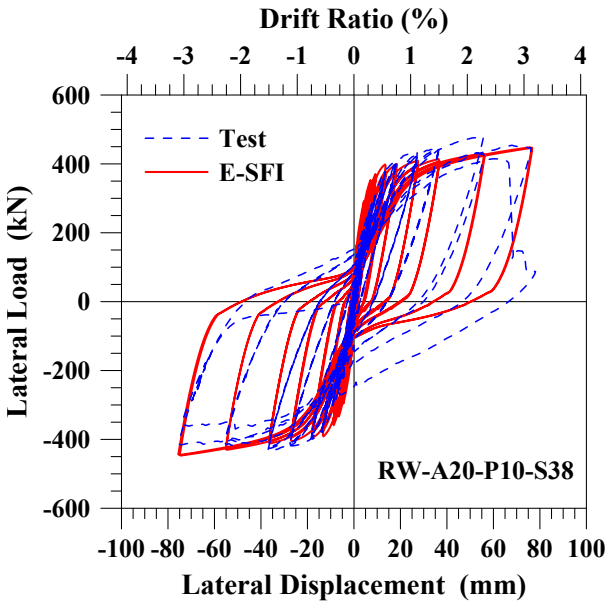

Figure 4.45: Lateral load vs. top displacement response for specimen RW-A20-P10-S38.

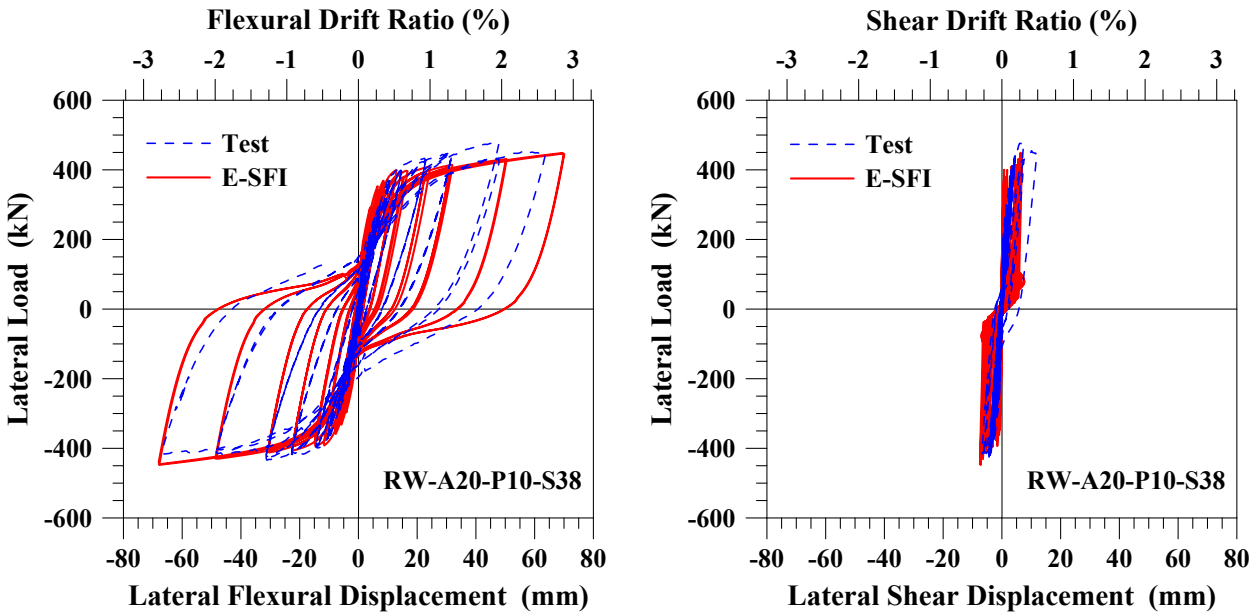

(a) Flexural response.

(b) Shear response.

Figure 4.46: Lateral load vs. top flexural and shear displacement responses for specimen RW-A20-P10-S38.

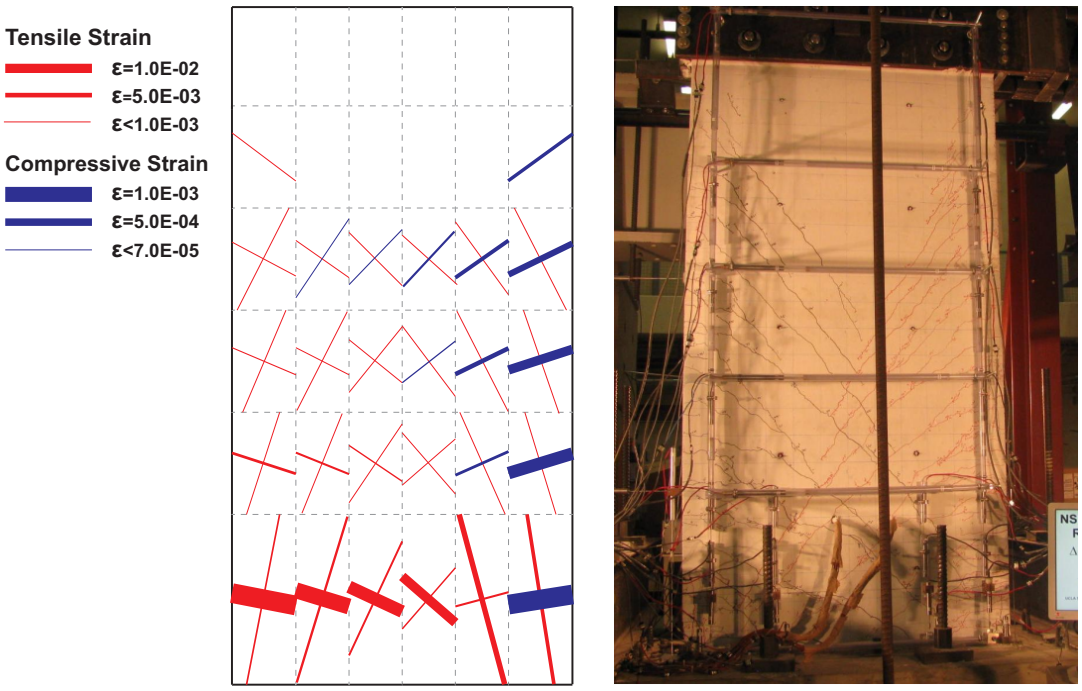

(a) Analytical cracking pattern.

(b) Experimental cracking pattern (Tran, 2012).

Figure 4.47: Analytical and experimental cracking patterns for specimen RW-A20-P10-S38 at 1.5% drift.

4.6.3. Specimen RW-A20-P10-S63

As shown in Figure 4.48, the analytical model accurately reproduces the shape of the hysteretic loops of the global response for the medium-rise wall specimen RW-A20-P10-S63. The stiffness and lateral load capacity are initially overestimated and are in reasonable agreement for drift levels above 0.5%. The model does not predict the lateral load capacity degradation at the last drift level, probably due to the absence of a rebar buckling mechanism into the model formulation, as occurred in the specimen test. The top flexural and shear responses are presented in Figure 4.49. The analytical model shows a reasonably accurate prediction of the deformation components at each drift level, although the flexural component is slightly overestimated for the last cycle. Figure 4.50 shows that the model developed flexural cracks at wall boundaries and shear cracks along the wall web, extended over the entire wall height, as occurred in the experimental test.

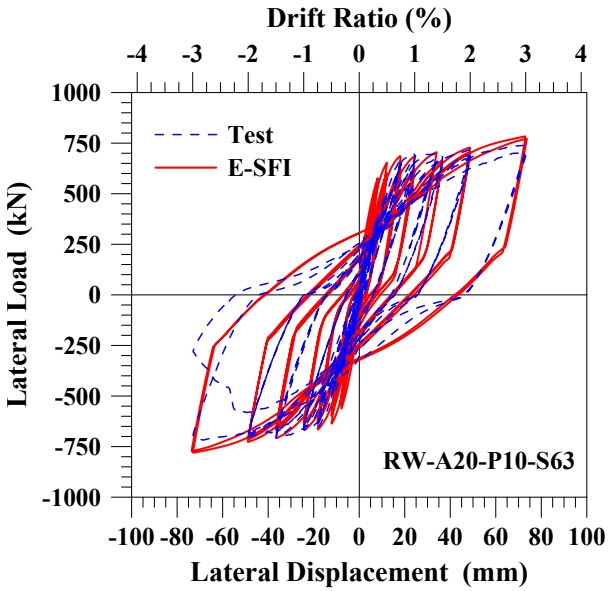

Figure 4.48: Lateral load vs. top displacement response for specimen RW-A20-P10-S38.

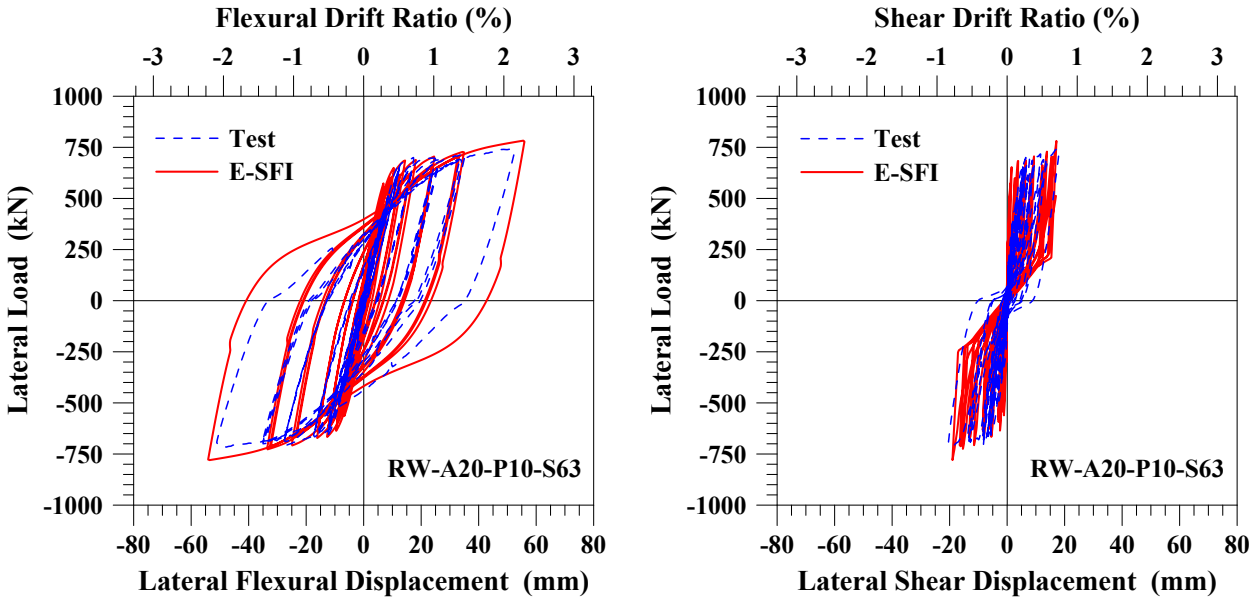

(a) Flexural response.

(b) Shear response.

Figure 4.49: Lateral load vs. top flexural and shear displacement responses for specimen RW-A20-P10-S63.

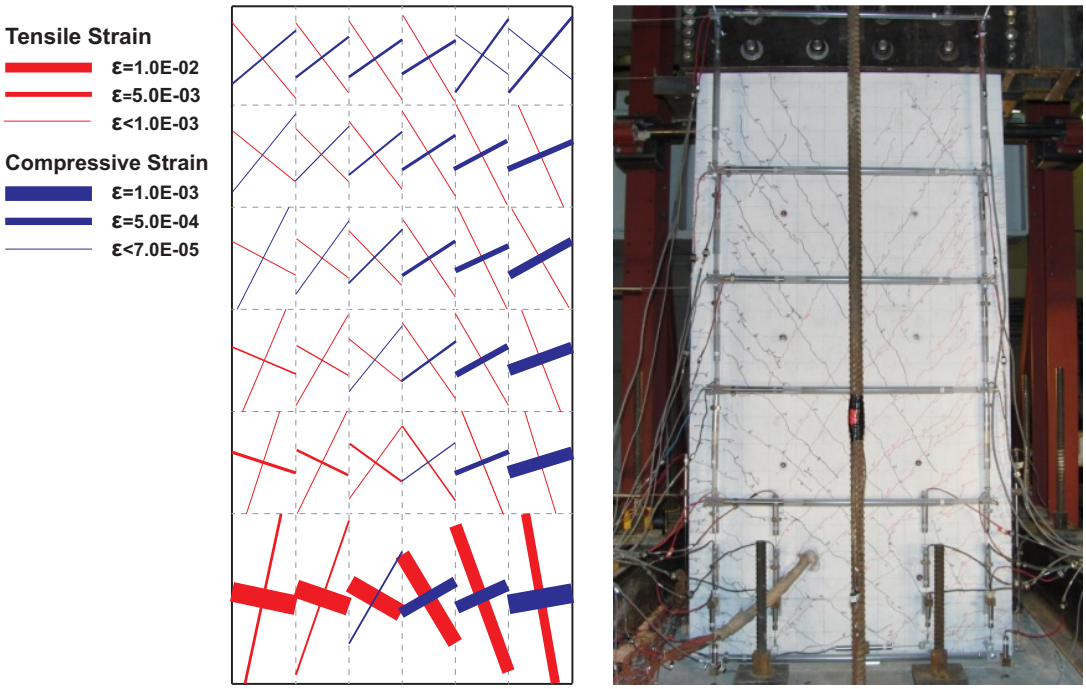

(a) Analytical cracking pattern.

(b) Experimental cracking pattern (Tran, 2012).

Figure 4.50: Analytical and experimental cracking patterns for specimen RW-A20-P10-S63 at 1.5% drift.

4.6.4. Specimen RW-A15-P10-S51

The global response for the medium-rise wall specimen RW-A15-P10-S51 is shown in Figure 4.51, revealing an accurate analytical model prediction of the hysteretic loops with a slight overestimation of the pinching behavior. The stiffness is initially overestimated and is in reasonable agreement for drift levels greater than 0.5%. The lateral load level attained at each drift level is slightly overestimated. The initiation of lateral load degradation during the last cycle is not captured, probably due to the absence of a rebar buckling mechanism into the model formulation, as occurred in the experimental test. The top flexural and shear displacement responses are presented in Figure 4.52. The analytical model reasonably replicates the flexural and shear components at each drift level, although the flexural component is slightly overestimated for the last negative cycle. Figure 4.53 reveals that the analytical model developed flexural cracks at wall boundaries and shear cracks towards the wall center, extended over the entire wall height, which agrees with the experimentally observed cracking pattern.

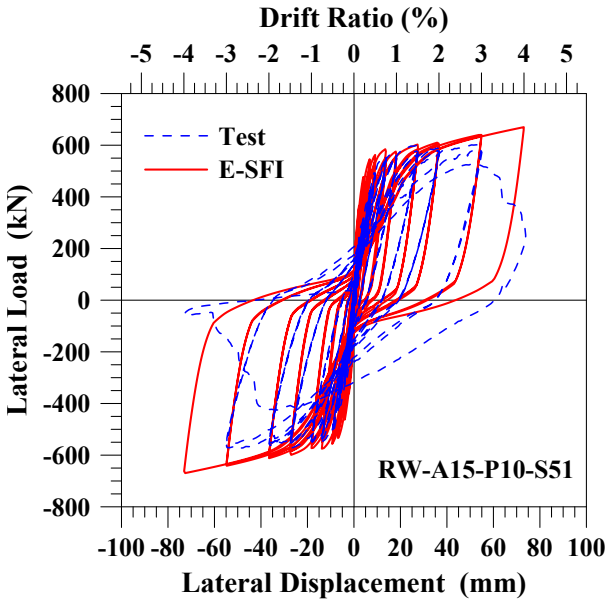

Figure 4.51: Lateral load vs. top displacement response for specimen RW-A15-P10-S51.

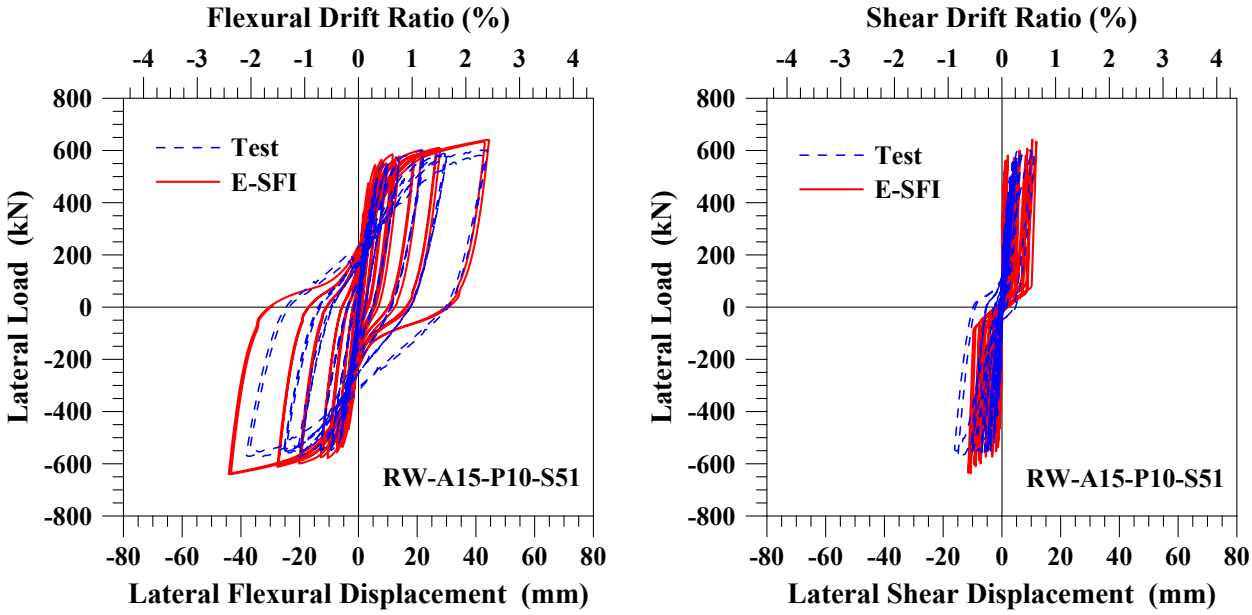

(a) Flexural response.

(b) Shear response.

Figure 4.52: Lateral load vs. top flexural and shear displacement responses for specimen RW-A15-P10-S51.

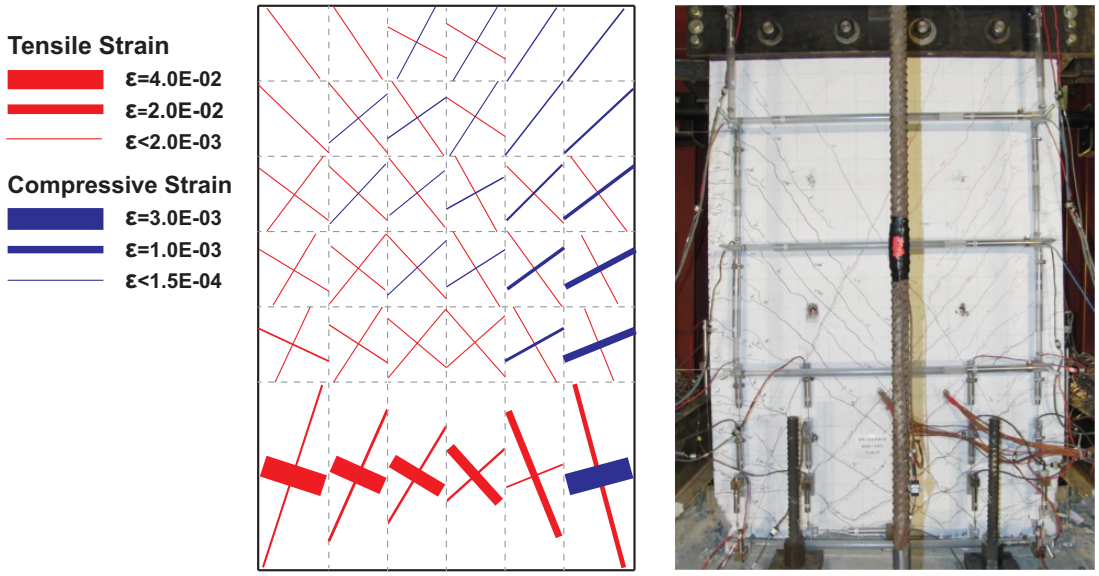

(a) Analytical cracking pattern.

(b) Experimental cracking pattern (Tran, 2012).

Figure 4.53: Analytical and experimental cracking patterns for specimen RW-A15-P10-S51 at 3.0% drift.

4.6.5. Specimen RW-A15-P10-S78

As shown in Figure 4.54, the analytical model accurately reproduces the shape of the hysteretic loops of the global response for the medium-rise wall specimen RW-A15-P10-S78. The stiffness is initially overestimated and is in reasonable agreement for drift levels greater than 0.5%. The lateral load attained at each drift level is slightly overestimated. The model does not predict the lateral load capacity degradation during the first cycle to 3.0% drift caused by diagonal compressive concrete struts at the wall bottom boundaries; furthermore, the model does not capture the abrupt strength degradation during the second cycle to 3.0% drift associated with lateral instability and shear sliding mechanisms because of the inability of the model to simulate such failure modes. The top flexural and shear displacement responses are presented in Figure 4.55. The analytical model shows a reasonably accurate prediction of the deformation components at each cycle, although the flexural component is overestimated for the last drift level. Figure 4.56 shows that the model developed flexural cracks at wall boundaries and shear cracks along the wall web extended over the entire wall height, as occurred in the specimen test.

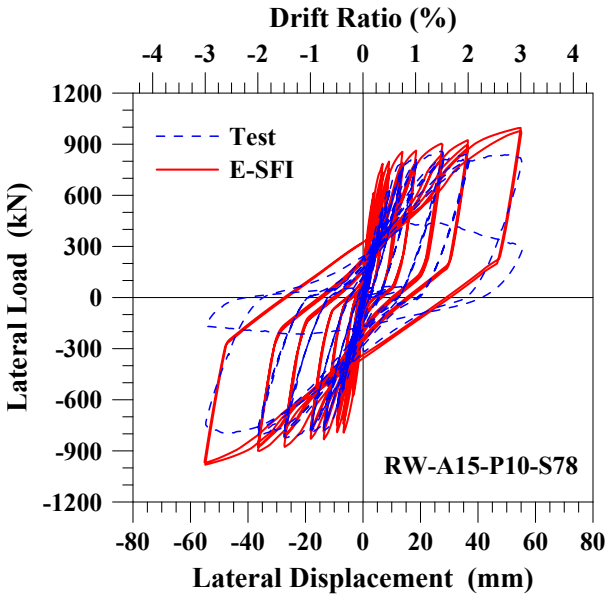

Figure 4.54: Lateral load vs. top displacement response for specimen RW-A15-P10-S78.

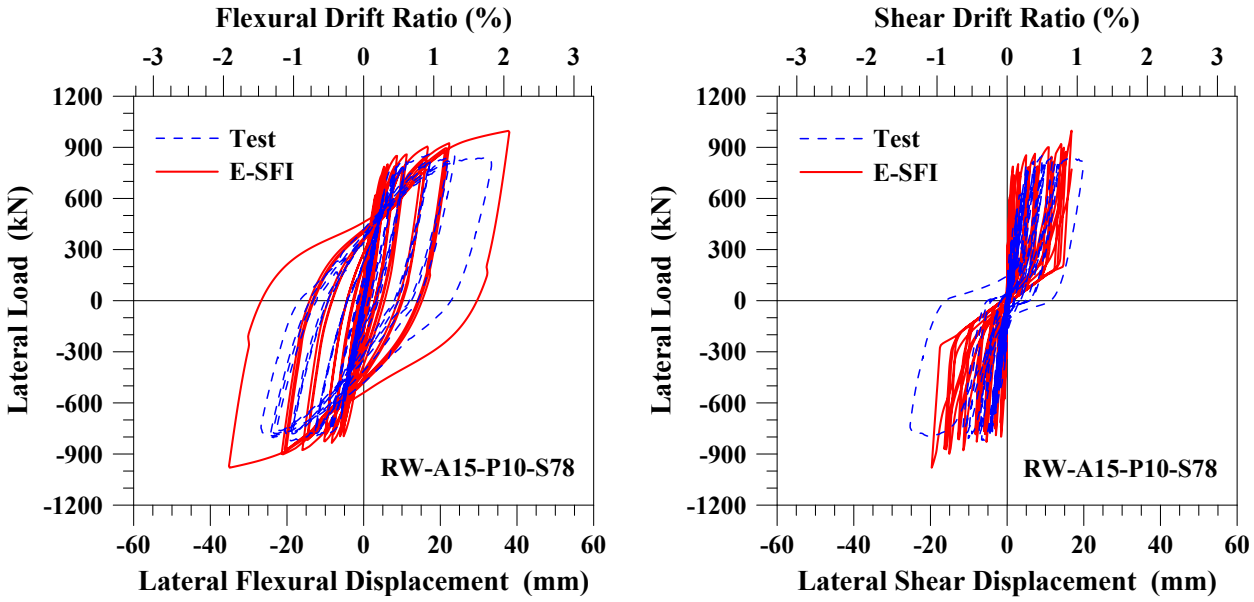

(a) Flexural response.

(b) Shear response.

Figure 4.55: Lateral load vs. top flexural and shear displacement responses for specimen RW-A15-P10-S78.

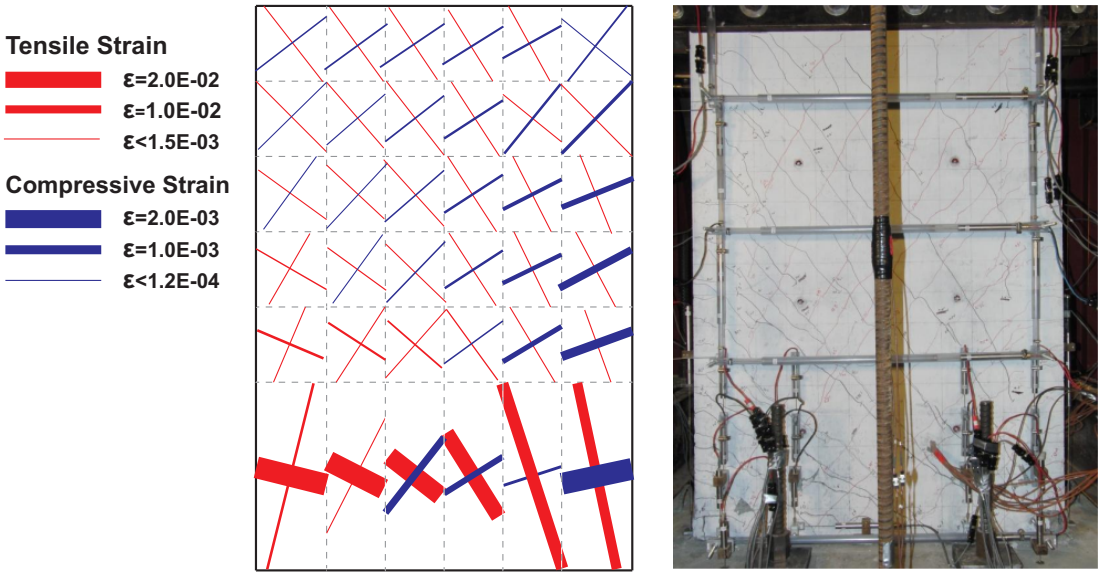

(a) Analytical cracking pattern.

(b) Experimental cracking pattern (Tran, 2012).

Figure 4.56: Analytical and experimental cracking patterns for specimen RW-A15-P10-S78 at 2.0% drift.

4.6.6. Specimen SW-T2-S3-4

The global response for the squat wall specimen SW-T2-S3-4 is shown in Figure 4.57, revealing a reasonably accurate analytical model prediction of the hysteretic loops. The stiffness is initially underestimated and in reasonable agreement for drift levels greater than 0.5%. The lateral load attained at each drift level is slightly underestimated. The average shear strength (including positive and negative direction) is underestimated by approximately 12%. The asymmetric response is accurately replicated by the model, including the initiation of lateral load degradation for each direction. The model strength degradation was initiated by concrete crushing at the wall bottom and propagated over the element length for the following cycles, indicating a diagonal compression failure, as occurred in the experimental test. The top flexural and shear deformation responses are presented in Figure 4.58. The analytical model accurately replicates the contribution of the flexural and shear deformation components at each drift level. The asymmetry of the shear response is not captured by the model, causing a slight overestimation of the shear component for positive direction. Figure 4.59 reveals that the analytical model developed principally shear cracks over the entire wall with a slight contribution of flexure toward wall bottom boundaries, as occurred in the experimental test.

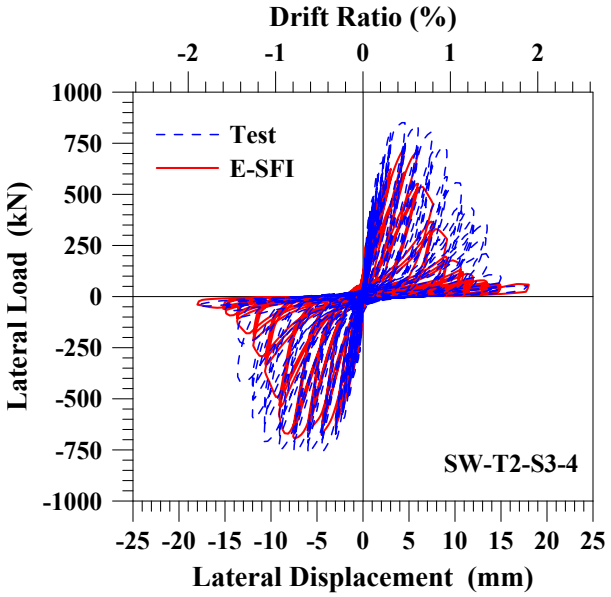

Figure 4.57: Lateral load vs. top displacement response for specimen SW-T2-S3-4.

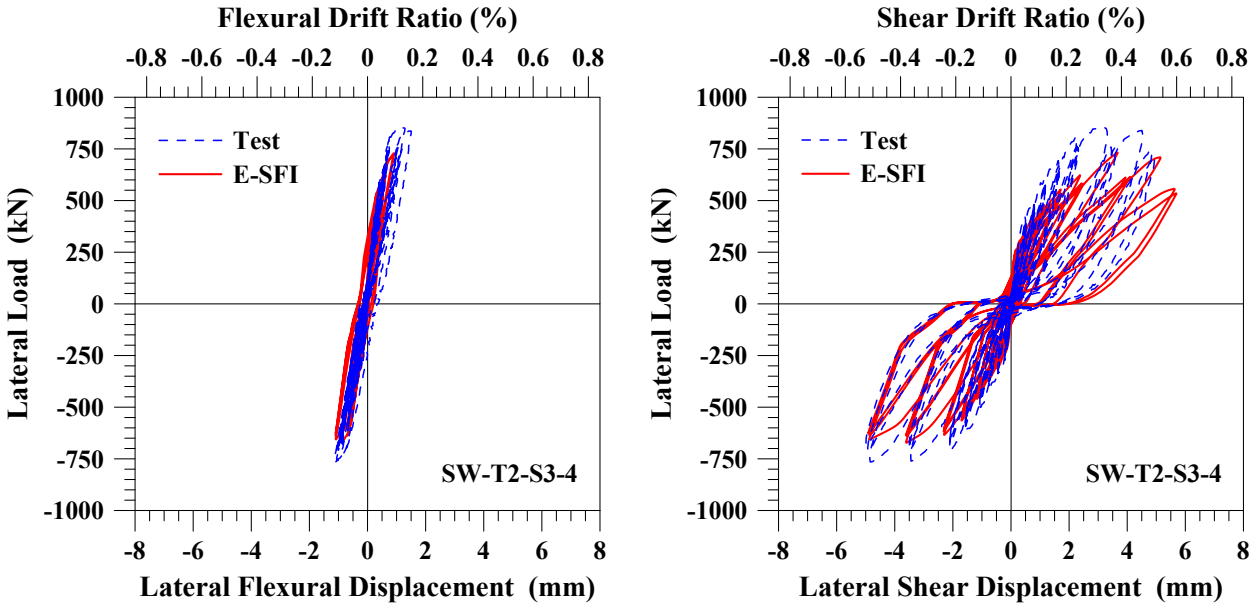

(a) Flexural response.

(b) Shear response.

Figure 4.58: First story lateral load vs. flexural and shear displacement responses for specimen SW-T2-S3-4.

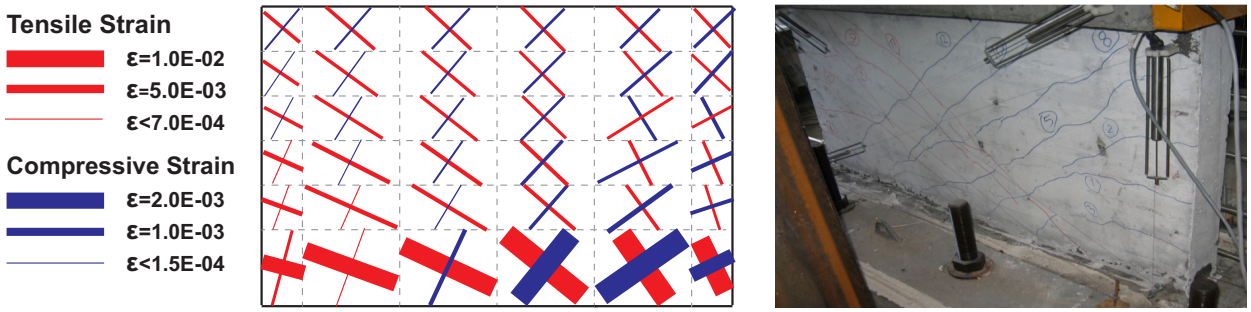

(a) Analytical cracking pattern.

(b) Experimental cracking pattern (Terzioglu, 2011).

Figure 4.59: Analytical and experimental cracking patterns for specimen SW-T2-S3-4 at 0.6% drift.

4.6.7. Specimen SW-T4-S1-6

As shown in Figure 4.60, the analytical model accurately reproduces the shape of the hysteretic loops of the global response for the squat wall specimen SW-T4-S1-6. The stiffness is initially underestimated and is in reasonable agreement for drift levels greater than 0.5%. The lateral load attained at each drift level is slightly underestimated. The average shear strength (including positive and negative direction) is underestimated by approximately 7%. The asymmetric response is accurately captured by the model, as well as the initiation of lateral load capacity degradation for each direction. The model capacity degradation was initiated by concrete crushing at the wall bottom and propagated over the element length for the subsequent cycles, indicating a diagonal compression failure, as occurred in the experimental test. The top flexural and shear deformation responses are presented in Figure 4.61. The analytical model shows a reasonably accurate prediction of the deformation components at each cycle. The asymmetry of the flexural and shear components are not captured by the model, causing a slight overestimation of the shear component for positive direction. Figure 4.62 shows that the model developed shear cracks over the entire wall height with slight contribution of flexure toward bottom boundaries.

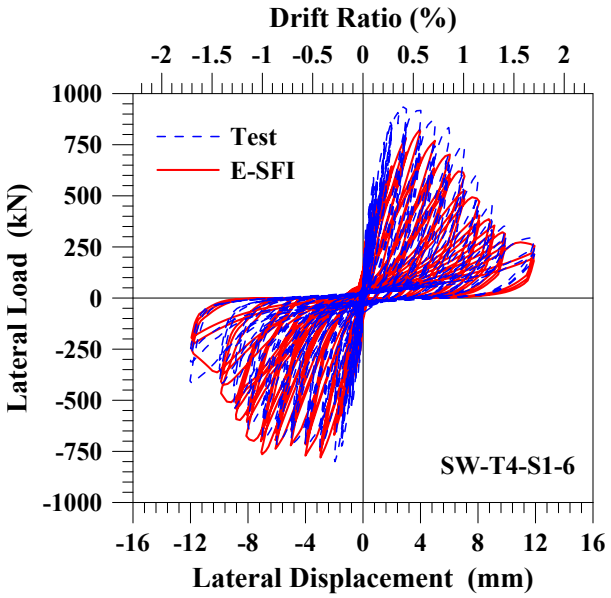

Figure 4.60: Lateral load vs. top displacement response for specimen SW-T4-S1-6.

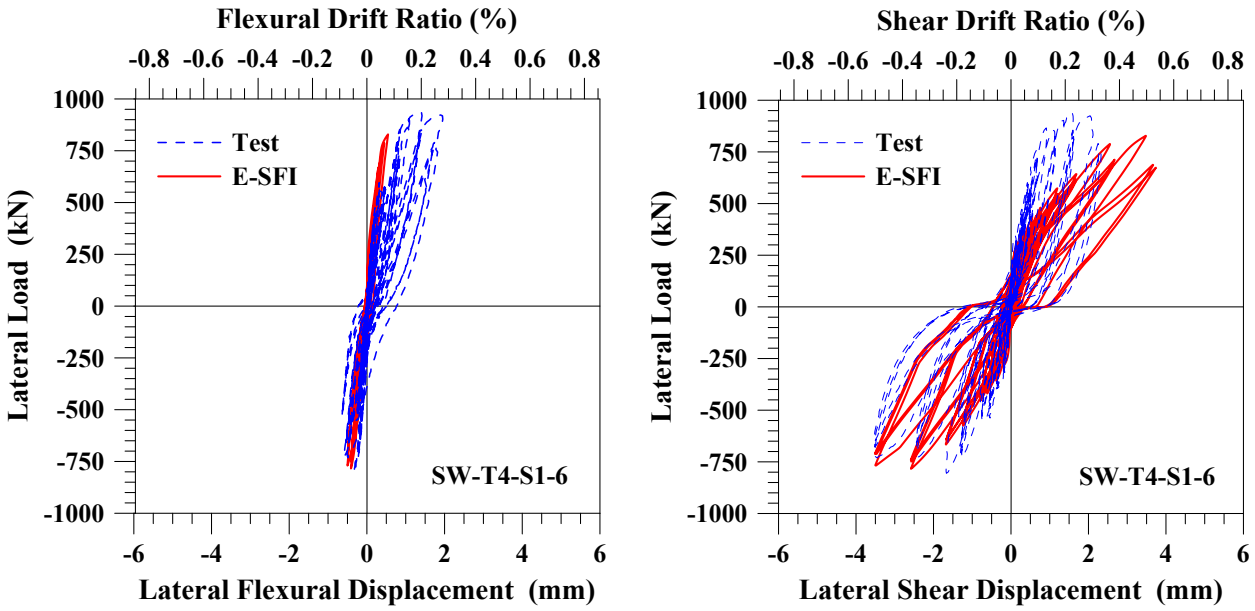

(a) Flexural response.

(b) Shear response.

Figure 4.61: First story lateral load vs. flexural and shear displacement responses for specimen SW-T4-S1-6.

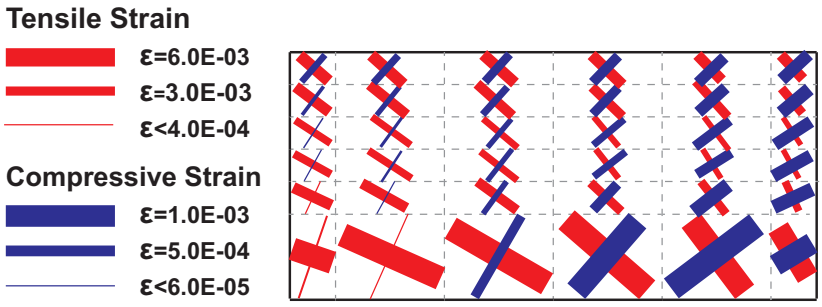

(a) Analytical cracking pattern.

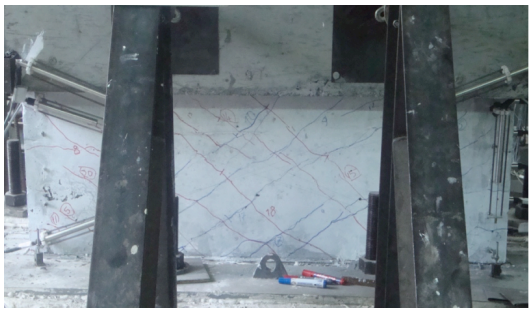

(b) Experimental cracking pattern (Terzioglu, 2011).

Figure 4.62: Analytical and experimental cracking patterns for specimen SW-T4-S1-6 at 0.6% drift.

4.6.8. Specimen SW-T6-S1-8

The global response for the squat wall specimen SW-T6-S1-8 is shown in Figure 4.63, revealing an accurate analytical prediction of the hysteretic loops. The stiffness is initially underestimated and is in agreement for drift levels above 0.4%. The lateral load level attained at each drift level is slightly underestimated for the major part of the test. The average shear strength (including positive and negative direction) is underestimated by approximately 11%. The analytical model prematurely initiates lateral load capacity degradation for positive direction, whereas capacity degradation initiation is reasonably replicated for negative direction. The model strength degradation was initiated by concrete crushing at the wall bottom and propagated over the element length for the subsequent cycles, indicating a diagonal compression failure, as occurred in the experimental test. The top flexural and shear deformation components are presented in Figure 4.64. The analytical model replicates reasonably well the contribution of flexural and shear deformation components at each drift level. The model overestimates the shear contribution for positive cycles, which caused the premature initiation of lateral load capacity degradation for this direction, whereas, for negative cycles, the flexural and shear contributions are reasonably captured. Figure 4.65 reveals that the analytical model developed principally shear cracks over the entire wall with a slight contribution of flexure toward wall bottom boundaries, as occurred in the experimental wall test.

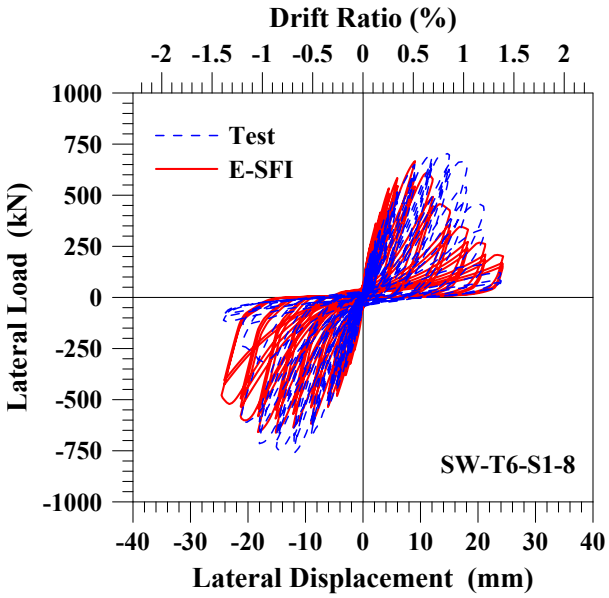

Figure 4.63: Lateral load vs. top displacement response for specimen SW-T6-S1-8.

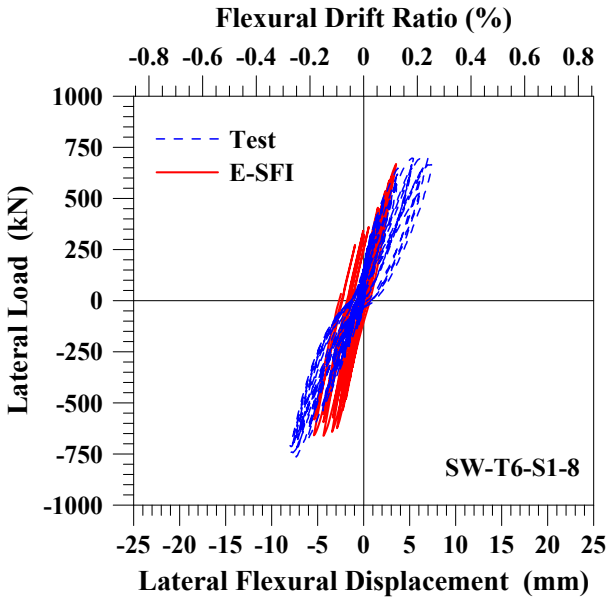

(a) Flexural response.

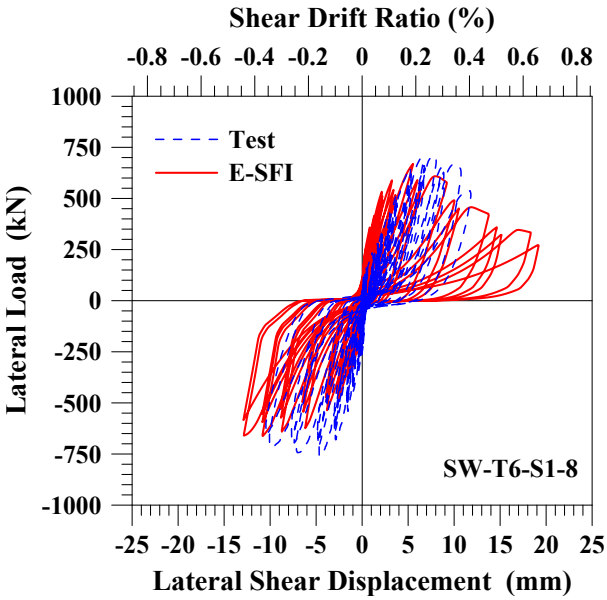

(b) Shear response.

Figure 4.64: First story lateral load vs. flexural and shear displacement responses for specimen SW-T6-S1-8.

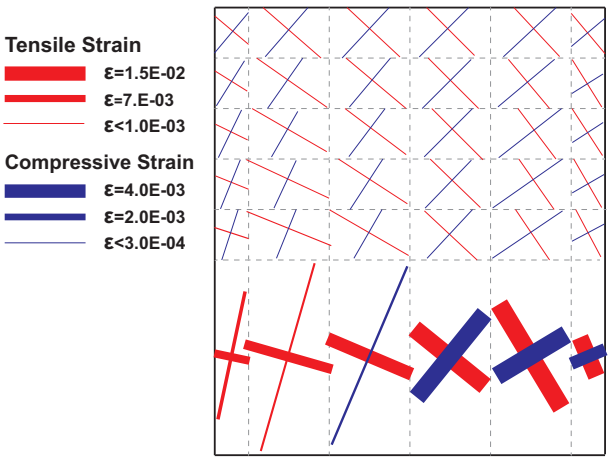

(a) Analytical cracking pattern.

(b) Experimental cracking pattern (Terzioglu, 2011).

Figure 4.65: Analytical and experimental cracking patterns for specimen SW-T6-S1-8 at 1.0% drift.

4.6.9. Specimen WP-T5-N0-S1

As shown in Figure 4.66, the analytical model accurately reproduces the shape of the hysteretic loops of the global response for the squat wall specimen WP-T5-N0-S1. The stiffness is initially overestimated and is in reasonable agreement for drift levels greater than 0.4%. The predicted lateral load attained at each drift level is generally in concordance with experimental test results. The average shear strength (including positive and negative direction) is overestimated by less than 1%. The analytically predicted load capacity degradation was initiated by large shear strains, causing concrete crushing and yielding of the horizontal reinforcement, indicating a diagonal tension failure, as occurred in the experimental test. The top flexural and shear deformation responses are presented in Figure 4.67. The analytical model shows a reasonably accurate prediction of the flexural and shear deformation components at each cycle. The model tends to slightly overestimate the shear contribution, whereas the flexural contribution is generally underestimated. Figure 4.68 shows that the model developed shear cracks over the entire wall with a marginal flexural contribution toward bottom boundaries, similar to the experimentally observed cracking pattern.

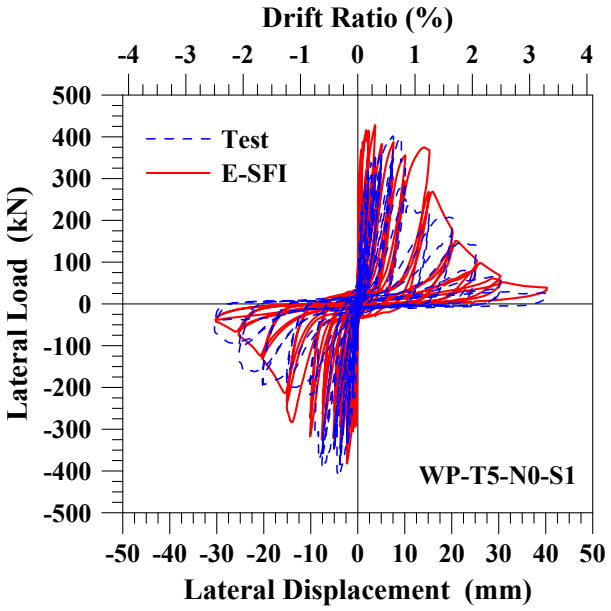

Figure 4.66: Lateral load vs. top displacement response for specimen WP-T5-N0-S1.

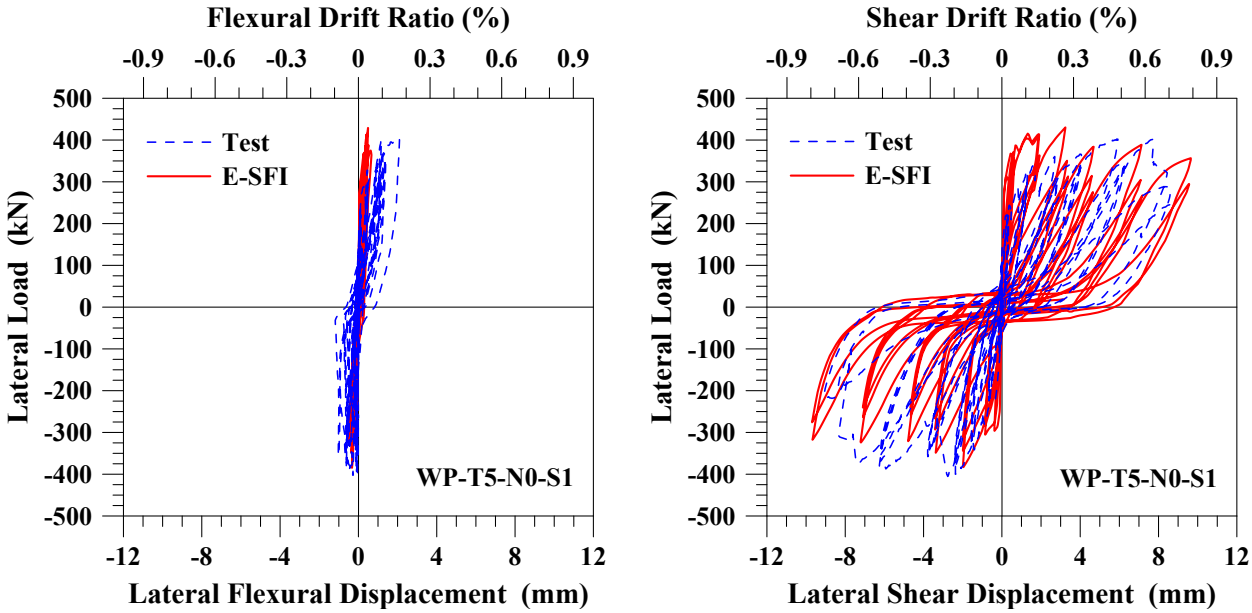

(a) Flexural response.

(b) Shear response.

Figure 4.67: First story lateral load vs. flexural and shear displacement responses for specimen WP-T5-N0-S1.

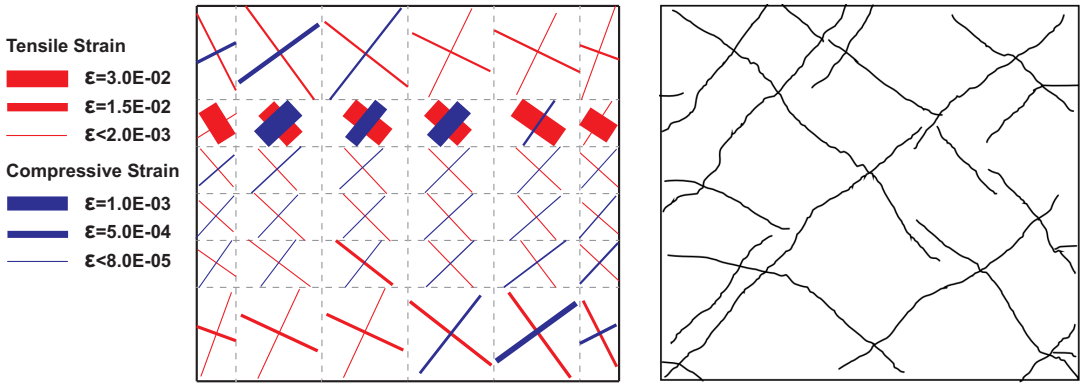

(a) Analytical cracking pattern.

(b) Experimental cracking pattern (Massone, 2006).

Figure 4.68: Analytical and experimental cracking patterns for specimen WP-T5-N0-S1 at 0.8% drift.

4.6.10. Specimen WP-T5-N5-S1

The global response for the squat wall specimen WP-T5-N5-S1 is shown in Figure 4.69, revealing a reasonably accurate prediction of the hysteretic loops. The stiffness is initially overestimated and is reasonably represented for drift levels greater than 0.2%. The lateral load attained at each drift level is slightly overestimated for the major part of the test. The average shear strength (including positive and negative direction) is overestimated by approximately 8%. The model reasonably replicates the initiation of load capacity degradation for both directions. The analytically predicted load capacity degradation was initiated by large shear strains, causing concrete crushing and yielding of the horizontal reinforcement, indicating a diagonal tension failure, as occurred in the experimental test. The top flexural and shear deformation responses are presented in Figure 4.70. The model underestimates the flexural component at each drift level, whereas shear contribution is reasonably captured. Figure 4.71 reveals that the analytical model developed principally shear cracks over the entire wall, with a marginal contribution of flexure toward bottom boundaries, similar to the experimentally observed cracking pattern.

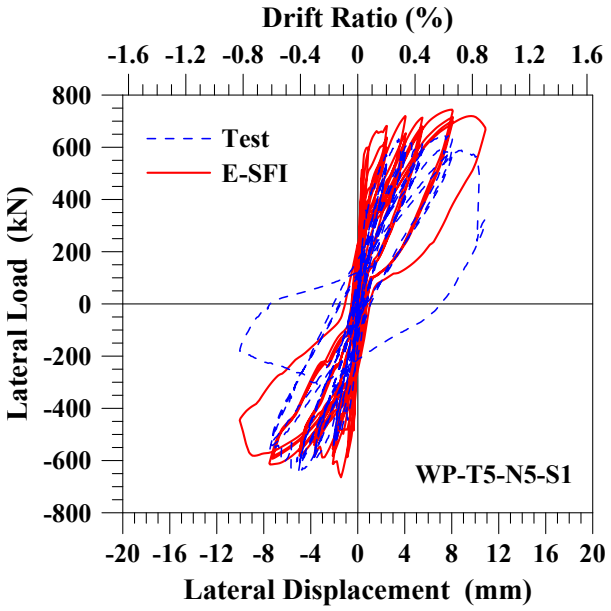

Figure 4.69: Lateral load vs. top displacement response for specimen WP-T5-N5-S1.

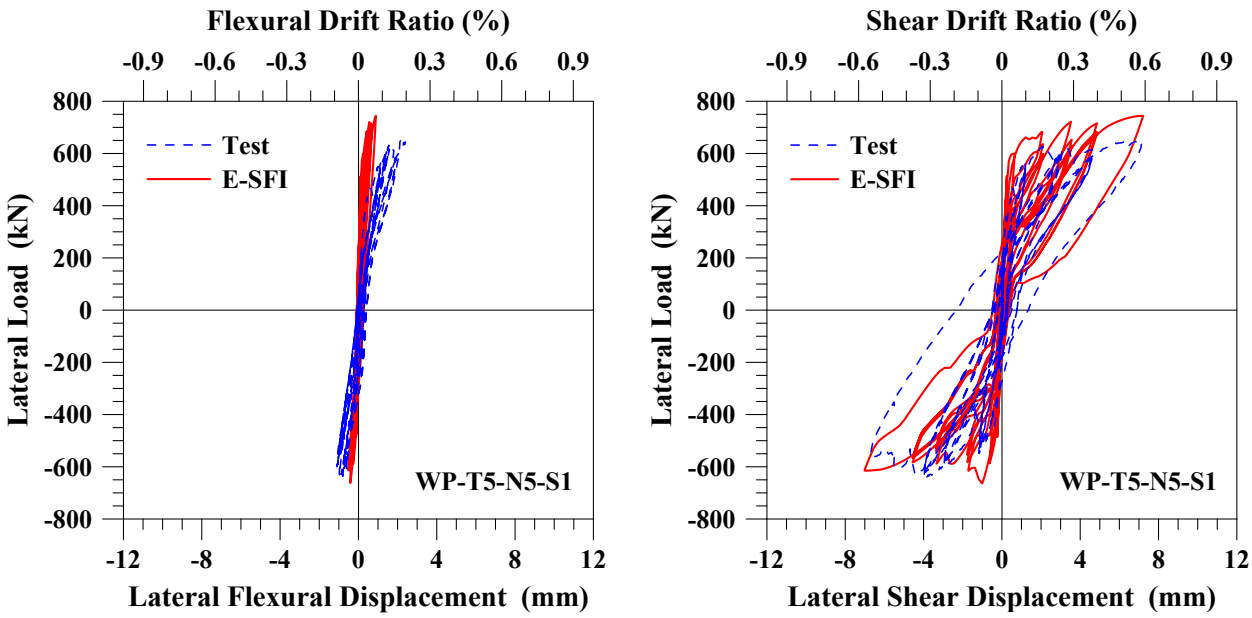

(a) Flexural response.

(b) Shear response.

Figure 4.70: First story lateral load vs. flexural and shear displacement responses for specimen WP-T5-N5-S1.

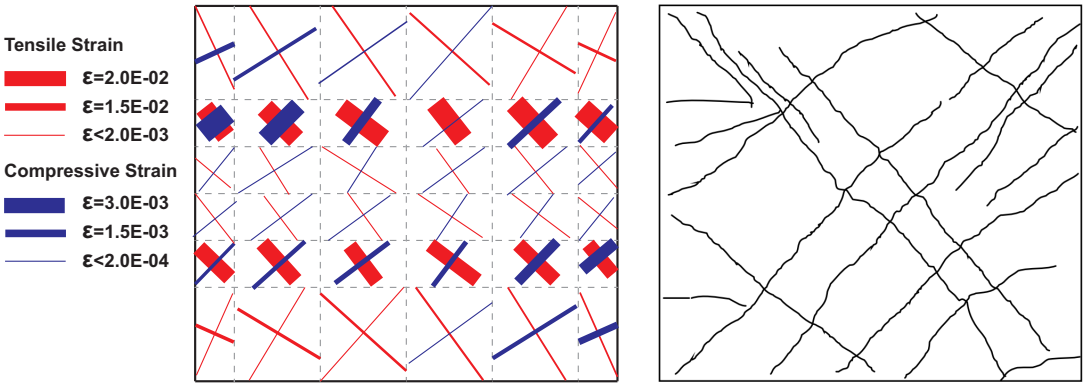

(a) Analytical cracking pattern.

(b) Experimental cracking pattern (Massone, 2006).

Figure 4.71: Analytical and experimental cracking patterns for specimen WP-T5-N5-S1 at 0.8% drift.

4.6.11. Horizontal normal strain profiles

As mentioned by Massone et al. (2009), the average horizontal normal strain distribution accurately correlates the model prediction with the experimentally measured response at global and local level; thus, as shown in Figure 4.72, the experimentally measured and analytically predicted average horizontal strain profiles were plotted at different drift levels (δ) for specimens RW-A15-P10-S78 and SW-T2-S3-4 to study the model effectiveness. The results indicate that although the horizontal expansion predicted by the model does not perfectly match with those values experimentally measured, the prediction of the horizontal expansion is in reasonably agreement, strengthening the proposed calibration at panel level.

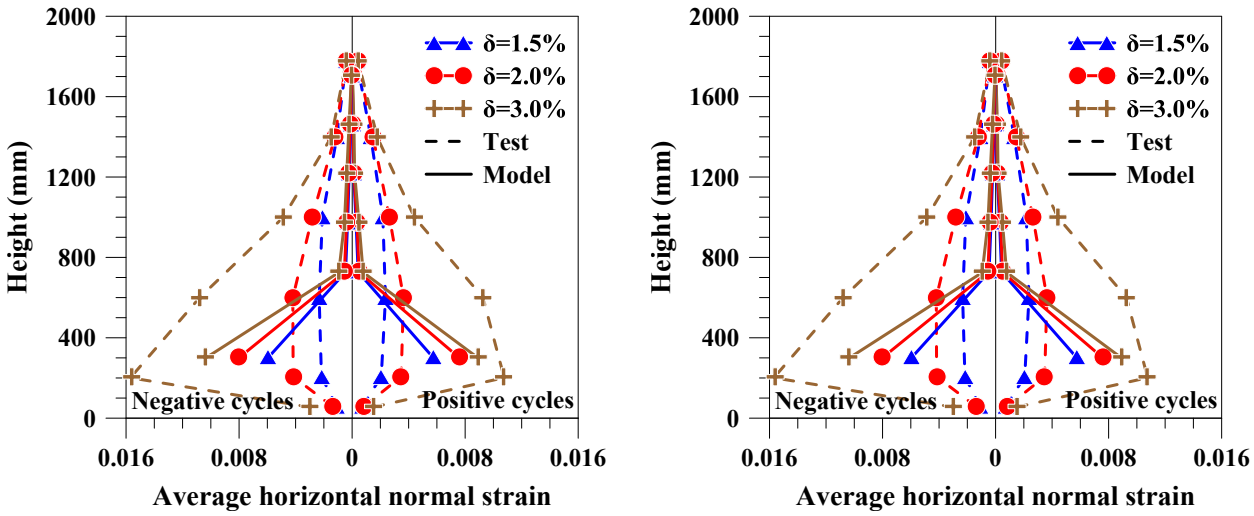

(a) RW-A15-P10-S78 (b) SW-T2-S3-4

Figure 4.72: Average horizontal normal strain profiles.

4.6.12. Cyclic response comparison summary

To quantify the difference between analytical and experimental responses, a comparison between the average (including positive and negative directions) maximum attained shear strength (V_{max}), average maximum flexural response ($u_{f,max}$), average maximum shear response ($u_{sh,max}$), and energy dissipated (E_D), was developed for the ten selected RC wall specimens. The ratio between the model prediction and the experimentally measured response for the aforementioned metrics is presented in Table 4.5, indicating that the E-SFI model, with a reasonable level of accuracy, captures the wall response at both global and local levels. To improve the correlation between model predictions and experimental results, a rotational spring at the wall-end interfaces can be incorporated into the model to account for the extension of the longitudinal reinforcing bars within the pedestals. This effect is specially important for squat walls, where the flexural contribution of the extension of the longitudinal bar within the pedestal (foundation) is relevant, as observed by Massone et al. (2009).

Table 4.5: Cyclic response comparison summary

Specimen ID	$\frac{V_{max,model}}{V_{max,test}}$	$\frac{u_{f,max,model}}{u_{f,max,test}}$	$\frac{u_{sh,max,model}}{u_{sh,max,test}}$	$\frac{E_{D,model}}{E_{D,test}}$
RW2	1.00	0.93	0.57	1.07
RW-A20-P10-S38	0.98	1.05	0.81	1.15
RW-A20-P10-S63	1.09	1.00	0.98	1.17
RW-A15-P10-S51	1.14	1.08	0.86	1.15
RW-A15-P10-S78	1.18	1.22	0.81	1.24
SW-T2-S3-4	0.88	0.76	1.07	0.75
SW-T4-S1-6	0.93	0.40	1.24	1.11
SW-T6-S1-8	0.89	0.57	1.44	1.05
WP-T5-N0-S1	1.00	0.34	1.08	0.74
WP-T5-N5-S1	1.08	0.40	1.03	1.11
Average	1.02	0.78	0.99	1.05
CV	0.10	0.42	0.25	0.16

4.7. Model Efficiency Benchmarking

A benchmarking between the E-SFI, SFI-MVLEM, and MVLEM models was developed to study the efficiency of the novel model in terms of elapsed time and current tangent convergence rate for the specimens RW2, RW-A15-P10-S78, and SW-T2-S3-4, using a standardized displacement-controlled iterative solution strategy. The iterative procedure uses a unique displacement increment step value (D_{incr}) and a norm displacement increment test $|\Delta U|$ to determine if convergence has been reached. The implemented solution strategy starts with the Newton-Raphson algorithm with a maximum value of 500 iterations to achieve a tolerance of $|\Delta U| < 10^{-4}$ mm. If the convergence test is not reached, the maximum number of iterations is increased to 1000, the tolerance is increased to $|\Delta U| < 10^{-3}$ mm, and several algorithms are used to solve the nonlinear problem, including Newton-Raphson with initial tangent and Krylov-Newton (Scott et al., 2010) algorithms. The simulations were conducted on a computer with an Intel Core i7-8700 CPU @ 3192MHz; 2x16GB @ 2400MHz memory RAM DDR4; 1Tb 7200RPM 6.0Gb/s HDD; running on Microsoft Windows 10 Pro version. The benchmarking results are summarized in Table 4.6, whereas the predicted global responses are shown in Figure 4.73. The analysis reveals an increase in the current tangent convergence rate and a reduction of the runtime of the E-SFI model in contrast to the SFI-MVLEM model for all cases, which is related to the reduction in the degrees of freedom. On the other hand, the E-SFI model has shown to be slower than the MVLEM model with a similar current tangent convergence rate, which is related to the use of the panel element in the E-SFI element. The RC panel element duplicates the number of uniaxial concrete elements (two-struts) compared to using a simple uniaxial element per fiber, as well as incorporates the compression softening effect in concrete, tension stiffening effect on concrete and steel, and biaxial damage on concrete. As shown in Figure 4.73(a), all models have a similar predicted response for the slender wall RW2 with accurate results. Figure 4.73(b) reveals that for the mid-rise wall RW-A15-P10-S78, the hysteretic loops are similar in the shear-flexure models, which are in concordance with the experimental results, whereas the flexural model shows a less pinched behavior. For the squat wall SW-T2-S3-4, the results presented in Figure 4.73(c) reveals that the flexural model highly overestimates the capacity and ductility of the wall, whereas the shear-flexure models are in more concordance with experimental results.

Table 4.6: Model Efficiency benchmarking results

Specimen ID	Model	Dincr (mm)	No. of Analysis Steps	Current Tangent Convergence Rate (%)	Runtime (mm:ss)
RW2	E-SFI	0.25	4104	99.1	00:43
	SFI-MVLEM	0.25	4104	73.2	02:27
	MVLEM	0.25	4104	99.8	00:13
RW-A15-P10-S78	E-SFI	0.25	2756	99.4	01:10
	SFI-MVLEM	0.25	2756	13.1	06:37
	MVLEM	0.25	2756	100.0	00:07
SW-T2-S3-4	E-SFI	0.10	4200	99.9	02:47
	SFI-MVLEM	0.10	4200	3.0	11:29
	MVLEM	0.10	4200	99.9	00:11

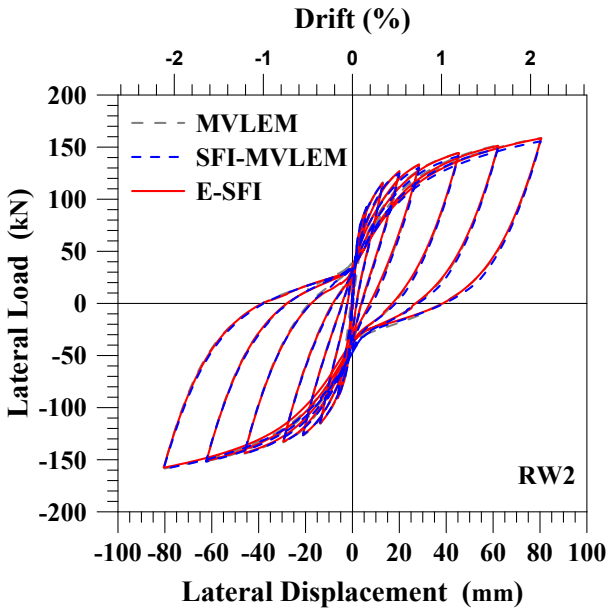

(a) RW2

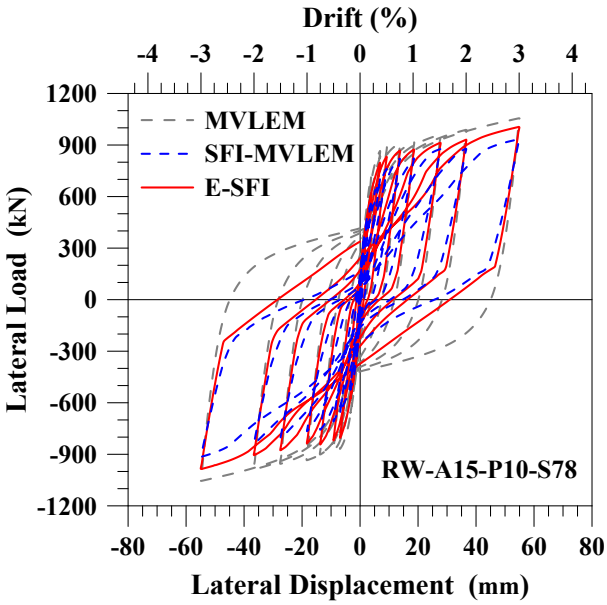

(b) RW-A15-P10-S78

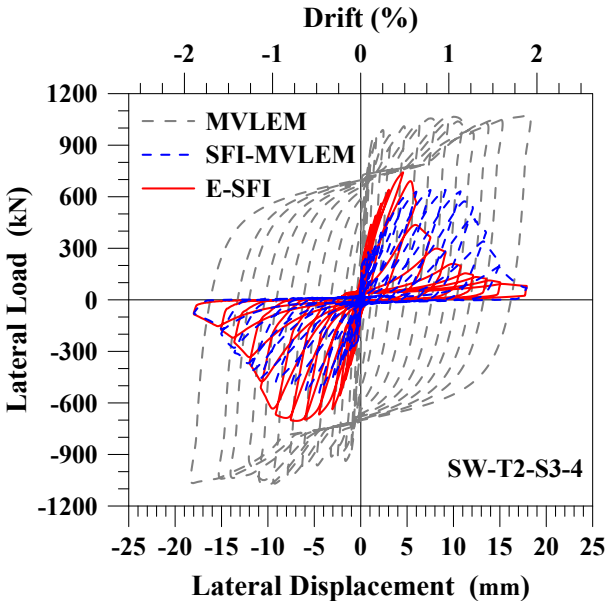

(c) SW-T2-S3-4

Figure 4.73: Predicted global response comparison.

Chapter 5

Summary and Conclusions

A novel macroscopic element named Efficient-Shear-Flexure-Interaction (E-SFI) was developed for simulating the nonlinear response of RC walls subjected to reversed cyclic loading conditions. The element formulation, based on the Shear-Flexure Interaction Multiple-Vertical-Line-Element-Model (SFI-MVLEM), replaces the uniaxial vertical springs of the Multiple-Vertical-Line-Element-Model (MVLEM) formulation by two-dimensional RC panel elements (macro-fibers) to capture the interaction between shear, axial and flexural behaviors. The vertical normal and shear strains at each macro-fiber are computed based on the element degrees of freedom, together with the assumptions of plane sections remain plane and constant shear strain across the section. In this approach, the horizontal normal strain at each macro-fiber is computed using a calibrated expression in terms of the shear strain and the horizontal reinforcement ratio at panel level. Therefore, no additional degrees of freedom nor iterative procedures are incorporated into the original MVLEM formulation. The adopted constitutive RC panel behavior is described by the Fixed-Strut-Angle-Model (FSAM), in which the principal strain and stress directions are set coincidentally with parallel and perpendicular directions to the first crack orientation. Simple shear stress transfer mechanisms across cracks are incorporated into the RC panel formulation, including shear aggregate interlock and dowel action models. Uniaxial cyclic stress-strain relationships are used to represent the behavior of concrete and steel. Furthermore, the effects of compression softening in concrete, tension stiffening effect on concrete and steel, and biaxial damage on concrete, are also incorporated into the RC panel formulation.

Shear resisting parameters were calibrated based on comparisons with experimental test results, suggesting a value of $\eta = 0.35$ for the shear aggregate interlock model, and a value of $\alpha = 0.0001$ for squat walls and $\alpha = 0.005$ for medium-rise and slender walls for the dowel action model. Also, a modeling methodology was proposed based on adjusting the end elements' height by the plastic hinge length, as well as the use of at least six wall elements over the height and six RC panels across wall length to have an accurate distribution of strains in the wall model.

The shear strength predicted by the model was contrasted with a database of 252 RC wall specimen tests reported in the literature. The average ratio of the predicted over the experimentally measured shear strength (V_{model}/V_{test}) for all cases was 1.04 with a coefficient of variation of 0.23, indicating an accurate prediction of the model with a relatively small dispersion. Furthermore, a sensitivity analysis was developed for variation in wall parameters

based on a linear trend estimation of the database specimens. The model has shown a little dependence to the horizontal and vertical web reinforcement, and shear span-to-depth ratio, with a variation of less than 20% over the whole range; a relatively small dependence to the longitudinal boundary reinforcement, concrete compressive strength, cross-sectional shape, and boundary condition, with a variation of less than 10% over the whole range; and a variation to the axial load of 30% over the whole range. Indicating that the E-SFI model accurately captures the physical dependence of the response to wall parameters.

The analytically-predicted hysteretic response was validated against ten well-instrumented RC wall specimen tests reported in the literature. The selected wall specimens cover a wide range of wall characteristics and responses, with a shear span-to-depth ratio ranging from 0.44 to 3.0, tested under single and double curvature conditions. Model results have shown an accurate prediction of the hysteretic loops, stiffness, and load capacity at each drift level. The predicted shear and flexural contributions to the global response are generally in agreement with experimental results, as well as the cracking pattern. The model was capable of capturing degradation mechanisms associated with diagonal tension and compression failure. Initiation of degradation in specimens that presented rebar buckling, shear sliding, and lateral instability was not captured since the model did not incorporate such failure modes. Furthermore, a benchmarking was developed by contrasting the runtime and current tangent convergence ratio for three wall specimens using the E-SFI, SFI-MVLEM, and MVLEM models, revealing a considerable improvement of the efficiency of the E-SFI model compared to the SFI-MVLEM model.

Based on the presented research, it was proven that the E-SFI model, with a simple and efficient macroscopic formulation, accurately captures the shear-flexure interaction phenomenon from squat to slender RC walls, reinforcing the effectiveness of the horizontal normal strain calibration used in the E-SFI model. Futures studies can be focus on the validation of the model in other structural elements, as well as an extension of the formulation to include out-of-plane behavior.

Bibliography

ACI Committee 318. 2019. *318-19 Building Code Requirements for Structural Concrete and Commentary*. American Concrete Institute.

Antebi, J., Utku, S., & Hansen, R. J. 1960. *The response of shear walls to dynamic loads*. Department of Civil and Sanitary Engineering, Massachusetts Institute of Technology.

Arteta, C. A. 2015. *Seismic Response Assessment of Thin Boundary Elements of Special Concrete Shear Walls*. Ph.D. Dissertation, Department of Civil and Environmental Engineering, University of California, Berkeley.

Barda, F., Hanson, J. M., & Corley, W. G. 1977. Shear strength of low-rise walls with boundary elements. *ACI Symposium Publication*, *SP-53*.

Belarbi, A., & Hsu, T. C. 1994. Constitutive Laws of Concrete in Tension and Reinforcing Bars Stiffened By Concrete. *ACI Structural Journal*, *91*(4), 465–474.

Belarbi, A., & Hsu, T. C. 1995. Constitutive Laws of Softened Concrete in Biaxial Tension Compression. *ACI Structural Journal*, *92*(5).

Belytschko, T., Lin, J. I., & Chen-Shyh, T. 1984. Explicit algorithms for the nonlinear dynamics of shells. *Computer methods in applied mechanics and engineering*, *42*(2), 225–251.

Benjamin, J. R., & Williams, H. A. 1957. The Behavior of One-Story Reinforced Concrete Shear Walls. *Journal of the Structural Division*, *83*(3), 1–49.

Bentz, E. C. 2005. Explaining the Riddle of Tension Stiffening Models for Shear Panel Experiments. *Journal of Structural Engineering*, *131*(9), 1422–1425.

Calabrese, A., Almeida, J. P., & Pinho, R. 2010. Numerical Issues in Distributed Inelasticity Modeling of RC Frame Elements for Seismic Analysis. *Journal of Earthquake Engineering*, *14*(sup1), 38–68.

Cardenas, A. E., Corley, W. G., & Russell, H. G. 1980. Strength of Low-Rise Structural Walls. *ACI Symposium Publication*, *63*, 221–242.

Chang, G. A., & Mander, J. B. 1994. *Seismic Energy Based Fatigue Damage Analysis of Bridge Columns: Part 1 - Evaluation of Seismic Capacity*. Technical Report No. NCEER-94-0006, National Center for Earthquake Engineering Research (NCEER), State University of New York, Buffalo.

Diana, T. 2011. *Finite Element Analysis User's Manual-Release 9.4. 4*. TNO DIANA.

Elmorsi, M., Kianush, M., & Tso, W. 1998. Nonlinear Analysis of Cyclically Loaded Reinforced Concrete Structures. *ACI Structural Journal*, *95*(6).

Filippou, F. C., Popov, E. P., & Bertero, V. V. 1983. *Effects of Bond Deterioration on Hysteretic Behaviour of Reinforced Concrete Joints.* EERC Report No. UCB/EERC-83/19, Earthquake Engineering Research Center, University of California, Berkeley, California.

Galletly, G. D. 1952. *Behavior of reinforced concrete shear walls under static load.* Department of Civil and Sanitary Engineering, Massachusetts Institute of Technology.

Gullu, M. F., & Orakcal, K. 2019. Nonlinear Finite Element Modeling of Reinforced Concrete Walls with Varying Aspect Ratios. *Journal of Earthquake Engineering*, 1–32.

Hidalgo, P. A., Ledezma, C. A., & Jordan, R. M. 2002. Seismic Behavior of Squat Reinforced Concrete Shear Walls. *Earthquake Spectra*, *18*(2), 287–308.

Hirosawa, M. 1975. *Past Experimental Results on Reinforced Concrete Shear Walls and Analysis on Them.*

Kolozvari, K., Arteta, C., Fischinger, M., Gavridou, S., Hube, M., Isaković, T., ... Wallace, J. 2018. Comparative Study of State-of-the-Art Macroscopic Models for Planar Reinforced Concrete Walls. *ACI Structural Journal*, *115*(6).

Kolozvari, K., Biscombe, L., Dashti, F., Dhakal, R. P., Gogus, A., Gullu, M. F., ... Wallace, J. 2019. State-of-the-art in nonlinear finite element modeling of isolated planar reinforced concrete walls. *Engineering Structures*, *194*, 46–65.

Kolozvari, K., Kalbasi, K., Orakcal, K., Massone, L. M., & Wallace, J. 2019. Shear–flexure-interaction models for planar and flanged reinforced concrete walls. *Bulletin of Earthquake Engineering*, *17*(12), 6391–6417.

Kolozvari, K., Orakcal, K., & Wallace, J. W. 2015. Modeling of Cyclic Shear-Flexure Interaction in Reinforced Concrete Structural Walls. I: Theory. *Journal of Structural Engineering*, *141*(5), 04014135.

Kolozvari, K., Tran, T. A., Orakcal, K., & Wallace, J. W. 2015. Modeling of Cyclic Shear-Flexure Interaction in Reinforced Concrete Structural Walls. II: Experimental Validation. *Journal of Structural Engineering*, *141*(5), 04014136.

Lu, Y., & Panagiotou, M. 2014. Three-Dimensional Cyclic Beam-Truss Model for Nonplanar Reinforced Concrete Walls. *Journal of Structural Engineering*, *140*(3), 04013071.

Mander, J. B., Priestley, M. J. N., & Park, R. 1988. Theoretical Stress-Strain Model for Confined Concrete. *Journal of Structural Engineering*, *114*(8), 1804–1826.

Mansour, M., & Hsu, T. T. C. 2005. Behavior of Reinforced Concrete Elements under Cyclic Shear. II: Theoretical Model. *Journal of Structural Engineering*, *131*(1), 54–65.

Mansour, M. Y., Hsu, T. T. C., & Lee, J. Y. 2002. Pinching Effect in Hysteretic loops of R/C Shear Elements. *ACI Symposium Publication*, *205*, 293–322.

Massone, L. M. 2006. *RC Wall Shear - Flexure Interaction: Analytical and Experimental Responses*. Ph.D. Dissertation, Department of Civil and Environmental Engineering, University of California, Los Angeles.

Massone, L. M. 2010. Strength prediction of squat structural walls via calibration of a shear–flexure interaction model. *Engineering Structures*, *32*(4), 922–932.

Massone, L. M., López, C. N., & Kolozvari, K. 2020. Efficient Shear-Flexure Interaction Model for Reinforced Concrete Walls. *Proceedings, 17th World Conference on Earthquake Engineering, Sendai, Japan*, 11.

Massone, L. M., Orakcal, K., & Wallace, J. W. 2006. Shear-Flexure Interaction for Structural Walls. *ACI Symposium Papers*, *SP-236*, 127–150.

Massone, L. M., & Wallace, J. W. 2004. Load - Deformation Responses of Slender Reinforced Concrete Walls. *ACI Structural Journal*, *101*(1), 103–113.

Massone, L. M., Wallace, J. W., & Orakcal, K. 2009. Modeling of squat structural walls controlled by shear. *ACI Structural Journal*, *106*(5), 646–655.

McKenna, F., Scott, M. H., & Fenves, G. L. 2010. Nonlinear Finite-Element Analysis Software Architecture Using Object Composition. *Journal of Computing in Civil Engineering*, *24*(1), 95–107.

Menegotto, M., & Pinto, E. 1973. Method of analysis of cyclically loaded RC plane frames including changes in geometry and non-elastic behavior of elements under normal force and bending. *Proceedings, IABSE Symposium, Lisbon, Portugal*, 15–22.

Mohammadi-Doostdar, H., & Saatcioglu, M. 2002. *Behavior and Design of Earthquake Resistant Low-Rise Shear Walls*. Report OCCERC 02-28. Ottawa Carleton Earthquake Engineering Research Center. Department of Civil Engineering, University of Ottawa, Canada.

Oesterle, R. G., Fiorato, A. E., Johal, L. S., Carpenter, J. E., & Russell, H. G. 1976. Earthquake resistant structural walls - tests of isolated walls. *Portland Cement Association, Skokie, IL*(October), 315.

Oesterle, R. G., Fiorato, A. E., Johal, L. S., Carpenter, J. E., Russell, H. G., & Corley, W. G. 1979. Earthquake resistant structural walls - tests of isolated walls. phase II. *Portland Cement Association, Skokie, IL*, 327.

Orakcal, K., Massone, L. M., & Ulugtekin, D. 2019. A Hysteretic Constitutive Model for Reinforced Concrete Panel Elements. *International Journal of Concrete Structures and Materials*, *13*(1), 51.

Orakcal, K., & Wallace, J. W. 2006. Flexural Modeling of Reinforced Concrete Walls - Experimental Verification. *ACI Materials Journal*, *103*(2), 196–206.

Orakcal, K., Wallace, J. W., & Conte, J. P. 2004. Flexural Modeling of Reinforced Concrete Walls - Model Attributes. *ACI Structural Journal*, *101*(5), 688–698.

Pang, X. B., & Hsu, T. T. 1995. Behavior of Reinforced Concrete Membrane Elements in Shear. *ACI Structural Journal*, *92*(6), 665–679.

Petrangeli, M., Pinto, P. E., & Ciampi, V. 1999. Fiber Element for Cyclic Bending and Shear of RC Structures. I: Theory. *Journal of Engineering Mechanics*, *125*(9), 994–1001.

Rojas, F., Anderson, J., & Massone, L. 2016. A nonlinear quadrilateral layered membrane element with drilling degrees of freedom for the modeling of reinforced concrete walls. *Engineering Structures*, *124*, 521–538.

Saatcioglu, M., & Razvi, S. R. 1992. Strength and Ductility of Confined Concrete. *Journal of Structural Engineering*, *118*(6), 1590–1607.

Sayre, B. L. 2003. *Performance Evaluation of Steel Reinforced Concrete Shear Walls*. MS Thesis, Department of Civil and Environmental Engineering, University of California, Los Angeles.

Scott, M. H., & Fenves, G. L. 2010. Krylov Subspace Accelerated Newton Algorithm: Application to Dynamic Progressive Collapse Simulation of Frames. *Journal of Structural Engineering*, *136*(5), 473–480.

Stevens, N. J. 1987. *Analytical modeling of reinforced concrete subjected to monotonic and reversed loadings*. Ph.D. Dissertation, Department of Civil Engineering, Univeristy of Toronto, Canada.

Terzioglu, T. 2011. *Experimental evaluation of the lateral load behavior of squat structural walls*. M.S. Thesis, Department of Civil Engineering, Bogazici University, Istanbul, Turkey.

Terzioglu, T., Orakcal, K., & Massone, L. M. 2018. Cyclic lateral load behavior of squat reinforced concrete walls. *Engineering Structures*, *160*, 147–160.

Thomsen, J. H., & Wallace, J. W. 2004. Displacement-Based Design of Slender Reinforced Concrete Structural Walls—Experimental Verification. *Journal of Structural Engineering*, *130*(4), 618–630.

Tran, T. A. 2012. *Experimental and Analytical Studies of Moderate Aspect Ratio Reinforced Concrete Structural Walls*. Ph.D. Dissertation, Department of Civil and Environmental Engineering, University of California, Los Angeles.

Tran, T. A., & Wallace, J. W. 2012. Experimental Study of Nonlinear Flexural and Shear Deformations of Reinforced Concrete Structural Walls. *Proceedings, 15th World Conference on Earthquake Engineering, Lisbon, Portugal.*.

Tsai, W. T. 1988. Uniaxial Compressional Stress-Strain Relation of Concrete. *Journal of Structural Engineering*, *114*(9), 2133–2136.

Vásquez, J. A., de la Llera, J. C., & Hube, M. A. 2016. A regularized fiber element model for reinforced concrete shear walls. *Earthquake Engineering & Structural Dynamics*, *45*(13), 2063–2083.

Vecchio, F. J., & Collins, M. P. 1986. The Modifed Compression-Field Theory for Reinforced Concrete Elements Subjected to Shear. *Journal of the American Concrete Institute*, *83*(2), 219–231.

Vecchio, F. J., & Collins, M. P. 1993. Compression Response of Cracked Reinforced Concrete. *Journal of Structural Engineering*, *119*(12), 3590–3610.

Vulcano, A., Bertero, V. V., & Colotti, V. 1988. Analytical Modeling of RC Structural Walls. *Proceedings, 9th World Conference on Earthquake Engineering, Tokyo-Kyoto, Japan*, *6*, 41–46.

Wallace, J. W. 1994. New Methodology for Seismic Design of RC Shear Walls. *Journal of Structural Engineering*, *120*(3), 863–884.

Wallace, J. W. 1995. Seismic Design of RC Structural Walls. Part I: New Code Format. *Journal of Structural Engineering*, *121*(1), 75–87.

Wong, P. S., Vecchio, F. J., & Trommels, H. 2013. *Vector2 & Formworks user's manual second edition*. University of Toronto, Canada.

Yamada, M., Katagihara, K., & Kawamura, H. 1974. Reinforced Concrete Shear Walls Without Openings; Test and Analysis. *ACI Symposium Publication*, *SP-42*, 539–558.

Appendix A

Shear strength test database

Table A.1: Shear strength test database.

No.	Author	h_w (mm)	l_w (mm)	t_w (mm)	l_{be} (mm)	t_{be} (mm)	f'_c (MPa)	$\rho_{v,web}$ (%)	$f_{yv,web}$ (MPa)	$\rho_{h,web}$ (%)	$f_{yh,web}$ (MPa)	ρ_{bound} (%)	$f_{y,bound}$ (MPa)	P_{axial} (N)	V_{test} (N)	Curvature Condition
1	Endo	750.0	2250.0	80.0	250.0	250.0	26.0	0.493	623.7	0.474	623.7	0.811	358.9	369720	654104	single
2	Endo	750.0	2250.0	80.0	250.0	250.0	24.6	0.160	623.7	0.135	623.7	0.811	358.9	367524	558979	single
3	Endo	750.0	2250.0	80.0	250.0	250.0	26.0	0.160	623.7	0.135	623.7	0.811	358.9	369720	524656	single
4	Endo	750.0	2250.0	50.0	250.0	250.0	24.6	0.255	623.7	0.217	623.7	0.811	358.9	368078	466797	single
5	Endo	750.0	2250.0	50.0	250.0	250.0	26.0	0.789	623.7	0.758	623.7	0.811	358.9	368550	783551	single
6	Hirosawa	625.0	600.0	30.0	100.0	100.0	23.5	0.231	293.2	0.213	293.2	2.512	208.9	0	49033	single
7	Hirosawa	625.0	600.0	30.0	100.0	100.0	27.2	0.231	293.2	0.213	293.2	2.512	208.9	29376	66195	single
8	Hirosawa	625.0	600.0	30.0	100.0	100.0	26.9	0.231	293.2	0.213	293.2	2.512	208.9	62946	76002	single
9	Hirosawa	625.0	600.0	30.0	100.0	100.0	25.7	0.231	293.2	0.213	293.2	2.512	208.9	125365	86299	single
10	Hirosawa	575.0	600.0	30.0	100.0	100.0	18.6	0.238	261.8	0.239	261.8	2.524	212.8	0	34323	single
11	Hirosawa	575.0	600.0	30.0	100.0	100.0	18.6	0.238	261.8	0.240	261.8	2.524	212.8	0	36775	single
12	Hirosawa	625.0	600.0	30.0	100.0	100.0	29.9	0.231	293.2	0.213	293.2	2.524	208.9	62969	58840	single

13	Hirosawa	625.0	600.0	30.0	100.0	150.0	25.2	0.209	475.6	0.201	475.6	2.719	276.2	0	72569	single
14	Hirosawa	625.0	600.0	30.0	100.0	150.0	28.3	0.209	475.6	0.201	475.6	2.612	221.1	41261	68647	single
15	Hirosawa	625.0	600.0	30.0	100.0	150.0	28.0	0.209	475.6	0.201	475.6	2.612	221.1	82152	78453	single
16	Hirosawa	625.0	600.0	30.0	100.0	150.0	29.0	0.209	475.6	0.201	475.6	2.612	221.1	123714	101989	single
17	Ryo	1200.0	2300.0	75.0	250.0	250.0	23.2	0.188	335.4	0.188	335.4	2.550	467.8	0	965955	single
18	Ryo	1200.0	2300.0	80.0	250.0	250.0	33.0	0.177	335.4	0.177	335.4	2.550	467.8	0	931632	single
19	Ryo	1200.0	1550.0	80.0	250.0	250.0	17.4	0.168	485.4	0.177	485.4	2.550	467.8	0	608012	single
20	Kokusho	150.0	430.0	30.0	30.0	150.0	22.5	0.000	0.0	0.000	0.0	0.680	382.5	0	24909	single
21	Kokusho	150.0	430.0	30.0	30.0	150.0	22.5	0.360	382.5	0.411	382.5	0.680	382.5	0	20692	single
22	Kokusho	150.0	430.0	30.0	30.0	150.0	16.9	0.360	382.5	0.411	382.5	0.680	382.5	0	17358	single
23	Kokusho	150.0	430.0	30.0	30.0	150.0	16.9	0.368	333.4	0.418	333.4	0.680	382.5	0	19123	single
24	Kokusho	150.0	430.0	30.0	30.0	150.0	16.9	0.360	382.5	0.411	382.5	0.680	382.5	0	22751	single
25	Kokusho	150.0	430.0	30.0	30.0	150.0	16.1	0.360	382.5	0.411	382.5	0.680	382.5	0	19025	single
26	Kokusho	150.0	430.0	30.0	30.0	150.0	16.1	0.360	382.5	0.411	382.5	0.680	382.5	0	20790	single
27	Kokusho	150.0	430.0	25.0	30.0	145.0	26.5	0.432	402.1	0.493	402.1	0.710	402.1	0	28439	single
28	Kokusho	150.0	430.0	23.0	30.0	145.0	17.9	0.470	402.1	0.536	402.1	0.710	402.1	0	24517	single
29	Kokusho	150.0	430.0	25.0	30.0	145.0	17.9	0.441	323.6	0.501	323.6	0.710	402.1	0	25988	single
30	Kokusho	150.0	430.0	20.0	30.0	145.0	15.4	0.551	323.6	0.627	323.6	0.710	402.1	0	25988	single
31	Kokusho	150.0	430.0	23.0	30.0	145.0	19.9	0.702	323.6	0.728	323.6	0.710	402.1	0	29420	single
32	Kokusho	150.0	430.0	24.0	30.0	145.0	18.6	0.672	323.6	0.697	323.6	0.710	402.1	0	27459	single
33	Kokusho	355.0	430.0	23.0	30.0	145.0	14.2	0.000	0.0	0.000	0.0	1.520	407.3	0	18142	single
34	Kokusho	355.0	430.0	24.0	30.0	145.0	14.2	0.000	0.0	0.000	0.0	1.520	407.3	0	16377	single
35	Kokusho	355.0	430.0	27.0	30.0	145.0	14.2	0.400	402.1	0.385	402.1	1.520	407.3	0	24517	single
36	Kokusho	355.0	430.0	24.0	30.0	145.0	14.2	0.450	323.6	0.433	323.6	1.520	407.3	0	23536	single
37	Kokusho	355.0	430.0	22.0	30.0	145.0	16.2	0.501	323.6	0.483	323.6	1.520	407.3	0	20006	single

38	Kokusho	355.0	430.0	16.0	30.0	145.0	13.8	0.689	323.6	0.664	323.6	1.520	407.3	0	19123	single
39	Kokusho	355.0	430.0	22.0	30.0	145.0	17.9	0.733	323.6	0.723	323.6	1.520	407.3	0	24713	single
40	Kokusho	355.0	430.0	22.0	30.0	145.0	16.8	0.733	323.6	0.723	323.6	1.520	407.3	0	25890	single
41	Kokusho	200.0	420.0	20.0	60.0	60.0	13.7	0.000	0.0	0.000	0.0	1.790	342.8	0	36677	single
42	Kokusho	200.0	420.0	20.0	60.0	60.0	13.7	0.523	323.6	0.523	323.6	1.790	342.8	0	48739	single
43	Kokusho	200.0	420.0	20.0	60.0	60.0	19.1	0.000	0.0	0.000	0.0	3.180	334.5	0	37265	single
44	Kokusho	200.0	420.0	20.0	60.0	60.0	18.0	0.000	0.0	0.000	0.0	3.180	334.5	0	37461	single
45	Kokusho	200.0	420.0	20.0	60.0	60.0	19.1	0.523	323.6	0.523	323.6	3.180	334.5	0	43149	single
46	Kokusho	200.0	420.0	20.0	60.0	60.0	18.0	0.523	323.6	0.523	323.6	3.180	334.5	0	48445	single
47	Kokusho	200.0	420.0	20.0	60.0	60.0	16.7	0.000	0.0	0.000	0.0	4.620	294.2	0	35304	single
48	Kokusho	200.0	420.0	20.0	60.0	60.0	15.2	0.000	0.0	0.000	0.0	4.620	294.2	0	34323	single
49	Kokusho	200.0	420.0	20.0	60.0	60.0	15.2	0.000	0.0	0.000	0.0	4.620	294.2	0	32362	single
50	Kokusho	200.0	420.0	20.0	60.0	60.0	29.4	0.257	372.7	0.258	372.7	3.080	294.2	0	45111	single
51	Sugano	1200.0	2300.0	74.0	250.0	250.0	24.1	0.184	549.2	0.184	549.2	2.540	418.7	0	833565	single
52	Sugano	1200.0	2300.0	83.0	250.0	250.0	25.2	0.074	460.9	0.074	460.9	2.540	418.7	0	804145	single
53	Hirosawa	1600.0	1700.0	160.0	170.0	160.0	17.3	0.505	407.0	0.263	419.2	5.680	418.7	0	809049	single
54	Hirosawa	1600.0	1700.0	160.0	170.0	160.0	20.8	0.505	407.0	0.263	419.2	5.680	376.6	531814	725692	single
55	Hirosawa	1600.0	1700.0	160.0	170.0	160.0	20.8	0.505	407.0	0.568	421.6	5.680	376.6	531814	813952	single
56	Hirosawa	1600.0	1700.0	160.0	170.0	160.0	13.7	0.505	407.0	0.568	421.6	5.680	376.6	532875	813952	single
57	Hirosawa	1600.0	1700.0	160.0	170.0	160.0	14.7	0.505	407.0	1.083	415.2	5.680	376.6	531787	804145	single
58	Hirosawa	1600.0	1700.0	160.0	170.0	160.0	18.3	0.505	407.0	1.083	415.2	5.680	376.6	532603	912018	single
59	Hirosawa	1600.0	1700.0	160.0	170.0	160.0	20.8	0.505	407.0	0.611	420.7	2.510	382.3	531814	686466	single
60	Hirosawa	1600.0	1700.0	160.0	170.0	160.0	13.7	0.505	407.0	0.611	420.7	2.510	382.3	532875	617819	single
61	Hirosawa	1600.0	1700.0	160.0	170.0	160.0	14.7	0.505	407.0	1.083	415.2	2.510	382.3	531787	706079	single
62	Hirosawa	1600.0	1700.0	160.0	170.0	160.0	18.3	0.505	407.0	1.083	415.2	2.510	382.3	532603	760015	single

63	Hirosawa	1600.0	850.0	160.0	85.0	160.0	20.8	0.404	407.0	0.568	421.6	9.910	380.4	265907	321168	single
64	Hirosawa	1600.0	850.0	160.0	85.0	160.0	17.8	0.404	407.0	0.568	421.6	9.910	380.4	266288	333426	single
65	Hirosawa	1600.0	850.0	160.0	85.0	160.0	17.8	0.404	407.0	1.083	415.2	8.440	377.6	266288	323619	single
66	Hirosawa	1600.0	850.0	160.0	85.0	160.0	23.2	0.404	407.0	1.083	415.2	8.440	377.6	268192	367749	single
67	Tanabe	300.0	420.0	20.0	60.0	40.0	63.4	0.000	0.0	0.000	0.0	7.010	315.8	0	38638	single
68	Tanabe	300.0	420.0	40.0	42.0	40.0	63.4	0.000	0.0	0.000	0.0	10.020	315.8	0	50406	single
69	Tanabe	450.0	570.0	20.0	60.0	60.0	32.1	0.000	0.0	0.000	0.0	4.700	367.7	0	50995	single
70	Tanabe	450.0	570.0	30.0	60.0	60.0	32.2	0.000	0.0	0.000	0.0	4.700	367.7	0	39227	single
71	Tanabe	450.0	570.0	40.0	60.0	60.0	33.3	0.000	0.0	0.000	0.0	4.700	367.7	0	58840	single
72	Tanabe	450.0	570.0	10.0	60.0	60.0	31.9	3.667	284.4	3.667	284.4	4.700	367.7	0	46081	single
73	Tanabe	450.0	570.0	20.0	60.0	60.0	34.3	1.833	284.4	1.833	284.4	4.700	367.7	0	62763	single
74	Tanabe	450.0	570.0	20.0	60.0	60.0	30.1	1.833	284.4	1.833	284.4	4.700	367.7	0	74531	single
75	Tanabe	450.0	570.0	20.0	60.0	60.0	34.9	1.833	284.4	1.833	284.4	4.700	367.7	0	62763	single
76	Tanabe	450.0	570.0	30.0	60.0	60.0	35.6	1.222	284.4	1.222	284.4	4.700	367.7	0	94144	single
77	Tanabe	450.0	570.0	30.0	60.0	60.0	34.3	1.222	284.4	1.222	284.4	4.700	367.7	0	89633	single
78	Tanabe	450.0	570.0	30.0	60.0	60.0	33.8	1.222	284.4	1.222	284.4	4.700	367.7	0	86299	single
79	Tanabe	450.0	570.0	40.0	60.0	60.0	32.9	0.917	284.4	0.917	284.4	4.700	367.7	0	98067	single
80	Tanabe	450.0	570.0	40.0	60.0	60.0	35.3	0.917	284.4	0.917	284.4	4.700	367.7	0	97086	single
81	Tanabe	450.0	570.0	40.0	60.0	60.0	35.8	0.917	284.4	0.917	284.4	4.700	367.7	0	101989	single
82	Tanabe	450.0	570.0	10.0	60.0	60.0	45.8	1.833	294.2	1.833	294.2	4.700	292.7	0	42659	single
83	Tanabe	450.0	570.0	10.0	60.0	60.0	43.4	1.833	294.2	1.833	294.2	4.700	292.7	0	43836	single
84	Tanabe	450.0	570.0	20.0	60.0	60.0	43.0	1.833	294.2	1.833	294.2	4.700	292.7	0	68647	single
85	Tanabe	450.0	570.0	20.0	60.0	60.0	48.7	1.833	294.2	1.833	294.2	4.700	292.7	0	70608	single
86	Tanabe	450.0	570.0	30.0	60.0	60.0	40.0	1.222	294.2	1.222	294.2	4.700	292.7	0	70608	single
87	Tanabe	450.0	570.0	30.0	60.0	60.0	46.1	1.222	294.2	1.222	294.2	4.700	292.7	0	76492	single

88	Tanabe	450.0	570.0	40.0	60.0	60.0	45.3	0.917	294.2	0.917	294.2	4.700	292.7	0	78453	single
89	Tanabe	450.0	570.0	40.0	60.0	60.0	42.6	0.917	294.2	0.917	294.2	4.700	292.7	0	77473	single
90	Tanabe	450.0	570.0	10.0	60.0	60.0	46.3	2.444	294.2	2.444	294.2	4.700	292.7	0	55211	single
91	Tanabe	450.0	570.0	10.0	60.0	60.0	46.9	2.444	294.2	2.444	294.2	4.700	292.7	0	57075	single
92	Tanabe	450.0	570.0	10.0	60.0	60.0	45.6	2.444	294.2	2.444	294.2	4.700	292.7	0	58055	single
93	Tanabe	450.0	570.0	20.0	60.0	60.0	43.7	2.444	323.6	2.444	323.6	4.700	292.7	0	81886	single
94	Tanabe	450.0	570.0	20.0	60.0	60.0	43.9	2.444	323.6	2.444	323.6	4.700	292.7	0	76492	single
95	Tanabe	450.0	570.0	20.0	60.0	60.0	45.1	2.444	323.6	2.444	323.6	4.700	292.7	0	79924	single
96	Tanabe	450.0	570.0	30.0	60.0	60.0	45.4	1.630	323.6	1.630	323.6	4.700	292.7	0	74531	single
97	Tanabe	450.0	570.0	30.0	60.0	60.0	43.1	1.630	323.6	1.630	323.6	4.700	292.7	0	83945	single
98	Tanabe	450.0	570.0	30.0	60.0	60.0	44.4	1.630	323.6	1.630	323.6	4.700	292.7	0	84533	single
99	Tanabe	450.0	570.0	40.0	60.0	60.0	43.8	1.222	323.6	1.222	323.6	4.700	292.7	0	86299	single
100	Tanabe	450.0	570.0	40.0	60.0	60.0	43.1	1.222	323.6	1.222	323.6	4.700	292.7	0	78453	single
101	Tanabe	450.0	570.0	40.0	60.0	60.0	40.8	1.222	323.6	1.222	323.6	4.700	292.7	0	91888	single
102	Tuboi	813.0	507.0	67.0	120.0	107.0	30.2	1.966	296.2	1.891	296.2	3.960	260.9	0	101008	single
103	Tuboi	813.0	507.0	67.0	120.0	107.0	31.4	1.966	296.2	1.891	296.2	8.260	302.0	0	161810	single
104	Tuboi	813.0	507.0	67.0	120.0	107.0	29.9	2.528	296.2	2.583	296.2	3.960	260.9	0	108854	single
105	Tuboi	813.0	507.0	67.0	120.0	107.0	32.2	2.528	296.2	2.583	296.2	8.270	302.0	0	174558	single
106	Tuboi	813.0	507.0	67.0	120.0	107.0	29.7	1.966	296.2	1.894	296.2	3.960	260.9	0	195152	double
107	Tuboi	813.0	507.0	67.0	120.0	107.0	28.6	1.966	296.2	1.894	296.2	8.260	302.0	0	184365	double
108	Matui	840.0	1000.0	40.0	80.0	80.0	15.8	0.331	236.8	0.331	236.8	0.830	286.1	0	45111	single
109	Matui	840.0	1000.0	40.0	80.0	80.0	15.8	0.457	334.9	0.457	334.9	0.830	286.1	0	50504	single
110	Matui	840.0	1000.0	30.0	80.0	80.0	12.3	0.442	433.0	0.442	433.0	3.750	294.2	0	74776	single
111	Matui	840.0	1000.0	30.0	80.0	80.0	12.3	0.610	531.0	0.610	531.0	3.750	294.2	0	70608	single
112	Sugano	1440.0	3960.0	120.0	360.0	360.0	20.6	0.663	571.7	0.663	571.7	1.770	397.2	1174694	2353596	single

113	Sugano	1440.0	3960.0	120.0	360.0	360.0	20.8	0.663	571.7	0.663	571.7	1.770	397.2	2253588	2941995	single
114	Sugano	1440.0	3960.0	120.0	360.0	360.0	21.3	0.663	571.7	0.663	571.7	1.770	397.2	1568873	3138128	single
115	Sugano	1440.0	3960.0	120.0	360.0	360.0	19.6	0.331	571.7	0.331	571.7	1.770	397.2	903450	1814230	single
116	Sugano	1440.0	3960.0	120.0	360.0	360.0	20.8	0.333	571.7	0.333	571.7	1.770	397.2	958764	1912297	single
117	Sugano	1440.0	3960.0	120.0	360.0	360.0	20.5	0.687	284.4	0.663	284.4	1.770	397.2	1071576	2137850	single
118	Sugano	1440.0	3960.0	120.0	360.0	360.0	19.6	0.687	284.4	0.663	284.4	1.770	397.2	987276	1980943	single
119	Sugano	1440.0	3960.0	120.0	360.0	360.0	20.9	0.770	397.2	0.742	397.2	1.770	397.2	1152075	2304563	single
120	Aoyagi	1200.0	2720.0	80.0	320.0	320.0	19.7	0.712	353.0	0.764	353.0	1.740	362.8	0	931632	single
121	Aoyagi	1200.0	2720.0	80.0	320.0	320.0	25.9	0.712	353.0	0.764	353.0	1.740	362.8	0	1029698	single
122	Aoyagi	1200.0	2720.0	160.0	320.0	320.0	29.4	0.580	339.4	0.623	339.4	1.740	362.8	0	1552393	single
123	Aoyagi	1200.0	2720.0	80.0	320.0	320.0	23.8	0.712	353.0	0.764	353.0	6.480	272.2	0	1495514	single
124	Aoyagi	1200.0	2720.0	160.0	320.0	320.0	29.2	0.580	339.4	0.623	339.4	6.480	272.2	0	2309466	single
125	Ohono-Arakawa	700.0	900.0	100.0	100.0	100.0	30.0	0.097	224.1	0.097	224.1	5.030	297.1	0	249089	double
126	Ohono-Arakawa	700.0	900.0	100.0	100.0	100.0	28.6	0.097	224.1	0.097	224.1	5.030	297.1	0	200056	double
127	Yoshizaki	800.0	800.0	60.0	80.0	60.0	23.5	0.219	433.5	0.233	433.5	5.290	332.9	0	101989	single
128	Yoshizaki	800.0	800.0	60.0	80.0	60.0	23.5	0.729	433.5	0.817	433.5	5.880	342.9	0	147100	single
129	Yoshizaki	800.0	800.0	60.0	80.0	60.0	23.5	0.438	433.5	0.408	433.5	8.290	342.7	0	135332	single
130	Yoshizaki	800.0	800.0	60.0	80.0	60.0	23.5	0.729	433.5	0.817	433.5	8.880	345.4	0	158868	single
131	Yoshizaki	800.0	800.0	60.0	80.0	60.0	23.5	1.167	433.5	1.167	433.5	8.880	345.4	0	174558	single
132	Yoshizaki	800.0	1200.0	60.0	120.0	60.0	24.5	0.243	433.5	0.233	433.5	3.530	332.9	0	159848	single
133	Yoshizaki	800.0	1200.0	60.0	120.0	60.0	24.5	0.778	433.5	0.817	433.5	3.920	342.9	0	235360	single
134	Yoshizaki	800.0	1200.0	60.0	120.0	60.0	24.5	0.438	433.5	0.408	433.5	5.530	342.7	0	219669	single
135	Yoshizaki	800.0	1200.0	60.0	120.0	60.0	24.5	0.778	433.5	0.817	433.5	5.920	345.4	0	259876	single
136	Yoshizaki	800.0	1200.0	60.0	120.0	60.0	24.5	1.167	433.5	1.167	433.5	5.920	345.4	0	274586	single
137	Yoshizaki	800.0	1600.0	60.0	160.0	60.0	25.5	0.219	433.5	0.233	433.5	2.650	332.9	0	199075	single

138	Yoshizaki	800.0	1600.0	60.0	160.0	60.0	25.5	0.802	433.5	0.817	433.5	2.940	342.9	0	321560	single
139	Yoshizaki	800.0	1600.0	60.0	160.0	60.0	25.5	0.365	433.5	0.408	433.5	4.440	345.4	0	318716	single
140	Yoshizaki	800.0	1600.0	60.0	160.0	60.0	25.5	0.802	433.5	0.817	433.5	4.440	345.4	0	382459	single
141	Yoshizaki	800.0	1600.0	60.0	160.0	60.0	25.5	1.167	433.5	1.167	433.5	4.730	350.9	0	421686	single
142	Hidalgo	2000.0	1000.0	120.0	100.0	120.0	19.4	0.251	392.0	0.131	392.0	8.500	382.5	0	198094	double
143	Hidalgo	2000.0	1000.0	120.0	100.0	120.0	19.6	0.251	402.0	0.246	402.0	8.500	382.5	0	269683	double
144	Hidalgo	2000.0	1000.0	120.0	100.0	120.0	19.5	0.251	402.0	0.381	402.0	10.583	382.5	0	323619	double
145	Hidalgo	1800.0	1300.0	120.0	130.0	120.0	17.7	0.259	314.0	0.131	314.0	6.538	480.5	0	308909	double
146	Hidalgo	1800.0	1300.0	120.0	130.0	120.0	17.8	0.125	471.0	0.246	471.0	6.538	480.5	0	363827	double
147	Hidalgo	1800.0	1300.0	120.0	130.0	120.0	15.7	0.259	471.0	0.246	471.0	6.538	480.5	0	374614	double
148	Hidalgo	1800.0	1300.0	100.0	130.0	100.0	17.6	0.255	366.0	0.255	366.0	7.000	485.0	0	257915	double
149	Hidalgo	1800.0	1300.0	80.0	130.0	80.0	16.4	0.250	367.0	0.250	367.0	7.308	485.0	0	186326	double
150	Hidalgo	1400.0	1400.0	100.0	140.0	100.0	16.3	0.255	362.0	0.127	362.0	5.714	482.5	0	234379	double
151	Hidalgo	1400.0	1400.0	100.0	140.0	100.0	17.0	0.127	366.0	0.255	366.0	5.714	482.5	0	304006	double
152	Hidalgo	1400.0	1400.0	100.0	140.0	100.0	18.1	0.255	370.0	0.255	370.0	5.714	482.5	0	288316	double
153	Hidalgo	1200.0	1700.0	80.0	170.0	80.0	17.1	0.250	366.0	0.125	366.0	4.412	482.5	0	255954	double
154	Hidalgo	1200.0	1700.0	80.0	170.0	80.0	19.0	0.125	366.0	0.250	366.0	4.412	482.5	0	367749	double
155	Hidalgo	1200.0	1700.0	80.0	170.0	80.0	18.8	0.250	366.0	0.250	366.0	4.412	482.5	0	361865	double
156	Hidalgo	1800.0	1300.0	100.0	130.0	100.0	24.2	0.000	0.0	0.000	0.0	4.615	482.5	0	257915	double
157	Hidalgo	1800.0	1300.0	100.0	130.0	100.0	17.2	0.000	0.0	0.000	0.0	4.615	482.5	0	221630	double
158	Hidalgo	1800.0	1300.0	100.0	130.0	100.0	24.2	0.000	0.0	0.250	431.0	8.538	482.5	0	333426	double
159	Hidalgo	1800.0	1300.0	100.0	130.0	100.0	23.9	0.250	431.0	0.000	0.0	4.615	482.5	0	232418	double
160	Hidalgo	1400.0	1400.0	100.0	140.0	100.0	23.9	0.000	0.0	0.000	0.0	4.286	482.5	0	352059	double
161	Hidalgo	1400.0	1400.0	100.0	140.0	100.0	17.7	0.000	0.0	0.000	0.0	4.286	482.5	0	261838	double
162	Hidalgo	1400.0	1400.0	100.0	140.0	100.0	23.9	0.000	0.0	0.250	431.0	6.500	482.5	0	491313	double

163	Hidalgo	1400.0	1400.0	100.0	140.0	100.0	23.3	0.250	431.0	0.000	0.0	4.286	482.5	0	257915	double
164	Hidalgo	1050.0	1500.0	80.0	150.0	80.0	23.2	0.000	0.0	0.000	0.0	5.000	482.5	0	399131	double
165	Hidalgo	1050.0	1500.0	80.0	150.0	80.0	17.9	0.000	0.0	0.000	0.0	5.000	482.5	0	355981	double
166	Hidalgo	1050.0	1500.0	80.0	150.0	80.0	23.1	0.000	0.0	0.250	431.0	6.667	482.5	0	391285	double
167	Hidalgo	1050.0	1500.0	80.0	150.0	80.0	23.3	0.250	431.0	0.000	0.0	5.000	482.5	0	344213	double
168	Yamada	475.0	1325.0	40.0	125.0	125.0	35.6	0.233	286.0	0.312	286.0	2.020	330.0	0	373000	single
169	Yamada	475.0	1325.0	40.0	125.0	125.0	30.4	0.467	286.0	0.467	286.0	2.020	330.0	0	370000	single
170	Yamada	475.0	1325.0	40.0	125.0	125.0	31.5	0.934	286.0	1.091	286.0	2.020	330.0	0	438000	single
171	Yamada	475.0	1325.0	30.0	125.0	125.0	32.8	0.622	286.0	0.623	286.0	2.020	330.0	0	276000	single
172	Yamada	475.0	1325.0	20.0	125.0	125.0	30.1	0.467	286.0	0.623	286.0	2.020	330.0	0	211000	single
173	Yamada	475.0	1325.0	20.0	125.0	125.0	33.7	0.934	286.0	0.935	286.0	2.020	330.0	0	213000	single
174	Wiradinata	1000.0	2000.0	100.0	200.0	100.0	24.8	0.800	434.4	0.250	424.7	0.800	434.4	14892	573792	single
175	Wiradinata	500.0	2000.0	100.0	200.0	100.0	22.1	0.800	434.4	0.250	424.7	0.800	434.4	8824	680544	single
176	Saatcioglu	1500.0	2000.0	100.0	200.0	100.0	45.0	0.800	449.9	0.800	449.9	0.800	449.9	0	380685	single
177	Saatcioglu	1500.0	1500.0	100.0	150.0	100.0	45.0	0.800	449.9	0.800	449.9	0.800	449.9	0	225405	single
178	Saatcioglu	500.0	2000.0	100.0	200.0	100.0	35.0	0.800	479.9	0.390	248.2	0.800	479.9	0	908634	single
179	Saatcioglu	1000.0	2000.0	100.0	200.0	100.0	35.0	0.800	479.9	0.800	479.9	0.800	479.9	0	529953	single
180	Saatcioglu	1000.0	2000.0	100.0	200.0	100.0	33.0	0.800	479.9	0.800	479.9	0.800	479.9	0	419755	single
181	Saatcioglu	1000.0	2000.0	100.0	200.0	100.0	27.0	0.800	479.9	1.200	479.9	0.800	479.9	0	587056	single
182	Antebi	1016.0	1803.0	50.8	127.0	190.5	21.8	0.250	271.0	0.250	271.0	2.090	324.1	1996	360288	single
183	Antebi	1016.0	1803.0	50.8	127.0	190.5	23.2	0.250	271.0	0.250	271.0	4.720	305.4	2122	453696	single
184	Antebi	1016.0	1803.0	50.8	127.0	190.5	18.4	0.500	393.0	0.500	393.0	2.090	296.5	5059	413664	single
185	Antebi	1016.0	1803.0	50.8	127.0	190.5	41.2	0.500	331.0	0.500	331.0	2.090	275.8	3770	409216	single
186	Antebi	1016.0	1803.0	50.8	127.0	190.5	26.8	0.500	344.8	0.500	344.8	2.090	344.8	2450	444800	single
187	Antebi	1016.0	1803.0	50.8	127.0	190.5	25.6	0.500	344.8	0.500	344.8	2.090	344.8	2343	404768	single

188	Antebi	1016.0	1803.0	50.8	127.0	190.5	28.3	0.500	344.8	0.500	344.8	2.090	344.8	2589	360288	single
189	Antebi	1016.0	1803.0	50.8	127.0	190.5	22.8	0.500	323.4	0.500	323.4	4.720	337.9	2090	471488	single
190	Antebi	1016.0	1803.0	76.2	127.0	190.5	20.3	0.250	313.0	0.250	313.0	2.090	295.8	2794	409216	single
191	Antebi	1016.0	1803.0	76.2	127.0	190.5	14.0	0.250	319.2	0.250	319.2	2.090	313.7	3847	400320	single
192	Antebi	1016.0	1803.0	76.2	127.0	190.5	16.4	0.500	306.1	0.500	306.1	2.090	319.2	4509	409216	single
193	Antebi	1016.0	1803.0	76.2	127.0	190.5	17.0	0.500	343.4	0.500	343.4	2.090	318.5	4679	502624	single
194	Antebi	1016.0	1803.0	76.2	127.0	190.5	14.4	0.500	346.1	0.500	346.1	2.090	312.3	3960	427453	single
195	Antebi	1016.0	3327.0	50.8	127.0	190.5	22.8	0.500	360.6	0.500	360.6	2.090	320.6	3857	493728	single
196	Antebi	1016.0	3327.0	50.8	127.0	190.5	20.0	0.500	348.2	0.500	348.2	2.090	335.8	6760	489280	single
197	Antebi	1016.0	3327.0	50.8	127.0	190.5	19.6	0.500	350.3	0.500	350.3	2.090	318.5	6618	600480	single
198	Barda	952.5	1906.0	101.6	101.6	609.6	29.0	0.500	543.3	0.500	495.8	1.830	525.4	28040	1218307	single
199	Barda	952.5	1906.0	101.6	101.6	609.6	16.3	0.500	551.6	0.500	499.2	6.460	486.8	18985	978471	single
200	Barda	952.5	1906.0	101.6	101.6	609.6	27.0	0.500	544.7	0.500	513.0	4.170	413.7	26172	1108219	single
201	Barda	952.5	1906.0	101.6	101.6	609.6	21.2	0.250	496.4	0.500	496.4	4.170	528.8	20566	876345	single
202	Barda	476.3	1906.0	101.6	101.6	609.6	25.7	0.500	530.9	0.500	501.3	4.170	539.2	14942	1139667	single
203	Barda	1905.0	1906.0	101.6	101.6	609.6	23.4	0.500	527.5	0.500	495.8	4.170	488.9	27235	885552	single
204	Benjamin	508.0	610.4	50.8	101.6	127.0	20.0	0.500	341.3	0.500	341.3	2.210	312.3	0	88960	single
205	Benjamin	508.0	915.2	50.8	101.6	127.0	21.4	0.500	341.3	0.500	341.3	2.210	312.3	0	154790	single
206	Benjamin	508.0	1220.0	50.8	101.6	127.0	19.5	0.500	341.3	0.500	341.3	2.210	312.3	0	201494	single
207	Benjamin	508.0	1778.8	50.8	101.6	127.0	26.2	0.500	341.3	0.500	341.3	2.210	312.3	0	293568	single
208	Benjamin	850.9	1727.2	50.8	127.0	95.3	21.4	0.500	341.3	0.500	341.3	4.190	312.3	0	186816	single
209	Benjamin	850.9	1727.2	50.8	127.0	190.5	20.0	0.250	341.3	0.250	341.3	2.090	312.3	0	249088	single
210	Benjamin	850.9	1727.2	50.8	127.0	190.5	22.1	0.500	341.3	0.500	341.3	2.090	312.3	0	462592	single
211	Benjamin	850.9	1727.2	50.8	127.0	190.5	24.1	0.500	341.3	0.500	341.3	2.090	312.3	0	373632	single
212	Benjamin	850.9	1727.2	50.8	127.0	304.8	22.8	0.500	341.3	0.500	341.3	1.310	312.3	0	293568	single

213	Benjamin	508.0	915.2	44.5	101.6	127.0	24.8	0.500	341.3	0.500	341.3	3.310	312.3	0	204608	single
214	Benjamin	508.0	915.2	44.5	101.6	127.0	19.3	0.250	341.3	0.250	341.3	3.310	312.3	0	137888	single
215	Benjamin	425.5	864.6	25.4	63.5	95.3	21.4	0.500	341.3	0.500	341.3	2.010	312.3	0	90294	single
216	Benjamin	425.5	864.6	25.4	63.5	95.3	20.7	0.500	341.3	0.500	341.3	2.010	312.3	0	88960	single
217	Benjamin	1276.4	2591.8	76.2	190.5	285.8	20.7	0.500	341.3	0.500	341.3	2.000	312.3	0	684992	single
218	Benjamin	698.5	1651.0	50.8	127.0	127.0	26.9	0.500	341.3	0.500	341.3	1.760	312.3	0	301130	single
219	Benjamin	952.5	1143.0	50.8	127.0	127.0	24.8	0.500	341.3	0.500	341.3	4.960	312.3	0	222400	single
220	Benjamin	539.8	1955.8	50.8	127.0	127.0	20.7	0.500	341.3	0.500	341.3	1.760	312.3	0	373632	single
221	Benjamin	850.9	1727.2	50.8	127.0	190.5	21.4	0.500	341.3	0.500	341.3	2.090	312.3	0	302464	single
222	Benjamin	850.9	1727.2	50.8	127.0	190.5	20.7	0.250	341.3	0.250	341.3	2.090	312.3	0	315808	single
223	Benjamin	501.7	1778.8	44.5	101.6	127.0	21.4	1.000	341.3	1.000	341.3	2.210	312.3	0	311360	single
224	Benjamin	501.7	1778.8	44.5	101.6	127.0	22.8	1.000	341.3	1.000	341.3	2.210	312.3	0	366960	single
225	Benjamin	501.7	1778.8	44.5	101.6	127.0	20.7	1.500	341.3	1.500	341.3	2.210	312.3	0	329152	single
226	Benjamin	863.6	1575.5	50.8	120.7	190.5	22.1	0.250	358.5	0.250	358.5	2.250	324.1	0	214386	single
227	Benjamin	863.6	1575.5	50.8	120.7	190.5	21.4	0.250	358.5	0.250	358.5	2.250	324.1	0	178321	single
228	Benjamin	419.1	1644.7	44.5	127.0	127.0	19.9	0.250	358.5	0.250	358.5	3.200	324.1	0	245441	single
229	Benjamin	419.1	1644.7	44.5	127.0	127.0	14.4	0.250	358.5	0.250	358.5	3.200	324.1	0	245441	single
230	Benjamin	584.2	1220.0	50.8	101.6	101.6	16.1	0.500	293.0	0.500	293.0	2.750	293.0	0	178321	single
231	Benjamin	584.2	1220.0	50.8	101.6	101.6	16.1	0.500	293.0	0.500	293.0	2.750	293.0	0	178321	single
232	Benjamin	584.2	1220.0	50.8	101.6	101.6	16.1	0.500	293.0	0.500	293.0	2.750	293.0	0	160288	single
233	Cardenas	1905.0	1905.0	76.2	190.5	76.2	43.0	0.860	448.2	0.270	413.7	8.270	448.2	12490	519082	single
234	Cardenas	1905.0	1905.0	76.2	190.5	76.2	42.5	2.890	448.2	0.270	465.4	2.890	448.2	12330	569789	single
235	Cardenas	1905.0	1905.0	76.2	190.5	76.2	43.0	2.890	448.2	1.000	413.7	2.890	448.2	12490	679210	single
236	Cardenas	1905.0	1905.0	76.2	190.5	76.2	40.3	1.630	448.2	0.000	448.2	1.630	448.2	0	306551	single
237	Cardenas	1905.0	1905.0	76.2	190.5	76.2	43.4	2.890	448.2	1.000	455.1	2.890	448.2	12612	632061	single

238	Galletly	508.0	915.2	44.5	101.6	101.6	35.9	0.790	344.8	0.790	344.8	4.910	317.2	0	273552	single
239	Galletly	508.0	915.2	44.5	101.6	101.6	29.7	1.570	344.8	1.570	344.8	4.910	312.3	0	318032	single
240	Galletly	508.0	915.2	44.5	101.6	101.6	33.8	0.790	344.8	0.790	344.8	2.760	342.7	0	226848	single
241	Galletly	508.0	915.2	44.5	101.6	101.6	34.5	1.570	344.8	1.570	344.8	2.760	342.7	0	284672	single
242	Galletly	508.0	915.2	44.5	101.6	101.6	31.7	0.790	344.8	0.790	344.8	5.510	368.9	0	191264	single
243	Galletly	508.0	915.2	44.5	101.6	101.6	29.7	1.570	344.8	1.570	344.8	5.510	366.8	0	244640	single
244	Massone	1524.0	1524.0	152.4	168.3	152.4	25.5	0.428	424.0	0.278	424.0	3.119	448.2	53324	633840	double
245	Massone	1524.0	1524.0	152.4	127.0	152.4	31.4	0.400	424.0	0.278	424.0	1.700	448.2	51001	453918	double
246	Massone	1524.0	1524.0	152.4	127.0	152.4	31.0	0.400	424.0	0.278	424.0	1.700	448.2	50335	491504	double
247	Massone	1524.0	1524.0	152.4	168.3	152.4	43.7	0.428	424.0	0.278	424.0	3.119	448.2	50760	749933	double
248	Massone	1219.2	1371.6	152.4	127.0	152.4	28.3	0.227	424.0	0.278	424.0	1.333	424.0	644117	753936	double
249	Massone	1219.2	1371.6	152.4	127.0	152.4	31.4	0.227	424.0	0.278	424.0	1.333	424.0	708192	820656	double
250	Massone	1219.2	1371.6	152.4	127.0	152.4	31.9	0.227	424.0	0.278	424.0	1.333	424.0	386993	649408	double
251	Massone	1219.2	1371.6	152.4	127.0	152.4	32.0	0.227	424.0	0.278	424.0	1.333	424.0	387842	682768	double
252	Massone	1219.2	1371.6	152.4	127.0	152.4	29.9	0.227	424.0	0.278	424.0	1.333	424.0	56288	405213	double